Temporally overlapping mechanisms diversify clonal B cell responses *in vivo*.

Oliver P. Skinner[1]*, Saba Asad[1]*, Marcela L. Moreira[1], Hyun Jae Lee[1], Cameron G. Williams[1], Zheng Ruan[1], Jorene Lim[1], Ashlyn S. Kerr[1], Shihan Li[1], Chen Zhu[1], Wang Jin[2], Thiago M. Steiner[1], Takahiro Asatsuma[1], Brooke J Wanrooy[1], Zihan Liu[1], Marcus Z.W. Tong[1], Megan S.F. Soon[3], Jessica A. Engel[4], Kalyan Shobhana[5], Adam P. Uldrich[1], David S. Khoury[2], Zewen Kelvin Tuong[3], Hamish W. King[6,7], Ashraful Haque[1¶]

*These authors contributed equally

Affiliations

[1]Peter Doherty Institute for Infection and Immunity, Department of Microbiology and Immunology, University of Melbourne, Parkville, Victoria, Australia
[2]Kirby Institute, University of New South Wales, Kensington, New South Wales, Australia
[3]Ian Frazer Centre for Children's Immunotherapy, Child Health Research Centre, Faculty of Medicine, University of Queensland, Australia
[4]QIMR Berghofer Medical Research Institute, Herston, Brisbane, Queensland, Australia
[5]Biological Optical Microscopy Platform, University of Melbourne, Parkville, Victoria, Australia
[6]The Department of Medical Biology, The University of Melbourne, Parkville, Victoria, Australia
[7]Epigenetics and Developmental Division, Walter and Eliza Hall Institute of Medical Research, Parkville, Victoria, Australia

*Authors contributed equally
¶Corresponding author: Associate Professor Ashraful Haque, 792 Elizabeth Street, Melbourne, VIC 3000, Australia, e-mail: ashraful.haque@unimelb.edu.au, tel: +613903355206

Abstract

Naive B cells amplify and diversify their responses when activated by cognate antigen, via *Myc*-dependent clonal expansion, immunoglobulin class switch recombination (CSR), phenotypic variation, and somatic hypermutation (SHM). Whether these mechanisms act combinatorially *in vivo* to diversify clonal responses to a single pathogen remains unclear. Since diversity in the antigenic targets, functional classes, and production kinetics of parasite-specific antibodies influences immunity to malaria, we test here whether individual B cell clones diversify over time during *Plasmodium* infection and treatment. During the first week of infection, amid widespread Type I Interferon (IFN)-mediated bystander activation, CSR initiates soon after *Myc* up-regulation, and overlaps partially with clonal expansion, resulting in isotype variegation amongst clones. During the second week of infection, expanded clones that seed germinal centres (GC) bifurcate into extra-follicular plasmablasts, exhibit isotype variegation, and initiate SHM, revealing substantial intra-clonal diversification. Over the following month, GC clones exhibit SHM at approximately four mutations per week, with IgG mutational diversity and IgM^+ cells also preserved in GCs over time. Anti-malarial intervention does not impede SHM, but instead exerts quantitative limits on GC size, plasma cell emergence, circulating IgG levels, and protection against re-infection. Finally, contemporaneous B cell development relocates from bone marrow to spleen during infection and treatment. Thus, multiple temporally overlapping mechanisms combine *in vivo* to amplify, diversify, and safeguard humoral immune responses. We present this data as a temporal, multi-parameter atlas of B cell differentiation *in vivo*: https://bcell-dynamics.science.unimelb.edu.au

58 **Graphical abstract**

59

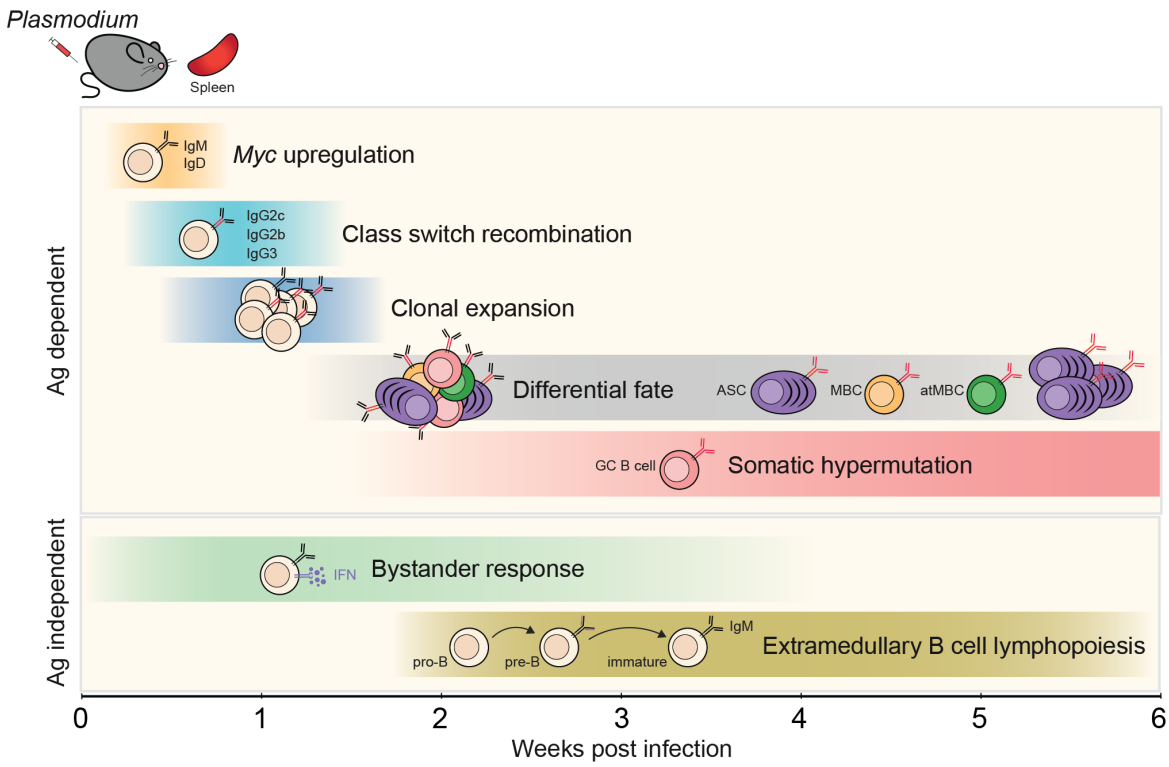

60

61

62 **Highlights:**

63

64 1. Partial temporal overlap of CSR with clonal expansion leads to isotype variegation in clones.

65 2. Clones seeding GCs bifurcate into plasmablasts and exhibit isotype variegation.

66 3. GC B cells accrue ~4 mutations/week, a rate unaffected by anti-malarials.

67 4. *Plasmodium* infection triggers antigen-independent Type I IFN-mediated bystander activation.

68 5. B cell development is preserved in malaria by shifting from bone marrow to spleen.

69

70

71

72

73

74

75

76

Introduction

Antigen receptor engagement on naive B cells initiates not only clonal expansion, but also a range of phenotypic changes and genetic alterations that increases diversity beyond that offered by pre-existing BCRs alone. Phenotypes adopted include short-lived antibody-secreting plasmablasts, memory B cells, atypical B cells, germinal centre B cells and plasma cells, each with distinct functions within the overall humoral immune response. Further diversification proceeds via class switch recombination (CSR), which replaces the constant portion of BCRs with one of a number of functionally varied isotypes (*e.g.* IgG1, IgG2, IgG3, IgG4, IgA1, IgA2 and IgE in humans)[1,2]. In addition, B cells entering germinal centres (GC) can further diversify their BCRs via somatic hypermutation (SHM)[3-6], leading to affinity maturation of resulting antibodies[7].

B cell diversification during infection can either promote or impair humoral immunity, as evidenced during blood-stage *Plasmodium* infection, in which plasmablast responses can limit immunity to malaria[8], while increased breadth of antibody specifities[9,10] and effector functions[11] is associated with greater protection against symptoms. Understanding when diversification mechanisms operate and whether they interact *in vivo* may offer opportunities for tuning immunological responses. In addition, although anti-malarial drugs have been instrumental in reducing the morbidity and mortality associated with malaria[12], their impact on long-term immunity remains unclear[13-18].

Experimental vaccination with single antigens has revealed several *in vivo* aspects of CSR and phenotypic diversification in single naive B cells. Firstly, CSR can occur prior to GC entry [19-21]. Secondly, in some cases[22], but not others[23], CSR occurs independently of phenotypic changes. Thirdly, the degree of phenotypic diversification by expanded clones is controlled by the BCR itself, and is further regulated by apoptosis during clonal expansion[22]. CSR is largely thought to act orthogonally to processes determining phenotypic fate, relying on stochastic expression of activation-induced cytidine deaminase (AID) and germ-line transcripts (GLT)[24]. Viral infection studies have revealed SHM dynamics within the GC[25], showing that mutations accrue and then diminish due to ongoing invasion by naive B cells[25,26]. Recent studies of steady-state human tonsils identified transient, intermediate states of B cell activation[27,28]. Although these observations provide vignettes of B cell clonal diversification, temporal relationships of, and interactions between these mechanisms remain to be determined within a single *in vivo* model.

Here, we employ scRNAseq, BCRseq, and spatial transcriptomics to map over time the diversification mechanisms that operate in polyclonal B cells *in vivo,* using a model of blood-stage infection with *Plasmodium* parasites*,* an antigenically complex protozoan[29,30], which continues to threaten global human health[31].

Results

Plasmablast and GC B cell differentiation temporally overlaps with Type I IFN-mediated bystander activation during experimental malaria.

To assess polyclonal B cell diversification over time, we employed blood-stage *Plasmodium chabaudi chabaudi* (*Pc*AS) infection of C57BL/6J mice. This model is characterised by peak parasitemia ~7-9 days post-infection (dpi), followed by $CD4^+$ T-cell dependent, antibody-mediated, parasite elimination over the following 60-90 days[32,33]. We performed paired scRNAseq and BCRseq of splenic polyclonal B cells ($CD19^+$ $B220^{int-hi}$) prior to and 4-, 7-, 10- and 14 dpi, reasoning this would capture early activation events and progressive emergence of plasmablasts and GC B cells (Fig. 1A). From 20 mice, 40,623 transcriptomes passed quality-control: day 0 (2,322 cells, n=1); day 4 (9,079 cells, n=4), day 7 (4,337 cells, n=5), day 10 (11,407 cells, n=5) and day 14 (13,478 cells, n=5). Dimensionality reduction, unbiased clustering, and canonical marker analysis revealed multiple subsets emerging over time (Extended Data Fig. 1A-C), in particular plasmablasts and GC B cells evident at days 10 and 14 dpi, displaying kinetics consistent with previous flow cytometric studies[32,33] (Fig. 1B). This suggested the data could be employed for examining B cell diversification mechanisms.

In addition to expected plasmablast and GC B cell differentiation we noted increased frequency at 4 and 7 dpi of a cluster of unswitched, non-proliferating B cells (Fig. 1C-D), defined by up-regulation of interferon-associated genes, including *Stat1*, *Socs1, Irf1* and *Irgm1* (Fig. 1E). *Ly6a* (encoding SCA-1) and *Ly6c2* (encoding Ly6C), were also upregulated (Extended Data Fig. 2A). This suggested B cells lacking specificity for *Plasmodium* antigens had responded in a bystander, interferon-mediated fashion during infection. Kinetics of SCA-1 and Ly6C expression were confirmed at protein level on IgD^+ cells by 4 dpi, which was sustained until day 14 (Fig. 1F). SCA-1/Ly6C up-regulation was less pronounced in CD4-depleted mice (Extended Data Fig. 2B)[32], suggesting partial T-cell-dependence for this phenomenon. We confirmed bystander activation in ovalbumin-specific OB1 cells after transfer and infection with non-ovalbumin expressing *Pc*AS (Fig. 1G; Extended Data Fig. 2C). Finally, SCA-1/Ly6C upregulation by IgD^+ cells was abrogated by IFNAR1-blockade (Fig. 1H), while B cell-intrinsic genetic deficiency of Toll-like receptor adaptor, *Myd88,* had no effect (Extended Data Fig. 2D). Thus, plasmablast and GC B cell differentiation had occurred amid Type I IFN-mediated bystander B cell activation in the spleen during experimental malaria.

CSR occurring soon after *Myc*-upregulation overlaps with clonal expansion.

Given plasmablasts and GC B cells had been detected within the scRNAseq data by 10-14 dpi (Fig. 1B), we next searched for evidence of early activation, clonal expansion and progressive phenotypic change. We observed a transient increase at 4 dpi of cells marked by upregulation of *Myc, Nfkbid*, *Cd83, Cd69* and *Jun*, consistent with early activation[27,28,34-36] (Fig. 2A). Although we observed no cell-states consistent with intermediate or progressive differentiation towards plasmablasts, we did note early activated cells positioned adjacent to emerging GC B cells (Fig. 2A). Closer examination revealed that early-activated cells, in

154 addition to strong *Myc*-expression had up-regulated CSR-related genes[27] though not cell-
155 cycling genes (Fig. 2B). Inference of progressive, overlapping, transitions from *Myc*-
156 upregulation to CSR and clonal expansion was supported by Bayesian Gaussian Process
157 Latent Variable Modelling (BGPLVM) and pseudo-temporal ordering (Fig. 2B & C), an
158 approach we previously used for inferring progressive change in $CD4^+$ T cells[37-39]. Given only
159 a subset of cells within the early activated cluster had upregulated *Myc* and CSR-related
160 genes, we re-clustered these to further test for overlap (Extended Data Fig. 3A), and to search
161 for novel genes associated with early activation. After unsupervised clustering, we noted
162 Cluster 5 exhibited the highest *Myc*-upregulation (Extended Data Fig 3B), amongst other
163 genes (Extended Data Fig. 3C, Supplementary Table 1), while Cluster 8 displayed moderate
164 *Myc*-upregulation, the highest expression of CSR-related genes, and emerging upregulation
165 of cell-cycling genes, within activated B cells (Extended Data Fig. 3B), consistent with
166 temporal overlap.

167 Finally, we tested for early overlap of CSR and clonal expansion by flow cytometric
168 assessment of splenocytes at 4 dpi. First, co-expression of CD83 and CD69 was employed
169 to enrich for polyclonal B cells recently activated by cognate antigen (Fig. 2D). Next,
170 compared to $CD83^-$ $CD69^-$ B cells in either infected or naïve control mice, ~1% of recently
171 activated $CD83^+$ $CD69^+$ cells had switched to IgG2c (Fig. 2E). Of note, the majority of these
172 co-expressed IgD, which given the relatively low turnover of surface protein IgD[40], suggested
173 these cells had recently switched. Furthermore, these cells expressed Fas, similar to a report
174 in which Fas^+ B1-8^{hi} cells underwent CSR prior to GC seeding[21] (Fig. 2F). Crucially, $IgG2c^+$
175 $CD83^+$ $CD69^+$ recently-switched B cells exhibited elevated levels of the proliferative marker,
176 Ki67 relative to unswitched comparator populations (Fig. 2G), consistent with overlap of CSR
177 and clonal expansion. Together, our data support a model in which CSR initiates soon after
178 *Myc* upregulation, and importantly, partially overlaps with clonal expansion.

179 **Activated B cell clones seeding GCs bifurcate into plasmablasts and exhibit isotype**
180 **variegation.**

181 Partial temporal overlap of CSR and clonal expansion suggested a proportion of activated B
182 cell clones, having undergone at least one cell division prior to CSR, could exhibit Ig isotype
183 variegation (since our model elicits IgG2b, IgG2c, IgG1, IgG3, and IgM[32,33,41]). Furthermore,
184 given subsequent differentiation into plasmablasts and GC B cells (Fig. 1B), we hypothesized
185 single naïve B cells could elicit diverse progeny exhibiting both multiple fates and multiple Ig-
186 isotypes.

187 To test for such clonal diversification, we first searched for expanded clones in our initial 0-
188 14 dpi scRNAseq/BCRseq dataset. Cells were defined as clonal when sharing identical *V*
189 and *J* genes, identical junctional CDR3 amino acid length, and >85% amino acid CDR3
190 sequence identity as previously described[42,43]. Amongst ten mice across 10 and 14 dpi, we
191 detected 356 expanded clones harbouring 2-8 cells (Fig. 3A), the majority of which (297
192 clones) consisted of two cells (hereafter referred to as “twins”), which were shared relatively
193 uniformly across all mice (Fig. 3B). A repeat scRNAseq/BCRseq experiment (6 mice across
194 10 & 14 dpi) supplemented the dataset, providing a total of 721 expanded clones, of which

592 were twins (Fig. 3B & C). Thus, despite shallow sampling of splenic B cell compartments in individual mice, our datasets nevertheless permitted testing for clonal diversification.

Firstly, we determined across 10 and 14 dpi whether individual clones could differentiate into both GC B cells and plasmablasts (Fig. 3C). The majority (567 out of 721) of expanded clones gave rise to plasmablasts only, consistent with these short-lived antibody secreting cells dominating at early time-points, although we noted ~50% reduced efficacy in BCR-detection amongst GC B cells compared to plasmablasts due to lower BCR gene expression levels. Nevertheless, across all 461 plasmablast twins, 119 (25.8%) of these exhibited isotype variegation, consistent with partial temporal overlap of CSR and clonal expansion (Fig. 3C).

Amongst 592 twins, 92 gave rise to at least one GC B cell, with 53 (57.6%) bifurcating to give rise to a plasmablast (Fig. 3C) – the frequency of fate bifurcation rose to 100% for the small number (19 clones) of GC-containing clones with >2 family members (Fig. 3C). Furthermore, of GC-containing twins 19.6% exhibited both isotype variegation and fate bifurcation (Fig. 3C), consistent with our original hypothesis.

Finally, to examine clonal diversification in larger clone sizes, we sampled more deeply plasmablasts and GC B cells flow cytometrically sorted from a single representative spleen (n=5) at 14 dpi (Fig. 3D, Extended Data Fig. 4A). From 19,482 post-QC B cell transcriptomes from a single mouse, 9,350 plasmablasts, and 8,744 GC B cells were detected in the paired scRNAseq/BCRseq data (with minor populations of memory/atypical cells and spike-in naive cells) (Extended Data Fig. 4A). Amongst these, we detected 478 twins, 38.4% of which exhibited isotype variegation (Fig. 3D), further supporting temporal overlap for CSR and clonal expansion. Of 107 clones comprised of 5 cells or more, and similar to experiments above (Fig. 3C), 100% of GC-containing clones (34 clones) had also given rise to plasmablasts (Fig. 3D) (which harboured as few mutations as naïve B cell controls, consistent being extrafollicular, not GC-derived) (Extended Data Fig. 4B). Furthermore, isotype variegation was evident in most (81.9%) clones comprised of 5 cells or more (Fig. 3D). Taken together, our data suggested it was commonplace during the first two weeks of infection for antigen-activated B cells, particularly GC-seeding clones to have exhibited both phenotypic and Ig-isotype diversification.

GC B cells progressively diversify via a constant SHM rate and retention of isotype diversity.

Having observed phenotypic and isotype diversification amongst GC-seeding clones, we next sought to determine the extent to which SHM further diversified B cells in our model of persisting infection. Furthermore, given evidence of reduced affinity maturation and disrupted splenic GC structures in malaria-endemic regions[44,45], we also sought to determine if anti-malarial drug intervention altered GC B cell biology during *Plasmodium* infection. Thus, we generated an extended scRNAseq/BCRseq time course until 42 dpi, which included a parallel arm of anti-malarial drug intervention from 7 dpi (Fig. 4A, Extended Data Fig. 5A).

To focus assessment on B cells activated via cognate antigen, we FACS-sorted IgD^{lo} B cells ($CD19^{+}$ $B220^{int\text{-}hi}$), spiking back in small numbers of IgD^{hi} naive cells at each timepoint to

assist in batch effect removal. We isolated 72,359 B cells across two treatment arms (*Pc*AS: 38,651 cells, *Pc*AS+drug: 27,452 cells, n=3 mice per timepoint) from 42 mice: IgD^{hi} spike-in from un-infected mice (6,256 cells, n=7); 10 dpi (9,250 cells), 14 dpi (10,338 cells), 21 dpi (15,766 cells), 28 dpi (12,251 cells), 35 dpi (15,502 cells) and 42 dpi (9,252 cells). Within the combined scRNAseq data (after confirmation of minimal batch effects), we inferred 11 distinct cell types including transient ASCs and increasing GC B cell frequencies (Fig. 4B). Most cell-types showed little change in frequency as a result of anti-malarial treatment, except for GC B cells which dropped by 36.2%, and MZ B cells and B1 cells, which increased by 148% and 75%, respectively (Extended Data Fig. 5B). Flow cytometric assessment confirmed a reduction in GC B cell numbers within the spleen by 42 dpi following drug treatment, with similar trends for ASCs, atypical and memory B cells (Extended Data Fig. 5C) as observed in the scRNAseq data (Extended Data Fig. 6A-B).

We next searched for qualitative changes in GC B cells over time and after anti-malarial treatment within the extended scRNAseq time-course. Phenotypic characterisation of GC B cell subsets using canonical gene markers and gene signatures[46], identified putative Light Zone (LZ), Dark Zone proliferating (DZp) and differentiating (DZd) cells, as well as mixed LZ/DZ cells and *Ccr6*$^{+}$ memory B cell precursors (preMems) (Fig. 4C, Extended Data Fig. 7A). Confirmation of annotations was provided by spatial transcriptomics, which localised LZ and DZp/DZd transcriptomes to adjacent microanatomical regions within GCs in the spleen at 30 dpi[39] (Extended Data Fig. 7B). By 21 dpi, the relative frequency of GC B cell subsets had stabilized (Fig. 4D), consistent with an equilibrium having been reached within GCs at a population level.

Of note, anti-malarial intervention had little qualitative effect on GC B cell composition, particularly between 21-42 dpi (Fig. 4D), despite the quantitative reductions in proportions of B cells displaying any GC B cell phenotype, a phenomenon validated by flow cytometric assessment with established markers[46,47] (Extended Data Fig. 7C & D). These data suggested functional stability of GCs over time and after antimalarial treatment, which was supported by stable *Aicda* gene expression in DZ GC B cells (Fig. 4E). To formally test for GC function, we quantified SHM rates by comparing BCR sequences to germline. Firstly, as expected, we detected few mutations in BCRs of either naive follicular B cells or subsets not expected to engage in SHM (Fig. 4F, Extended Data Fig. 8). In contrast, GC B cells exhibited a progressive increase in median number of mutations summed across heavy and light chains, at a constant rate of 3.71 mutations per week, which remained unaltered (3.79 mutations per week) after anti-malarial treatment (Fig. 4F). Of note, SHM was detected as early as 10 dpi, a timepoint dominated by unmutated extrafollicular plasmablasts (Fig. 4B). Thus, mutational analysis supported GC functional stability over time and after antimalarial treatment by revealing constant SHM rates. Furthermore, SHM rates observed here were similar to those in previous studies of Ighv regions in murine lymph node GC B cells after influenza infection[25,48] (Fig. 4G), further suggesting that SHM in our model of experimental malaria was not impaired relative to that of viral infection.

275 Having confirmed GC functional stability, we also noted that by 42 dpi GC B cells harboured
276 BCRs with a wide spectrum of mutations, from 0-40 mutations per cell, with little skewing
277 towards only highly mutated BCRs, as quantified by a progressive increase in the interquartile
278 range of mutation counts over time (Fig 4H). Furthermore, although IgG1, IgG2b, IgG2c, IgG3
279 or IgA isotypes were largely retained over time and after treatment (Fig. 4F), a proportion of
280 GC B cells was evident which expressed IgM and harboured 0-10 mutations (Fig. 4F and
281 Extended Data Fig. 9). Taken together, our analysis revealed that once GCs are seeded, an
282 immediate and progressive diversification of participating B cells ensues, mediated not only
283 by a constant SHM rate, but also by the emergence and retention of unswitched cells with
284 low numbers of mutations.

285 **Anti-malarial treatment exerts quantitative limits on GC output.**

286 Although GC B cell subset composition and SHM rates were unaffected by antimalarial
287 treatment, it nonetheless elicited a quantitative drop in GC B cell frequency (Extended Data
288 Fig. 5B-C). Hence, we next hypothesized that output from GCs was impaired by anti-malarial
289 treatment. Consistent with this, inferred switched memory and atypical memory B cells, with
290 mutations in BCRs consistent with GC origin (Extended Data Fig. 10), exhibited reduced
291 numbers in the spleen following anti-malarial drug treatment, particularly at later stages of
292 the infection (Extended Data Fig. 5C).

293 Secondly, we assessed GC output by searching for emerging plasma cells in the spleen, by
294 re-clustering ASC transcriptomes within scRNAseq data of IgD^{lo} CD19^{+} B220^{int-hi} cells (Fig.
295 5A). This revealed a cluster expressing high levels of *Prg2,* a putative marker of splenic
296 plasma cells[49] (Fig. 5A). Given our sorting strategy had precluded detection of mature B220^{-}
297 CD19^{-} mature plasma cells, we reasoned splenic *Prg2*^{hi} ASCs, which had isotype-switched
298 (Fig. 5B), and harboured high mutation counts from 21 dpi (Fig. 5C), were likely pre-plasma
299 cells. *Prg2*^{hi} pre-plasma cell transcriptomes appeared to drop in frequency after anti-malarial
300 treatment (Fig. 5D), providing further evidence of quantitative reduction in GC output. Finally,
301 to formally screen for GC output we quantified long-lived plasma cells (LLPCs) amongst
302 ASCs in the bone marrow, via flow cytometric assessment of CD138, TACI, CD19 and
303 B220[50,51] (Fig. 5E). At 42 dpi we detected a reduction in LLPCs in bone marrow after
304 antimalarial drug treatment (Fig. 5E), suggesting GC output had been impaired. Consistent
305 with reduced LLPC numbers, anti-malarial drug treatment also reduced circulating parasite-
306 specific IgG (Fig. 5F) and rendered mice more susceptible to high-dose homologous re-
307 challenge (Fig. 5G). Taken together, our data reveal that anti-malarial treatment exerts
308 quantitative limits on GC output during experimental malaria.

309 **B cell lymphopoiesis relocates to the spleen during experimental malaria.**

310 Presence within GCs between 21-42 dpi of unswitched B cells harbouring few mutations
311 suggested these as recent invader clones, consistent with viral infection and immunisation
312 models[25,26]. In considering ongoing sources of naive B cells, we noted from 14 dpi,
313 pronounced emergence of cells lacking *Ighd*, yet expressing *Il7r* and surrogate light chain
314 gene *Vpreb1,* suggestive of precursor B cells (Extended Data Fig. 1C and 6A). To test for

315 developing B cells in the spleen, we integrated our scRNAseq data (Extended Data Fig. 11A-
316 C), with a dataset of developing B cells in the bone marrow[52] (Extended Data Fig. 11D-E).
317 Splenic data merged with bone marrow transcriptomes in certain expected areas, *e.g.* mature
318 B cells (cluster 1) and ASCs (cluster 13) (Extended Data Fig. 11D), providing confidence in
319 the integration. Inferred splenic immature and precursor B cell populations integrated with
320 reported bone marrow counterparts (Extended Data Fig. 11D). Based on the integrated
321 embedding and canonical markers, we annotated splenic precursor B cells as pro-and cycling
322 pro-B cell (*Vpreb1, Igll1, Dntt, Rag1, Il7r, Il2ra, Ebf1, Ighd$^-$, Cd74$^-$, Ms4a1$^-$*), pre-B cells (*Rag1,*
323 *Il7r, Il2ra, Ebf1, Ighd$^-$, Cd74$^-$, Ms4a1$^-$)* and immature B cells (*Ighd$^-$, Ighm$^+$, Ms4a1, Cd74*) on
324 our integrated Experiment 1 and 2 UMAP (Fig. 6A and Extended Data Fig. 11F). Mapping
325 transcriptomes over time suggested pro- and cycling pro- B cells emerged first at 14 dpi
326 before subsiding, followed by pre-B cells peaking at 21 dpi, with immature B cells persisting
327 until 42 dpi (Fig. 6A and Extended Data Fig. 12A). Anti-malarial drug treatment had little effect
328 on these dynamics (Extended Data Fig. 12A). We then confirmed these dynamics via flow
329 cytometric analysis of IL7R, IgM, CD43 and CD24 on IgD^{lo} CD93$^+$ non-plasmablast, non-GC
330 B cells (Fig. 6B and Extended Data Fig. 12B), and secondly that the phenomenon was
331 unaffected by anti-malarial drug treatment (Extended Data Fig. 12C).

332 To investigate whether immature B cells might complete their development in the spleen, we
333 first examined their location within the spleen at 30 dpi. Spatial transcriptomics at 10µm
334 resolution, followed by cell-type deconvolution as previously[39], revealed immature B cell
335 transcriptomes co-localised with naïve B cells within follicles (Fig 6C, Extended Data Fig.
336 13A-B), consistent with potential to complete maturation in the spleen. To formally test this,
337 we adoptively transferred splenic CD93$^+$ IgD$^-$ cells, also expressing eGFP, from infected mice
338 (confirming splenic precursors at 21 dpi, Extended Data Fig. 14A) into infection-matched mice
339 (Fig. 6D), and confirmed maturation 21 days later via loss of CD93 and acquisition of surface
340 IgD (Fig. 6E). Of note, these cells had not given rise to ASCs or GC B cells by this time-point
341 (Fig. 6E and Extended Data Fig. 14B). Together, these data demonstrated that splenic B cell
342 precursors could traffic to follicles and complete maturation into naïve B cells amid an ongoing
343 humoral immune response.

344 Finally, we sought to infer cellular and molecular mechanisms supporting B cell development
345 in the spleen. High-resolution spatial transcriptomics at 21 dpi revealed non-random
346 distributions of pre-B cells adjacent to white pulp zones, and, in particular, their co-localisation
347 with multiple white pulp stromal cells: T cell zone reticular cells (TRCs), T-B reticular cells
348 (TBRCs) and marginal reticular cells (MRCs) (Fig. 6F & G). Of note, these cell-types express
349 high levels of *Il7* at steady state[53] (Fig. 6H), a cytokine important for B cell development in
350 the bone marrow[54-56], with its receptor, *Il7r*, also expressed by splenic pre-B cells in our model
351 (Extended Data Fig. 11F). Together, these data support a role for multiple white pulp stromal
352 cell populations in supporting B cell development in the spleen, a process that temporally
353 overlaps with SHM-mediated diversification of B cells in GCs.

354 **A Graphical User Interface (GUI) enables multi-parameter assessment of B cells *in***
355 ***vivo.***

356
357 Having observed in our scRNAseq/BCRseq time-course a spectrum of overlapping B cell
358 processes, including initial activation, CSR, clonal expansion, ASC differentiation, SHM in
359 GCs, bystander activation, and splenic B cell lymphopoiesis, we next curated the data into
360 a Graphical User Interface (GUI) alongside the high-resolution spatial transcriptomics data.
361 (https://bcell-dynamics.science.unimelb.edu.au). The GUI enables simultaneous
362 interrogation of individual B cells for 1) time-point, 2) cell-type 3) gene expression profile, 4)
363 antibody isotype, 5) BCR sequence/mutation count, 6) clonal relationships with other cells,
364 and 7) location of specific B cells states relative to other immune and non-immune cell types
365 within the spleen. We reasoned such multi-parameter assessment would assist in hypothesis
366 generation relating to B cells within secondary lymphoid organs. We present below three
367 examples highlighting the utility of this GUI.

368

369 ***Case Study 1: Mining for pathogen-specific immunoglobulins.***
370 Monoclonal antibodies, developed against known *Plasmodium* surface antigens, have shown
371 promise clinically for preventing malaria in humans (CIS43LS and L9LS Abs)[57-60]. BCRs
372 harbouring specificity to unknown *Plasmodium* antigens might also be of potential use, *e.g.*
373 for *de novo* immunoglobulin discovery pertaining to the field of malaria-prevention. Hence,
374 we employed our GUI to search for BCRs with potential to bind *Plasmodium* antigens. We
375 screened GC B cell transcriptomes (expressing *Aicda*) at later timepoints (28-42 dpi) for those
376 switched to IgG isotypes, and with high numbers of mutations within their BCRs. Paired IGH
377 and IGL sequences were downloaded, cloned, and recombinantly expressed (Fig. 7A).
378 Subsequent ELISA-based analyses confirmed *Plasmodium*-binding, relative to similarly
379 expressed negative control BCRs (Fig. 7A). Thus, our GUI likely harbours a collection of
380 BCRs exhibiting specificity to as yet uncharacterised blood-stage *Plasmodium* antigens.
381 Experimental and/or computational approaches may in the future determine precise antigen-
382 specificities.

383

384 ***Case Study 2: Inferring a pre-plasma cell state within the spleen.***
385 It was recently reported that differentiation towards a plasma cell fate in the spleen could be
386 discerned via *Prg2* expression and concomitant down-regulation of *Ssr2*[49]*.* To further test
387 this, we examined our GUI for evidence of ASCs expressing high levels of *Prg2,* and reduced
388 expression of *Ssr2* (Fig. 7B). Having located these cells at 21-42 dpi, further evidence of
389 these as pre-plasma cells was provided by having switched to IgG, harbouring high numbers
390 of mutations consistent with having derived from the GC, and with clonal relationships with
391 GC B cells (Fig. 7B). Hence, multi-parameter assessment at certain timepoints, of gene
392 expression profiles, BCR isotype and mutation counts provided further of evidence of the
393 existence of splenic pre-plasma cells.
394

395 ***Case study 3: Assessing cellular co-localisation and in situ gene expression within the***
396 ***spleen.***

397 To enable spatially-informed hypothesis generation regarding cell-type location, co-
398 localisation and gene expression, we present within the GUI a genome-wide spatial
399 transcriptomic (ST) data of two representative spleens at 21 dpi (when GCs are maturing,
400 and B cell development is evident), generated from 1cm^2 *Stereo-seqV1.2* arrays (with each
401 pixel binned from 400 capture spots, approximating to a final working resolution of 10µm x
402 10µm) (Fig. 7C). This enables determination of relative location of several cell types (*e.g.* GC
403 B cells, red blood cells (RBC), naïve CD4$^+$ T cells and naïve B cells (Fig. 7C), as well as
404 stromal cells. Displayed cell-types may then be filtered according to whether a given gene is
405 detected at that location within the ST data. For example, having displayed four different
406 stromal cell populations, TRC, FDC, MRC and RP FB, we observed *Mfge8* was expressed
407 not only on FDCs as reported previously[61], but also on other stromal cells such as TRCs (that
408 also expressed *Ccl19*) and MRCs (Fig. 7C), which further support the notion that *Mfge8*
409 expression is not limited to FDCs[62,63].

410 Taken together, our GUI enables multiple parameter analysis of B cells in the spleen over
411 time and space, via the examination of time points, cell-types, gene expression profiles,
412 antibody isotypes, BCR mutation counts, clonal relationships, and spatial co-localisation.

413

414

415

416

Discussion

Here we tested the hypothesis that population-level diversity amongst polyclonal B cell responses during infection is contributed to by intra-clonal diversification. We employed experimental malaria as a model, rather than single-antigen vaccination, because *Plasmodium* parasites express hundreds of proteins[29,30], and might be expected to activate a broad spectrum of antigen-specific B cell clones. Furthermore, effective naturally acquired immunity to malaria benefits from a breadth of *Plasmodium*-specific antibodies[9,10]. By employing scRNAseq and paired BCRseq over time, we observed it was commonplace amongst hundreds of expanded clones, for the progeny of single naive B cells to vary both in the phenotypes and switched IgG sub-classes adopted. This suggests that during infection with a complex pathogen, although initial BCR sequence and antigen affinity can determine fate, as with single-antigen vaccination[22], that BCR-independent processes may be important for diversifying the progeny of single naive B cells.

CSR can occur prior to GC formation during experimental vaccination[19-21]. Our observations during *Plasmodium* infection are consistent with this model, although the absolute timing of responses appears slower than that elicited by vaccination, perhaps due to low parasite numbers and hence antigen availability at early stages. scRNAseq over time facilitated the inference that *Myc*-upregulation, CSR and clonal expansion occur in a specific order, in which they nevertheless overlap with each other. Differential gene expression analysis presented here and visualised in our GUI highlights potential understudied genes in B cell activation, such as *Irf1*, which although implicated in gammaherpesvirus infection[64], remains poorly studied in B cells. Recent work highlights methods for functional gene testing in naïve B cells[65], which could be employed to test genetic targets mined from our data.

The consequences of temporal overlap between transcriptional programs associated with clonal expansion and CSR is that certain clones might commit to switching prior to clonal expansion, while others would initiate proliferation before committing to switching. Deeper sequencing of B cells from a single mouse raised the possibility that clonal isotype variegation may be the dominant outcome during infection, at least in our model, which further suggests substantial overlap and division-linked CSR *in vivo*, as suggested by previous *in vitro* studies[66-68]. To determine whether intra-clonal phenotypic variation is beneficial one might consider an alternative scenario in which initial BCR sequence fully determines fate and isotype in a given innate immune environment. In such a case, clones displaying specificity for an important, protective, pathogen-derived epitope would be locked into a single response that may not be optimal for pathogen control. In contrast, intra-clonal diversity early during infection may act as a “bet-hedging” strategy, providing responsive clones with functional flexibility, *e.g.* to enter the GC or not, to produce IgG2b, IgG3 or IgG2c, or to elicit rapid extra-follicular responses. Indeed, enhanced breadth of antibody isotypes mounted following malaria is associated with better clinical immunity[11]. Since many initial GC clones had also given rise to plasmablasts, we hypothesise GC entry remains an inclusive process that encourages diversity during recruitment for SHM.

457 Data from this study, together with previous reports[19-21], prompts a consideration of why CSR
458 initiates early, prior to GC entry. One explanation is that innate cytokine-mediated tailoring of
459 humoral immune responses[69-71], specifically of which antibody isotypes to deploy for a given
460 pathogen class, must necessarily occur soon after pathogen sensing has occurred, *e.g* via
461 pathogen-associated molecular patterns (PAMPs). This is likely to be within hours to a few
462 days after pathogen exposure. Hence, it seems likely the CSR transcriptional program must
463 be initiated at a time when innate immune responses have recently occurred, and innate
464 cytokines are circulating within secondary lymphoid organs. Additionally, it may streamline
465 affinity maturation within the GC by having many clones switched to IgG early during infection.
466 Of note, this model does not preclude CSR from continuing within the GC, a prominent zone
467 for AID expression[72,73]. Given the persistence of IgM^+ GC clones in our model as in other
468 studies[21,74], we speculate that CSR continues in the GC across various times during infection.

469 The initial dynamics of SHM within GCs have been explored during hapten exposure or viral
470 infection[25,48,75]. This has revealed linear rates of mutation acquisition in the heavy chains of
471 BCRs of 1.9-2.1 mutations per week[25,48]. In our model, we also note a constant SHM rate
472 over the first 6 weeks of infection of ~2 mutations in the heavy chain per week, with similar
473 rates evident for light chains. Our analysis suggests SHM initiates as early as 10 dpi during
474 *Plasmodium* infection, at a rate comparable to viral infection[25,48]. Although our previous work,
475 and from others revealed GC B cell responses are sub-optimal during *Plasmodium*
476 infection[32,33], we hypothesise this is due to limits on clonal expansion and fate choice, rather
477 than adverse effects on SHM. We next consider why SHM rate is constant. AID expression
478 levels are constant in GC B cells over time in our model. This is consistent with estimates
479 that GC B cells mutate $1x10^{-3}$ per base pair per cell division[76,77]. However, although a recent
480 study also suggested AID expression remained constant[78], high affinity clones shielded
481 themselves from deleterious mutations by spending less time during G0/G1 phase of the cell
482 cycle, such that mutation rates were not constant amongst all GC clones[78,79]. Whether there
483 is inter-clonal variation of SHM rates in our data is unknown. We also noted that anti-malarial
484 treatment, which lowers parasite numbers and protects against splenomegaly, had no effect
485 on SHM rates, despite deleterious effects on GC size, antibody titres, LLPC numbers and
486 susceptibility during re-infection. Whether sufficient antigen remains on follicular dendritic
487 cells (FDCs) to facilitate selection after anti-malarial treatment remains to be tested. Our data
488 may be relevant for humans treated for mild malaria[31], who could potentially harbour GCs in
489 which affinity maturation continues unimpaired. However, complementary strategies with
490 monoclonal antibodies or vaccines may be needed to quantitatively boost humoral immunity.
491 In support of this, a recent phase III clinical trial suggests that combination of seasonal anti-
492 malarial chemoprophylaxis and vaccination with $RTS,S/AS01_E$ provide better clinical
493 protection to malaria compared to either strategy in isolation[80].

494 Our untargeted approach of examining polyclonal B cells facilitated the discovery of two
495 phenomena that would have been missed with a focus on antigen-specific cells: Type I IFN-
496 mediated bystander B cell activation, and a splenic B cell developmental pathway. Both these
497 processes occurred contemporaneously, and in the same organ as antigen-specific B cell
498 differentiation. Although long-term consequences of Type I IFN-mediated bystander

activation of naïve B cells was not determined here, previous work including our own, indicates systemic blockade of Type I IFN-signaling early during an immune response improves cellular and humoral immunity to malaria[32,81-84], and also during viral infection[85]. Whether Type I IFN-mediated effects on naïve B cells impairs subsequent immune responses to a new pathogen remains to be tested.

Plasmodium infection can impair haematopoiesis in the bone marrow, with negative consequences for myelopoiesis[86,87]. Common lymphoid progenitors are detected in adult mouse spleen[88], with one study suggesting these could undergo B cell development during *Plasmodium* infection[89]. Our study extends this by revealing various immature B cell states are readily detected in the spleen during malaria, and that the classical B cell developmental pathway is likely phenocopied in the spleen. Further work is required to elucidate whether these mature B cells have the propensity to participate in ongoing or *de novo* immunological responses.

In summary, we have identified multiple, overlapping biological phenomena within splenic B cells during infection with blood-stage *Plasmodium* parasites. Amid a backdrop of bystander activation, single naive B cells with initial specificity for parasites proliferate and exhibit a spectrum of intra-clonal functional diversification. This diversity is maintained and increased in the GC via a constant rate of SHM, and persistence of both switched and unswitched GC B cells. Finally, deleterious effects on B cell development in bone marrow[90] are counteracted by relocation to the spleen, potentially allowing the body to respond future immunological challenges.

522 **Limitations**

523 Although our temporal assessment of polyclonal B cells aimed to capture the transition of B
524 cells from one state to another, we were unable to identify an intermediate state between
525 activated B cells and plasmablasts. This may have been due to the relative sparsity of
526 timepoints at early stages of the immune response, rather than there being a lack of such an
527 intermediate state. Secondly, the reduced capacity to detect BCR sequence data for GC B
528 cells compared to plasmablasts prevented us from making unequivocal statements around
529 the probabilities and frequencies with which naive B cells opted for these two fates. Rather,
530 we restricted our conclusions to whether or not single clones giving rise to GC B cells could
531 bifurcate into plasmablasts. Thirdly, our FACS-sorting strategy would not have isolated long
532 lived plasma cells (LLPCs), meaning that plasma cell output from the GC could not be
533 comprehensively assessed[91]. Instead, we infer *Prg2*-expressing ASCs in the spleen[49] as
534 likely pre-plasma cells yet to down-regulate CD19 as described by others[50].

535

536

537 **Methods**

538 **Mice**

539 C57BL/6J mice were sourced from Animal Resources Centre (Perth, Western Australia,
540 Australia) and maintained under specific pathogen-free (SPF) conditions in the Bioresources
541 Facility (BRF) at The Peter Doherty Institute for Infection and Immunity (Melbourne, Victoria,
542 Australia). Mice were housed at an ambient air temperature of 19-22ºC and 40-70% humidity
543 with a 12-hour day/night cycle. OB1.Rag−/−.uGFP, CD23Cre-MyD88flox and nzEGFP mice
544 were bred in-house in the BRF of The Peter Doherty Institute for Infection and Immunity and
545 maintained under the same conditions described above. Unless stated otherwise, all
546 experimental mice used were female at 6-12 weeks old. All animal procedures were approved
547 by the University of Melbourne Animal Ethics Committee (1915018 and 28191).

548

549 **Infection**

550 Passage C57BL/6J mice were infected with a thawed vial of either *Plasmodium chabaudi*
551 *chabaudi* clone AS (*Pc*AS) or *Plasmodium yoelii* strain 17XNL (*Py*17XNL) infected RBC
552 stabilite. Once parasitemia reached 1-5%, blood was collected from passage mice by intra-
553 cardiac bleed into RPMI containing 5U/ml heparin. A total of 10^5 (*Pc*AS) or 10^4 (*Py*17XNL)
554 parasitized RBCs were injected into each experimental mouse via lateral tail vein injection.
555 For rechallenge, mice were infected with 10^7 parasitized RBCs via lateral tail vein injection,
556 28 days after primary infection with *Pc*AS.

557

558 **Parasitemia assessment**

559 Parasitemia measurements were carried out as described previously[33]. Briefly, tail vein
560 bleeds were performed to collect a drop of blood into RPMI containing 5U/ml of heparin.
561 Diluted blood samples were stained at room temperature, for 30 minutes in the dark, with a
562 combination of Hoechst 33342 (10µg/ml; Sigma-Aldrich) and Syto84 (5µM; Life
563 Technologies). 10 times the initial volume of cold RPMI was used to quench the staining. The
564 percentage of parasitized RBCs was determined as the proportion of
565 Hoechst$^+$ Syto84$^+$ RBCs measured using a LSRFortessa X-20 cytometer (BD).

566

567 **Anti-malarial drug treatment**

568 Artesunate (Guilin Pharmaceutical, kindly gifted by J. Moehrle) was made to 50mg/ml in 5%
569 sodium bicarbonate solution (in PBS) and diluted with 0.9% saline (Baxter) to form a 5mg/ml
570 solution of sodium artesunate. From day 7 post *Pc*AS infection, 1mg of sodium artesunate
571 was injected intra-peritoneally (i.p.) twice daily to day 9, then once a day from day 10 to day
572 16 and twice weekly from day 17 to day 42 post *Pc*AS infection, alternating left and right side

573 each i.p. injection. Additionally, from day 7 until day 42, mice received 70mg/l of
574 pyrimethamine (Sigma Aldrich) in the drinking water.

575

576 **CD4+ T cell depletion**

577 At 4 days prior to *Pc*AS infection, mice were administered 0.2mg of anti-CD4 depleting
578 monoclonal antibody (clone GK1.5, BioXcell) or isotype control antibody (clone LTF-2,
579 BioXcell) and a further 0.1mg dose was administered one day prior to infection. Antibodies
580 were administered by intra-peritoneal injection in 200µl sterile PBS.

581

582 **IFNAR1 blockade**

583 On the day of *Pc*AS injection, prior to infection, mice were administered 0.1mg of anti-IFNAR1
584 monoclonal antibody (clone MAR1-5A3, Leinco) or isotype control antibody (clone HKSP84,
585 Leinco) and a further 0.1mg dose on day 2 post infection. Antibodies were administered by
586 intra-peritoneal injection in 200µl sterile PBS.

587

588 **Intravenous Cell Labelling**

589 To differentiate between lymphocytes that are in circulation and those that are within tissue,
590 prior to spleen isolation, the mice were labelled with CD45.2 (clone 104, BioLegend)
591 fluorescently conjugated antibody. A total of 15µl CD45.2-APC antibody was made up to
592 200µl in sterile 1x PBS and administered to each mouse via lateral tail vein injection. After 5
593 minutes, mice were culled and spleens harvested.

594

595 **Adoptive transfer**

596 Uninfected spleens from OB1.Rag−/−.uGFP female donor mice were collected and
597 homogenised through 70µm cell strainers. Homogenates were incubated with red blood cell
598 (RBC) lysis buffer (Pharm Lyse, BD) for 3 minutes at room temperature. $15x10^6$ OB1 cells
599 were injected into each C57BL/6J recipient mouse by lateral tail vein injection in a volume of
600 200µl.

601 For adoptive transfer of splenic precursor B cells, firstly, nzEGFP and C57BL/6J mice were
602 infected with *Py*17XNL. At 21 dpi nzEGFP mouse spleens were collected, homogenised
603 through 70µm cell strainers and underwent red blood cell lysis using Pharm Lyse (BD).
604 Spleen homogenates were incubated with CD93-PE antibody (1:100) for 30 minutes on ice,
605 washed twice with FACS wash buffer (2% FCS, 1mM EDTA in PBS) and then incubated with
606 anti-PE MicroBeads (Miltenyi Biotec) (1:10) for a further 30 minutes on ice and then washed
607 twice with FACS wash. Each homogenate was then passed through a LS MACS column as
608 per the manufacturer's instructions (Miltenyi Biotec, 130-042-401) for positive enrichment of

609 CD93-PE cells. Enriched samples were pooled and cells were further sorted using a FACS
610 Aria III (BD) to eliminate contaminating ASCs or GC B cells. Each infection-matched
611 C57BL/6J recipient mouse received a total of 6-10x10^5 GFP^+ enriched splenic precursor B
612 cells by lateral tail vein injection in a volume of 200µl. Mice were left for 21 days before
613 assessment of adoptively transferred GFP^+ cells.

614

615 **Flow cytometry**

616 For bone marrow analysis, a single femur and tibia were isolated from each mouse. Bone
617 marrow was extracted by flushing the inside of each bone with cold 1x PBS. Isolated bone
618 marrow and spleens were homogenised through 70µm cell strainers and underwent red blood
619 cell lysis using Pharm Lyse (BD). After washing in 1x PBS, cells were stained with Zombie
620 Yellow live/dead stain (BioLegend) (1:500) in PBS on ice for 15 minutes, followed by Fc
621 receptor block (1:500) (BD) in FACS wash buffer (2% FCS, 1mM EDTA in PBS) on ice for 20
622 minutes. Finally, cells were stained with different titrated panels of monoclonal antibodies
623 diluted in FACS wash buffer (refer to table for antibody details). For intracellular staining,
624 surface-stained cells were fixed and permeabilised using FoxP3/Transcription Factor
625 Staining Set (eBiosciences) then stained with titrated antibody panels for 20-30 minutes on
626 ice in the dark. Cells were acquired using LSRFortessa X-20 cytometer (BD), with all analysis
627 of raw data performed using FlowJo version 5 (Treestar). Fluorescence minus one (FMO)
628 controls for SCA-1, Ly6C, IgM, IL7R, CXCR4, CD69, CD83, CD86, CCR6, B220 and CD19
629 were used to help draw gates for each marker.

630

Marker	Fluorophore	Clone	Source	Titration	Surface/ICS
B220	AF700	RA3-6B2	BioLegend	1:200	Surface
B220	BUV395	RA3-6B2	BD	1:200	Surface
CD19	PE-Cy7	6D5	BioLegend	1:200	Surface
CD19	PerCP-Cy5.5	1D3/CD19	BioLegend	1:200	Surface
CD19	FITC	6D5	BioLegend	1:200	Surface
CD24	PE-Cy7	M1/69	BioLegend	1:200	Surface
CD38	BUV737	90/CD38	BD	1:200	Surface
CD43	AF700	S11	BioLegend	1:100	Surface
CD69	PE-Cy7	H1.2F3	BD	1:200	Surface
CD83	PE	Michel-19	BioLegend	1:200	Surface
CD86	PE-Cy7	GL1	BD	1:200	Surface
CD86	APC-Cy7	GL-1	BioLegend	1:100	Surface

CD93	PE	AA4.1	BioLegend	1:200	Surface
CD95/Fas	PE-CF594	Jo2	BD	1:200	Surface
CD127/IL7R	BV421	A7R34	BioLegend	1:200	Surface
CD138	BV786	281-2	BD	1:100	Surface
CD184/CXCR4	BV421	2B11/CXCR4	BD	1:50	Surface
CD196/CCR6	PE	29-2L17	BioLegend	1:200	Surface
CD267/TACI	APC	ebio8F10-3	eBioscience	1:200	Surface
IgD	BV711	11-26c-2a	BioLegend	1:200	Surface
IgG2c	Biotin	5.7	BD	1:200	Surface
IgM	APC-Cy7	RMM-1	BioLegend	1:100	Surface
Ki67	FITC	SolA15	eBioscience	1:200	ICS
Ly6a/SCA-1	APC-Fire	D7	BioLegend	1:100	Surface
Ly6c	PE	HK1.4	BioLegend	1:100	Surface
Streptavidin	BV421	-	Biolegend	1:200	Surface
TCRβ	BUV737	H57-5797	BD	1:200	Surface

Antibody cloning

Selected BCR sequences (including ovalbumin, sequence adapted from[92]) were cloned into mouse IgG1 backbone expression vector for the heavy chain and mouse kappa backbone expression vector for light chain. Briefly:

1. Restriction Digestion: Cut heavy chain DNA and IgG1 vector with AgeI and SalI. Cut light chain mouse kappa light chain vector with AgeI and BsiWI (New England Biolabs). At 37ºC for 2 hours, then run on an agarose gel.
2. Gel purification: DNA is extracted from the gel (Zymo Research D4001)
3. Ligation: Ligate each DNA fragment into corresponding expression vectors with T4 ligase (NEB M0202S) at 4ºC overnight.
4. Transformation: Heat shock ligated DNA at 42ºC for 90 seconds into DH5α competent cells
5. Miniprep plasmid purification (Zymo Research D4212)
6. Sequence verification by AGRF (Australian Genome Research Facility)
7. Maxiprep plasmid purification (Zymo Research D4202)

Antibodies were expressed by transient transfection into mammalian Expi293F cells using Expi-Fectamine (A14525, Thermo Fisher Scientific) with heavy and light chain plasmid (1:1 ratio) and purified by Protein G column chromatography (29048581 GE), followed by buffer-exchange into PBS. Butyrophilin antibody was synthesised previously[93] as per clone sequence from[94].

Preparation of naive and parasitised RBC lysates

Parasitised antigen extract from infected blood was carried out as described previously[95,96]. Briefly, blood was collected from infected mice when blood parasitemia reached 20–30%. Blood was collected by intra-cardiac bleed into RPMI containing 5U/ml heparin. RBCs were washed once in RPMI at 400xg for 7 minutes at room temperature, before using ultrapure water to lyse, followed by four washes in ice-cold PBS at 16,000xg for 25 minutes at 4ºC, followed by three cycles of freezing (two hours at -80ºC) and thawing (30 minutes at room temperature). This procedure was followed by disruption (twice for 30s) with an ultrasonic probe at 60W on ice. Protein extracts were also processed from RBCs of uninfected C57BL/6J mice, to serve as negative controls in ELISA. Bradford assay (Thermo Fisher Scientific) was used to determine the concentration of proteins in the purified extracts.

***Plasmodium*-specific IgG ELISA**

As described previously[96], Costar EIA/RIA 96-well flat bottom plates were coated overnight at 4ºC with 10µl of parasite antigen (20µg) in bicarbonate coating buffer (pH9.6). Wells were washed three times with 0.05% Tween-20 in PBS and then blocked for 1 hour at 37ºC with 1% skim milk in PBS. Wells were washed three times, followed by incubation with 5µg of purified cloned antibody for 1 hour at 37ºC. Following six washes, wells were incubated in the dark with goat anti-mouse IgG HRP (G21040) for 30 minutes at room temperature. Wells were washed six times prior to development (100µl, OPD; P9187 Sigma-Aldrich) for five minutes in the dark before termination with an equal volume of 1M HCl. Absorbance was determined at 492nm using CLARIOstar analyser (BMG Labtech).

Serum was collected from uninfected and infected mice (day 55-60 post-*Pc*AS) with or without anti-malarial drug treatment and diluted 1/400, 1/800, 1/1600 or 1/3200 to assess binding to crude antigen extracts from *Pc*AS-infected pRBCs, as previously described[96].

Cell sorting and scRNAseq

Spleens were harvested from mice and homogenised through 70µm cell strainers. RBCs were lysed using Pharm Lyse (BD) for 3 minutes at room temperature and then single cell suspensions washed twice in 1x PBS. Samples were then incubated with Fc receptor-blocking antibodies (1:500) (BD) for 20 minutes on ice, followed by incubation with titrated monoclonal fluorescently conjugated antibodies and TotalSeq-C (BioLegend) mouse

686 hashtags for 20 minutes on ice. Cells were washed twice and resuspended with propidium
687 iodide (1:500) in PBS 2% BSA.

688 For experiment 1, samples from five individual mouse replicates were pooled together for
689 each timepoint. Note, for timepoint day 4 post infection, there were four separately infected
690 mice with one uninfected naive sample pooled in. Live, TCRβ negative, $CD19^{+}$, $B220^{int\text{-}hi}$ cells
691 were sorted using a FACS Aria III (BD) into a 2% BSA/PBS buffer. For experiment 2, samples
692 from seven individual mice (three for *Pc*AS, three for *Pc*AS+drug and one uninfected) were
693 pooled together for each timepoint. Live, TCRβ negative, $CD19^{+}$, $B220^{int\text{-}hi}$, IgD^{lo} cells were
694 sorted using a FACS Aria III (BD) into a PBS 2% BSA buffer. For each sample, a small number
695 of IgD^{hi} naive cells were spiked in to assist in removal of batch effects for downstream
696 scRNAseq analysis. For experiment 3, a single representative spleen was chosen from a 14
697 dpi mouse. Live, $CD19^{+}$, $B220^{int\text{-}hi}$ were sorted into either $CD138^{+}$ IgD^{-} ASCs or $CD38^{-}$ Fas^{+}
698 GC B cells at 1:1 ratio. A small number of IgD^{hi} naive cells were spiked in.

699 After sorting, cells were loaded onto the Chromium controller and cDNA-sequencing libraries
700 were prepared using the Chromium Single Cell 5' Kits (10X Genomics).

701

702 **Analysis of scRNAseq datasets**

703 For experiments 1 (days 0-14) and 2 (days 10-42), the transcriptome of splenic B cells was
704 aligned using Cell Ranger 3.1.0 (10X Genomics) against mouse genome v2020-A (10X
705 Genomics). For experiment 3, the transcriptome of splenic B cells was aligned using Cell
706 Ranger 9.0.1 (10X Genomics) against mouse genome GRCm39-2024-A (10X Genomics).
707 Hashtag demultiplexing and pre-processing of the data was performed using R version 4.2.0
708 (experiment 1 and 2) or version 4.3.1 (experiment 3) and Seurat version 4[97]. Doublets and
709 negatives were removed from the demultiplexed samples for further downstream analysis
710 (Supplementary Method Fig. 1A and 2A). For pre-processing, cells with a mitochondrial gene
711 content of greater than 10% (experiment 1 and 2) or greater than 20% (experiment 3) were
712 removed as well as cells with fewer than 200 and greater than 6000 total gene expression
713 (Supplementary Method Fig. 1B and 2B).

714

715 Normalisation of data, selection of highly variable features and scaling of data were achieved
716 using the *SCTransform()* function using default settings. Dimensional reduction was
717 performed using the *RunPCA()* function and the resultant principal components were inputted
718 to perform unifold manifold approximation and projection (UMAP) using *RunUMAP()* function.
719 Finally, *FindNeighbours()* function and *FindClusters()* functions were used for unsupervised
720 clustering.

721

722 Additionally, if immunoglobulin genes were left in the dataset for high dimensional reduction
723 and clustering, clusters formed based purely on certain immunoglobulin variable heavy or

light chain regions (Supplementary Method Fig. 1C and 2C). Therefore, immunoglobulin related genes (list of genes in Supplementary Table 2) were removed from the high dimensional reduction and clustering analysis, as recommended previously[98]. After high dimensional reduction and clustering analysis, UMAPs of each experiment were generated which highlighted anomalous cell clusters in each dataset: high mitochondrial content clusters, monocytes (*Lyz2*) and additionally in experiment 2, T cells (*Cd3g*) and erythrocytes (*Hbb-bs*) (Supplementary Method Fig. 1D and 2D). These clusters were removed from the UMAPs for subsequent downstream analysis. Altogether, after these quality control approaches, there were a total of 112,982 B cells: 40,623 B cells from experiment 1 and 72,359 B cells from experiment 2. A total of 19,482 post-QC B cell transcriptomes from a single mouse were retrieved from experiment 3.

Cell type annotation

Differential gene expression analysis was performed using the *FindMarkers()* function with Wilcoxon rank sum test used to identify statistically significant differentially expressed genes across clusters. Geneset enrichment analysis (GSEA) was performed against biological processes GO terms using ToppGene Suite[99] or WebGestalt[100]. Gene signatures were sourced from publicly available datasets for the following signatures: cell cycle[101], class switch recombination (CSR)[27], GC B cell subsets[46] and B1a cells[102]. These cluster gene lists in addition to GSEA analysis and gene signatures aided in cell annotation of clusters for each UMAP.

Sub-clustering

To further sub-cluster ASC and GC B cell subsets, each subset were taken separately and the above workflow repeated, i.e. normalisation, *SCTransform(), RunPCA(), RunUMAP(), FindNeighbours()* and *FindClusters().*

Data integration

Single-cell variational inference (scVI)[103] was used to account for batch effects when performing data integration of day 10-42 B cell dataset with publicly available scRNAseq data of bone marrow B cells[52]. All parameters were kept at default and number of epochs set to 30 to train the model. Latent variables were used as input to run UMAP using Scanpy package (v1.9.1)[104]. In addition, data integration was performed on experiment 1 and 2 B cell datasets to generate a combined scRNAseq B cell dataset using the above parameters but using 9 epochs to the train the integration model.

Bayesian Gaussian Process Latent Variable Model (bGPLVM)

761 Pseudo-temporal ordering of activated and GC B cells was performed using Bayesian
762 Gaussian Process Latent Variable Model (BGPLVM) using GPFates[37]. This generated a
763 progression of activated and GC B cell transcriptomes that correlated with sampled
764 timepoints as well as an inferred pseudotime trajectory.

765

766 **Spatial transcriptomics using *Slide-seqV2***

767 Spatial transcriptomics was performed using *Slide-seqV2* at the Broad Institute of Harvard
768 and MIT, as described elsewhere[105]. The methodology for the following spatial transcriptomic
769 datasets were performed as previously described[39,106] and analysis performed on previously
770 published data[39].

771

772 **Spatial transcriptomics using *Stereo-seqV1.2***

773 *Pc*AS infected spleens were isolated from 21 dpi mice and fresh frozen in liquid nitrogen,
774 embedded in Tissue-Tek® O.C.T Compound (Sakura) and stored at -80ºC. *Stereo-seqV1.2*
775 (BGI) was performed as per manufacturer's instructions and two independent mouse
776 spleens. Briefly, once appropriate red and white pulp regions were located within the spleen,
777 a 10µm cryosection was mounted onto a spatially barcoded 1x1cm chip. A serial cryosection
778 was collected to confirm spleen morphology via H&E staining. Spleen sections on chips were
779 fixed with 4% PFA (BioScientific) followed by DAPI (Thermo Fisher Scientific) staining for 2
780 minutes. Chips were imaged using an Axioscan 7 microscope (Zeiss). Following imaging,
781 tissue permeabilisation was conducted for 8 minutes as determined by preliminary
782 permeabilisation tests. cDNA-sequencing libraries were prepared and sequenced data was
783 processed following STOmics *Stereo-seq* Analysis Workflow (SAW) pipeline.

784

785 **Spatial deconvolution**

786 Spatial deconvolution was achieved using robust cell type decomposition (RCTD) algorithm
787 on day 21 *Pc*AS infected spleens (*Stereo-seqV1.2*) and on publicly available *Slide-seqv2* day
788 30 *Pc*AS infected spleens with artesunate treatment[107] (n=4, two spatial transcriptomic arrays
789 per spleen for two infected mice). The single cell transcriptomic references used were from
790 the day 10-42 B cell dataset (experiment 2). In addition, our reference contained CD4, CD8
791 T cells, NK cells, macrophages, monocytes, erythrocytes, granulocytes, cDC1s, cDC2s and
792 pDCs from an uninfected spleen reference dataset[106] and GC-Tfhs from a day 30 infected
793 *Pc*AS reference[39]. Finally, our reference contained cells from a publicly available spleen
794 stromal dataset from uninfected mice, which included fibroblastic reticular cells (FRCs),
795 follicular dendritic cells (FDCs), red pulp reticular cells (RPRCs) and adventitial reticular cells
796 (ARCs)[53]. For cell-cell co-localisation analysis, we defined spatial neighbourhoods with a
797 radius of 50µm. Spearman correlations are then calculated for all cell type pairs from the
798 reference data and visualised as a heatmap.

BCR sequencing and analysis

Dandelion package[42] was used for VDJ clonal analysis.

Pre-processing

Using Dandelion, the data was pre-processed using the standard outputs from all cellranger vdj versions. Here, single-cell V(D)J data from the 5′ Chromium 10X kit were initially processed with cellranger vdj pipeline (v6.1.2). BCR contigs contained in ‘all_contigs.fasta’ and ‘all_contig_annotations.csv’ files were then re-annotated using an immcantation-inspired pre-processing pipeline contained in the Dandelion singularity container (v0.3.0).

The pre-processing pipeline includes the following steps:

1. Adjust cell and contig barcodes by adding user-supplied suffixes and/or prefixes to ensure that there are no overlapping barcodes between samples.
2. Re-annotation of contigs with igblastn (v1.19.0) against IMGT (international ImMunoGeneTics) reference sequences.
3. Re-annotation of *D* and *J* genes separately using blastn with similar parameters as per igblastn (dust = ‘no’, word size (J = 7; D = 9)) but with an additional *e*-value cutoff (J = 10^{-4} in contrast to igblastn’s default cutoff of 10; D = 10^{-3}). This is to enable the annotation of contigs without the *V* gene present.
4. Identification and recovery of nonoverlapping individual *J* gene segments (under associated ‘j_chain_multimapper’ columns). In the list of all mapped *J* genes (all_contig_j_blast.tsv) from blastn, the *J* gene with the highest score (j_support) was chosen. Dandelion then looks for the next *J* gene with the highest ‘j_support’ value, and with start (j_sequence_start) and end (j_sequence_end) positions not overlapping with the selected *J* gene, and does so iteratively until the list of all mapped *J* genes are exhausted. In contigs without *V* gene annotations, it then selects the 5′ end leftmost *J* gene and update the ‘j_call’ column in the final AIRR table. For contigs with *V* gene annotations, but with multiple *J* gene calls, it uses the annotations provided by igblastn.

For BCRs, there are two additional steps:

1. Additional re-annotation of heavy-chain constant (C) region calls using blastn (v2.13.0) against curated sequences from CH1 regions of respective isotype class.
2. Heavy chain *V* gene allele correction using TIgGER (v1.0.0). The final outputs are then parsed into AIRR format with change-o scripts.

The rearrangement sequences that pass standard quality control checks are saved in file ending with the suffix '_contig_dandelion.tsv'.

Postprocessing

In addition to the pre-processing steps at the contig level, postprocessing or integrating cell-level quality control is performed using Dandelion's 'check_contig' function. The function checks whether a rearrangement is annotated with consistent *V*, *D*, *J* and *C* gene calls and performs special operations when a cell has multiple contigs. All contigs in a cell are sorted according to the unique molecular identifier (UMI) count in descending order, and productive contigs are ordered higher than non-productive contigs. For cells with other than one pair of productive contigs (one VDJ and one VJ), the function will assess if the cell is to be flagged with having orphan (no paired VDJ or VJ chain), extra pair(s) or ambiguous (biologically irreconcilable, for example, both BCRs in the same cell) status with an exception that IgM and IgD are allowed to coexist in the same B cell if no other isotypes are detected. The function also asserts a library type restriction with the rationale that the choice of the library type should mean that the primers used would most likely amplify only relevant sequences to a particular locus. Therefore, if there are any annotations to unexpected loci, these contigs likely represent artifacts and will be filtered away. A more stringent version of 'check_contigs' is used here by a separate function, 'filter_contigs', which only considers productive VDJ contigs, asserting a single cell should only have one VDJ and one VJ pair, or only an orphan VDJ chain, and explicitly removes contigs that fail these checks (with the same exceptions for IgM/IgD as per above). Productive contigs are selected for downstream analysis (Supplementary Methods Fig. 3A-B). Summary of frequency of unexpanded and expanded clones for each timepoint and experiment can be found in Supplementary Method Fig. 3.

Clonotype definition and diversity

BCRs were grouped into clones/clonotypes using a sequential, rule-based procedure applied to productive rearrangements and implemented within Dandelion/Change-O outputs. Briefly, after cell-level QC (mentioned above), each cell contributed at most one dominant productive VDJ (heavy) and one productive VJ (light; IGK/IGL) contig (selected by UMI count), and clonotypes were assigned as follows:

1. **Chain-aware grouping (heavy and light):** Heavy- and light-chain repertoires were clonotyped separately using the criteria below, and paired clonotypes were defined using the combined heavy+light signature when both chains were available.

2. **Shared V/J gene usage:** Sequences were first required to have identical V-gene and J-gene calls (gene-level calls, not allele-level unless otherwise stated) for the relevant chain.

3. **Matched junction length:** Within each V/J bin, sequences were required to have identical CDR3 (junction) amino-acid length, ensuring a like-for-like comparison across aligned CDR3s.
4. **CDR3 similarity threshold:** Sequences passing (1–3) were then clustered by CDR3 amino-acid sequence similarity using a Hamming-distance criterion (equal-length CDR3s), with clonotype membership requiring ≥85% amino-acid identity.
5. **Handling incomplete receptors:** Cells lacking an unambiguous productive chain (e.g., missing light chain or orphan heavy chain) were clonotyped using the available productive chain only, and were excluded from analyses requiring paired heavy+light definition.

Diversity was quantified from the resulting clonotype frequency tables (counts of cells per clonotype within each sample/timepoint/condition). Clonal expansion was summarised by the distribution of clone sizes (e.g., unexpanded singletons versus expanded clones), and repertoire diversity was computed using standard clonotype-based diversity metrics (e.g., Shannon entropy and/or Simpson diversity) on depth-normalised clonotype tables to enable fair comparisons across samples.

Somatic Hypermutation (SHM)

The basic mutation load is quantified by using the 'pp.quantify_mutations' in Dandelion which is a wrapper of SHaZam's basic mutational analysis. It sums all mutation scores (heavy and light chains, silent and replacement mutations) for the same cell.

GC B cell mutation analysis

Mutation rate analysis is calculated by fitting linear regression line to the median number of mutations at each timepoint for each condition (*Pc*AS or *Pc*AS+drug). The gradient of the line provides the mutation rate per day. Mutation rate analysis was also performed specifically on the Ighv region of the BCR in comparison with publicly available clonal data from lymph node GC B cells after influenza infection[25,48].

GUI Architecture

An interactive B cell GUI was developed using Dash (pyDash), which couples a Flask-based Python back end to a React-based front end, with all layouts and interactions defined in a single Python codebase. Interactive visualisation was implemented with Plotly, enabling hover-based inspection, zooming, brushing/linked filtering, and export across modules (B cell dynamics, gene expression, violin plots, clonality, and spatial views). Single-cell RNA-seq and paired BCRseq data were curated into an AnnData/HDF5 data model with harmonized metadata (treatment, timepoint, cell type, clonotype, isotype and SHM metrics).

To minimise runtime costs, 2D/3D UMAP embeddings and key summary metrics were pre-computed, and frequently queried metadata fields were indexed to support rapid subsetting in callbacks. For usability at scale, lightweight aggregation was applied where appropriate and the dataset was down-sampled explicitly retaining cells with BCR information to maintain a smooth, responsive user experience.

Plotting

For data visualisation, the following packages were used: Prism version 9, Tableau (2023.2.0), Python version 3.8.8 or ggplot2 version 3.4.4 package utilised in R version 4.2.1. Adobe Illustrator version 26.3.1 was used for figure generation and schematics were partly generated using BioRender.

Data availability

Raw sequencing data for scRNAseq B cell data for experiments 1, 2 and 3 and two independent *Stereo-seqV1.2* spleen samples are found via accession number provided: GSE286215 and can be accessed using reviewer's token *cnaduagirzinval*. Processed data including contig annotations of BCR data, Seurat objects of all experiments and integrated Seurat object are also found via accession number: GSE286215 and can be accessed using reviewer's token *cnaduagirzinval*. Previously published data used in this present study can be found here: spleen stromal scRNAseq data for spatial deconvolution (GSE171124), T cell scRNAseq data for spatial deconvolution (GSE244806, GSE233713), *Slide-seqV2* spatial transcriptomics data (GSE234253), B cell bone marrow scRNAseq data (GSE168158).

Code availability

Publicly available software was used, as detailed in the methods and reporting summary. Code can be provided upon request.

Ethics declarations

The authors declare no competing interests.

Acknowledgements

This research was supported by The University of Melbourne's Research Computing Services, the Petascale Initiative, and the LIEF HPC-GPGPU Facility hosted at The University of Melbourne. The facility was established with the assistance of LIEF grant LE170100200. We extend our gratitude to the Bioresources Facility located at The Peter

Doherty Institute for Infection and Immunity for their animal care and assistance. We are also deeply thankful to the Doherty Institute node of the Melbourne Cytometry Platform at The University of Melbourne. We acknowledge the Hudson Genomics Facility for sequencing of single cell data. We would also like to acknowledge Dr Katherine Jackson (Garvan Institute of Medical Research, Sydney, Australia) for discussions and help regarding BCR sequencing analysis. A thank you also goes towards Dr Nick (Ka Leung) Li and Dr Jiyoti Verma from Decode Science for assistance and support with the *Stereo-seqV1.2* experiments as well as the Biological Optical Microscopy Platform at the University of Melbourne. The authors acknowledge the South Australian Genomics Centre (SAGC) for sequencing the *Stereo-seqV1.2* libraries. The SAGC is supported by the National Collaborative Research Infrastructure Strategy (NCRIS) via Bioplatforms Australia. We finally acknowledge Joshua Lilley at The University of Melbourne for assistance with deployment of the GUI that accompanies this resource.

Main Figures

Figure 1

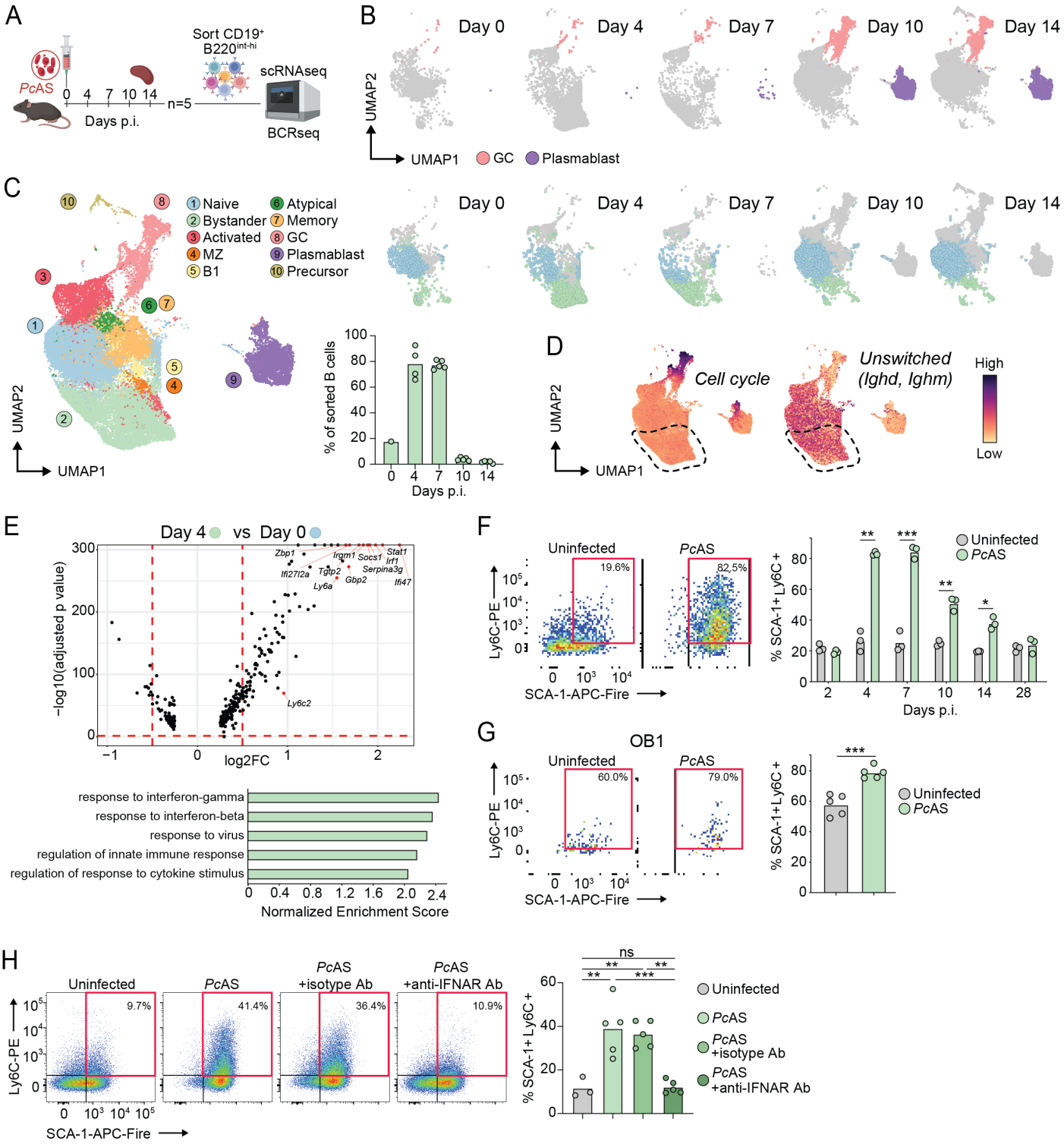

Figure 1: **Plasmablast and GC B cell differentiation temporally overlaps Type I IFN-mediated bystander activation during experimental malaria.**

(**A**) Experimental plan to study B cell differentiation in *Pc*AS-infected mice. Splenic $CD19^{+}$ $B220^{int\text{-}hi}$ B cells were isolated at various timepoints post-infection and underwent droplet-based, paired single cell RNA and BCR sequencing. (**B**) High-dimensional clustering UMAP of GC B cells (pink) and plasmablasts (purple). (**C**) UMAP plot of combined B cell populations across all (left) or specific timepoints (right) with the two follicular B cell subsets; naive (blue) and bystander (green) and all other B cells (grey). Frequency of bystander B cells at each timepoint are indicated by the bar graph (middle). (**D**) Gene signature feature plots of cell cycle or unswitched signatures (dashed lines highlight bystanders). (**E**) Volcano plot highlighting the top differentially upregulated genes in red expressed in follicular (day 4) compared to naïve (day 0) clusters. Gene set enrichment analysis (GSEA) highlights the top five significantly enriched biological processes gene ontology (GO) terms. (**F**) Representative pseudocolour density plots of SCA-1 and Ly6C expression ("bystander markers") in IgD^{+} B cells at day 4 post-*Pc*AS infection (left) and bar graph of $SCA\text{-}1^{+}$ $Ly6C^{+}$ cell frequencies amongst IgD^{+} B cells over time (right). (**G**) Representative pseudocolour density plots (left) and bar graph (right) showing proportion of SCA-1 and Ly6C expression on $CD86^{lo}$ OB1 adoptively transferred B cells at 4 days post-*Pc*AS infection. (**H**) Representative pseudocolour density plots (left) and bar graph (right) of SCA1 and Ly6C-expressing IgD^{hi} $CD19^{+}$ $B220^{+}$ B cell frequencies at day 4 post-*Pc*AS infection in the presence of continual anti-IFNAR antibody blockade or isotype control. Data from bar graphs in C-H represent the mean, where F-G were compared using Welch's *t*-test and H by one-way ANOVA with Tukey's multiple comparisons test. All experiments are representative of two independent experiments of n = 3-5 per group. $^{*}P < 0.05$, $^{**}P < 0.01$, $^{***}P < 0.001$. ns, not significant.

Figure 2

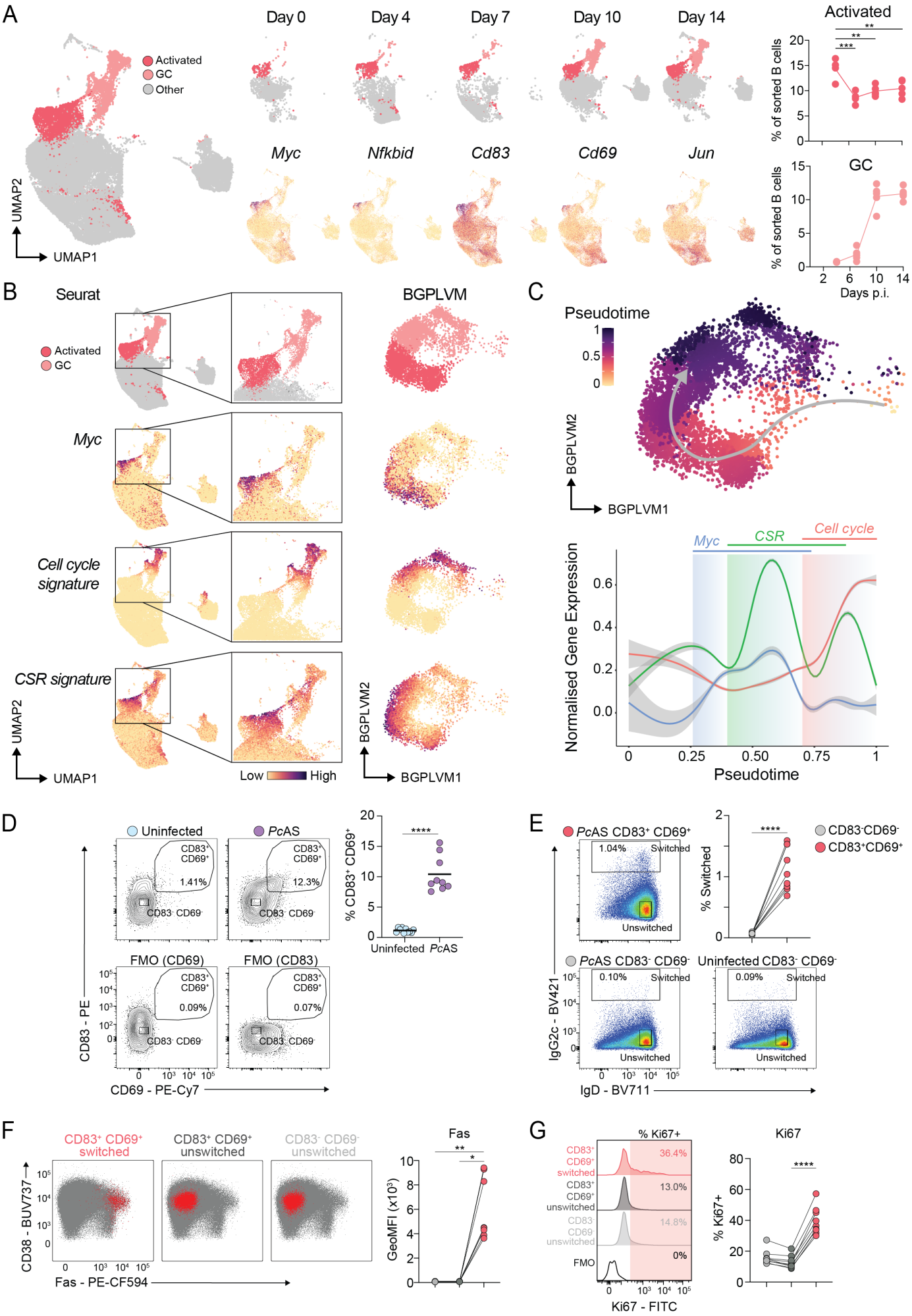
A
Activated
GC
Other
UMAP2
UMAP1
Day 0
Day 4
Day 7
Day 10
Day 14
Myc
Nfkbid
Cd83
Cd69
Jun
Activated
GC
% of sorted B cells
Days p.i.
B
Seurat
BGPLVM
Activated
GC
Myc
Cell cycle signature
CSR signature
UMAP2
UMAP1
Low
High
BGPLVM2
BGPLVM1
C
Pseudotime
BGPLVM2
BGPLVM1
Myc
CSR
Cell cycle
Normalised Gene Expression
Pseudotime
D
Uninfected
PcAS
CD83+ CD69+
1.41%
12.3%
CD83- CD69-
FMO (CD69)
FMO (CD83)
0.09%
0.07%
CD83 - PE
CD69 - PE-Cy7
% CD83+ CD69+
Uninfected
PcAS
E
PcAS CD83+ CD69+
1.04%
Switched
Unswitched
% Switched
CD83-CD69-
CD83+CD69+
PcAS CD83- CD69-
Uninfected CD83- CD69-
0.10%
0.09%
IgG2c - BV421
IgD - BV711
F
CD83+ CD69+ switched
CD83+ CD69+ unswitched
CD83- CD69- unswitched
CD38 - BUV737
Fas - PE-CF594
Fas
GeoMFI (x10³)
G
% Ki67+
CD83+ CD69+ switched
CD83+ CD69+ unswitched
CD83- CD69- unswitched
FMO
36.4%
13.0%
14.8%
0%
Ki67 - FITC
Ki67
% Ki67+

Figure 2: CSR occurring soon after *Myc*-upregulation overlaps with clonal expansion.

(**A**) Annotated B cell UMAP (left) of activated (indicated by activation marker gene expression: *Myc, Nfkbid, Cd83, Cd69* and *Jun*) and GC B cells after high-dimensional reduction. Clustering is additionally split by each timepoint (middle) with quantitation of replicate mice across time for activated and GC B cells (right). (**B**) Feature plots of *Myc* expression, Class Switch Recombination (CSR) and cell cycle gene signatures across Seurat and Bayesian Gaussian Process Latent Variable Model (BGPLVM) embedding methods. (**C**) Pseudotime trajectory analysis of BGPLVM object using GPFates, including *Myc*, CSR signature and cell cycle signature-normalised expression along pseudotime. (**D**) Representative contour plots (left) and scatter plot (right) of $CD83^+$ $CD69^+$ activated B cell frequencies as gated on $CD19^+$ $B220^+$, non-GC B cells and non-PBs, in uninfected and *Pc*AS (4 dpi) from total B cells. Activated B cell gates were drawn based on $CD69^-$ and $CD83^-$ FMOs. (**E**) Representative pseudocolour density plots (left) of $IgG2c^+$ switched $CD83^+$ $CD69^+$ (activated) and $CD83^-$ $CD69^-$ B cells frequencies (right) from *Pc*AS-infected samples. (**F**) Representative dot plots (left) of Fas expression in selected cell populations (highlighted in red) and line graph (right) of geometric mean fluorescence intensity (GeoMFI) of Fas in populations of $CD83^+$ $CD69^+$ switched, $CD83^+$ $CD69^+$ unswitched, and $CD83^-$ $CD69^-$ unswitched B cells. (**G**) Representative histograms (left) and line graph (right) of % $Ki67^+$ cells in populations of $CD83^+$ $CD69^+$ switched, $CD83^+$ $CD69^+$ unswitched and $CD83^-$ $CD69^-$ unswitched B cells. $Ki67^+$ gate drawn based on $Ki67^-$ FMO. Lines connect the mean value in panel a at each timepoint and analysed by one-way ANOVA with Tukey's multiple comparisons test. Data in panel D-G is pooled from two independent experiments of n = 9-10 per group. Data in panel D represents the mean and analysed using Welch's *t*-test. Data in panel E analysed using a paired *t*-test. Data in panels F-G analysed using Friedman test with Dunn's multiple comparisons test. *P <0.05, **P <0.01, ***P <0.001, ****P <0.0001.

Figure 3

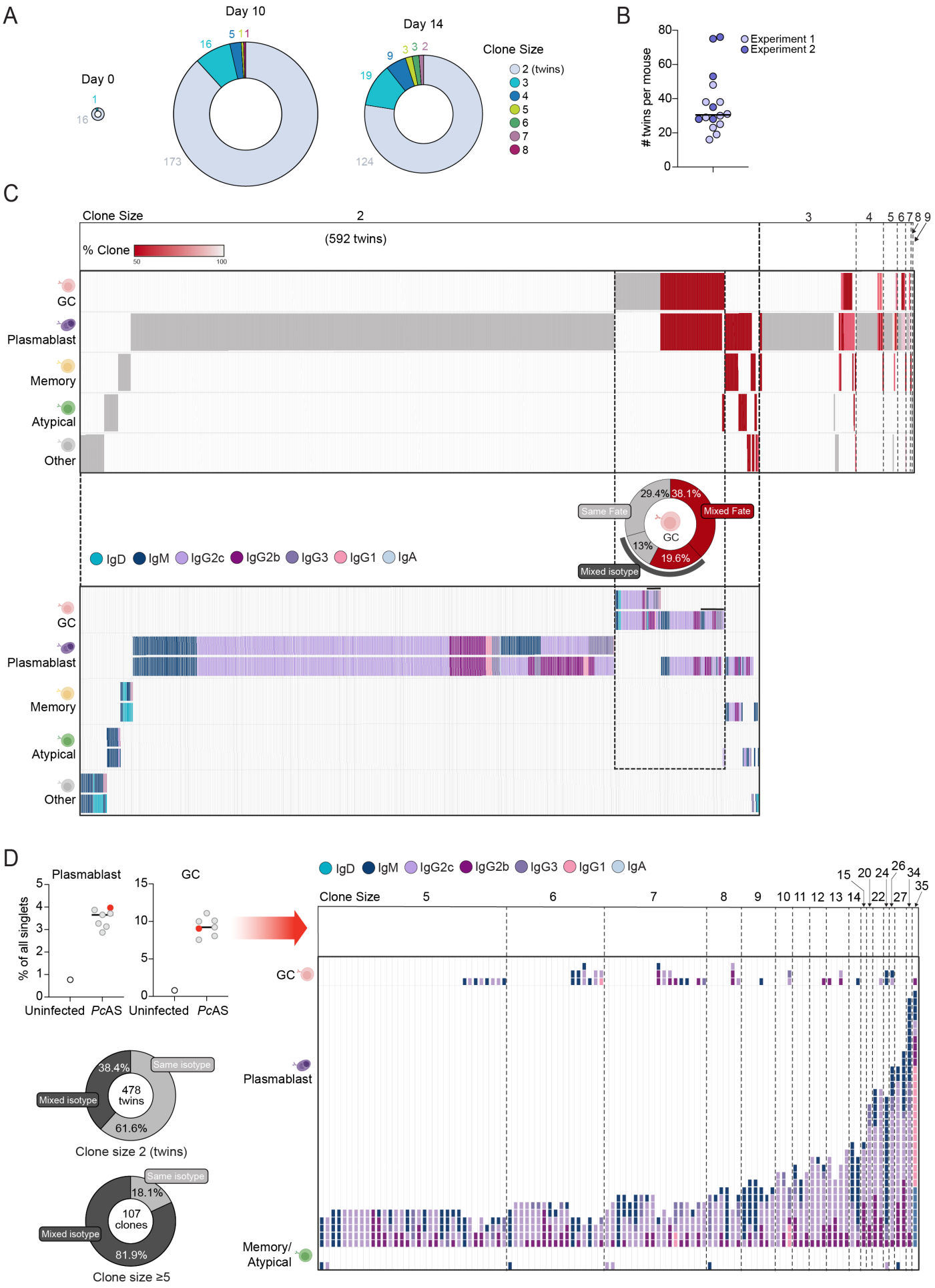
A
Day 0
1
16
Day 10
16
5 1 1
173
Day 14
19
9
3 3 2
124
Clone Size
2 (twins)
3
4
5
6
7
8
B
twins per mouse
80
60
40
20
0
Experiment 1
Experiment 2
C
Clone Size
2
(592 twins)
3
4
5 6 7 8 9
% Clone
50
100
GC
Plasmablast
Memory
Atypical
Other
29.4%
38.1%
Same Fate
Mixed Fate
GC
13%
19.6%
Mixed isotype
IgD IgM IgG2c IgG2b IgG3 IgG1 IgA
D
Plasmablast
GC
% of all singlets
Uninfected PcAS Uninfected PcAS
38.4%
Same isotype
Mixed isotype
478
twins
61.6%
Clone size 2 (twins)
Same isotype
18.1%
107
clones
Mixed isotype
81.9%
Clone size ≥5
IgD IgM IgG2c IgG2b IgG3 IgG1 IgA
Clone Size
5
6
7
8
9
10 11 12 13 14
15 20 24 26 34
22 27 35
GC
Plasmablast
Memory/
Atypical

Figure 3: Activated B cell clones seeding GCs bifurcate into plasmablasts and exhibit isotype variegation.

(**A**) Donut plots highlighting clone size distribution of expanded B cell clones detected at 0, 10 and 14 dpi. Size of donut plot is proportional to number of expanded clones at each timepoint. (**B**) scatter plot of the number of twin clones detected per mouse at 10 and 14 dpi from two experiments. (**C**) Clonal fates ordered by clonal size of plasmablast, GC, memory, atypical and other B cell subsets at 10 and 14 dpi. Each row represents cell fate, and each column represents the frequency of cells per clone. Clones are split by same fate (grey) and mixed fate (red). Donut plot represents quantification of same (grey) and mixed fates (red) in GC-containing clones of size 2. Clones of size 2 (of which there were 592 twins in total) were further analysed for their isotype in each cell, with donut chart of same and mixed isotypes (denoted with thick black line) for each clone with same (grey) and mixed fate (red) outcomes. (**D**) A single mouse spleen which had representative proportion of plasmablasts and GC B cells at 14 dpi (denoted in red), underwent paired single cell RNA and BCR sequencing (left). Plot on the right highlights the 107 expanded clones (≥ 5). Each column represents a clone, and each row depicts the cell fate within each clone, coloured by isotype. Donut charts highlight the proportion of clones (twins or clones greater than 5) with same and mixed isotypes.

Figure 4

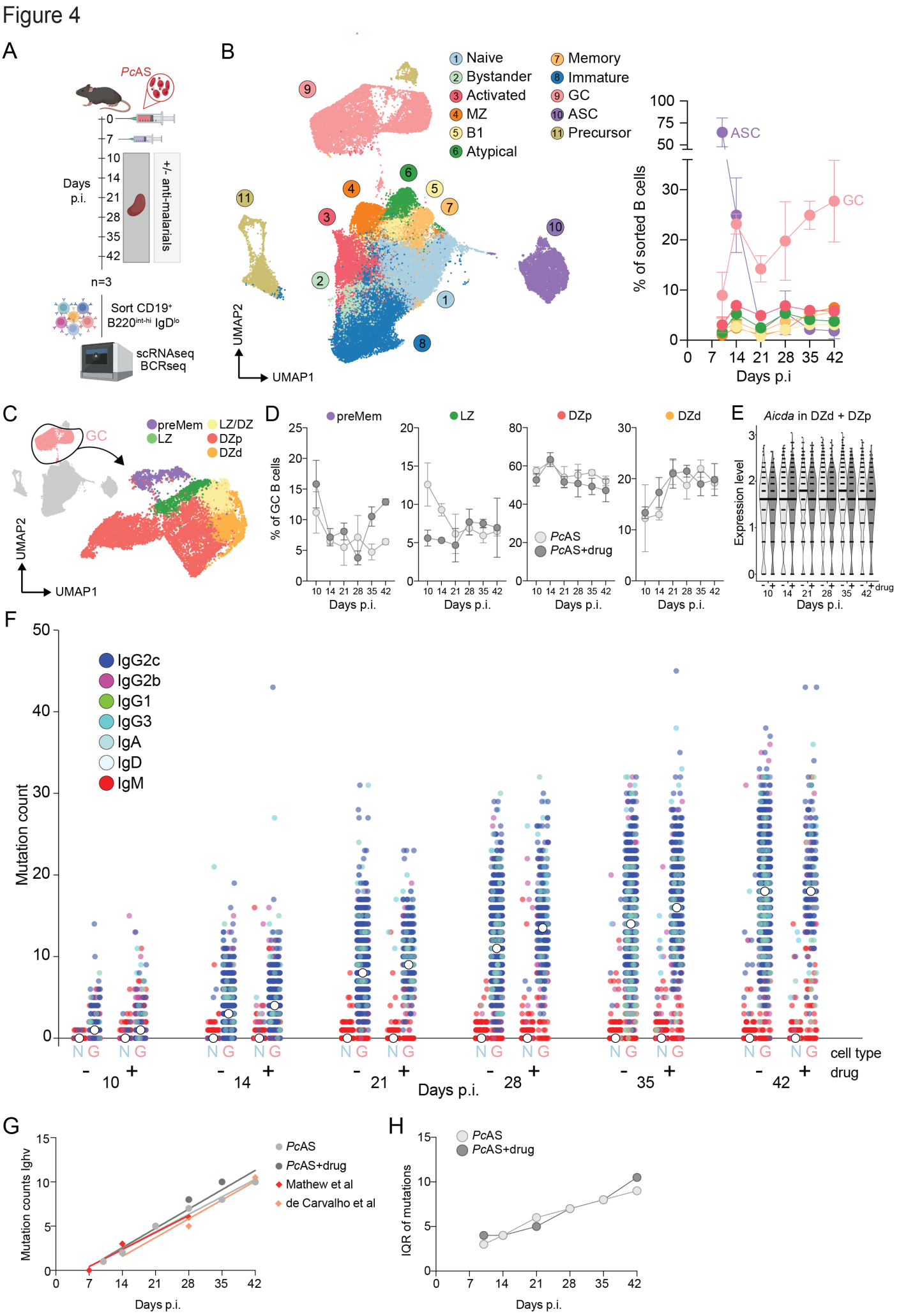
A
PcAS
Days p.i.
0
7
10
14
21
28
35
42
+/- anti-malarials
n=3
Sort CD19+ B220int-hi IgDlo
scRNAseq BCRseq
B
1 Naive
2 Bystander
3 Activated
4 MZ
5 B1
6 Atypical
7 Memory
8 Immature
9 GC
10 ASC
11 Precursor
UMAP2
UMAP1
ASC
GC
% of sorted B cells
Days p.i
C
GC
preMem
LZ
LZ/DZ
DZp
DZd
UMAP2
UMAP1
D
preMem
LZ
DZp
DZd
% of GC B cells
PcAS
PcAS+drug
Days p.i.
E
Aicda in DZd + DZp
Expression level
drug
Days p.i.
F
IgG2c
IgG2b
IgG1
IgG3
IgA
IgD
IgM
Mutation count
N G
cell type
drug
Days p.i.
G
Mutation counts Ighv
PcAS
PcAS+drug
Mathew et al
de Carvalho et al
Days p.i.
H
PcAS
PcAS+drug
IQR of mutations
Days p.i.

Figure 4: GC B cells progressively diversify via a constant SHM rate and retention of isotype diversity.

(**A**) Experimental plan to study B cell differentiation in *Pc*AS-infected mice, with or without anti-malarial drug treatment. $CD19^{+}$ $B220^{int\text{-}hi}$ IgD^{lo} splenic B cells isolated at various timepoints post-infection underwent droplet-based, paired single cell RNA and BCR sequencing. (**B**) Annotated combined UMAP of B cell subsets from all mice, treatments and timepoints after high-dimensional reduction and clustering (left), and line graph (right) of selected, annotated B cell frequencies over the course of *Pc*AS infection without anti-malarial drug treatment. (**C**) Sub-clustering of the GC cluster identifies preMem, LZ, LZ/DZ, DZp and DZd B cells. (**D**) Line graphs of GC B cell subset frequencies over time, with or without drug treatment. (**E**) Violin plot of the median *Aicda* expression shown over time, with or without anti-malarial treatment in DZd and DZp GC B cells. (**F**) Scatter plot of somatic hypermutation rates of naïve (N) and GC (G) B cell BCRs and isotype usage between drug or non-drug-treated mice over time. Median number of mutations for each treatment and timepoint indicated in white. (**G**) Line graph of interquartile range (IQR) of GC B cell mutations at each timepoint. (**H**) Line graph of median number of mutations in the *Ighv* region of the BCR for each condition in comparison to clonal data from lymph node GC B cells after influenza infection from Mathew et al. and de Carvalho et al. Data in B and D are shown as mean ± SD of n = 3 per group.

Figure 5

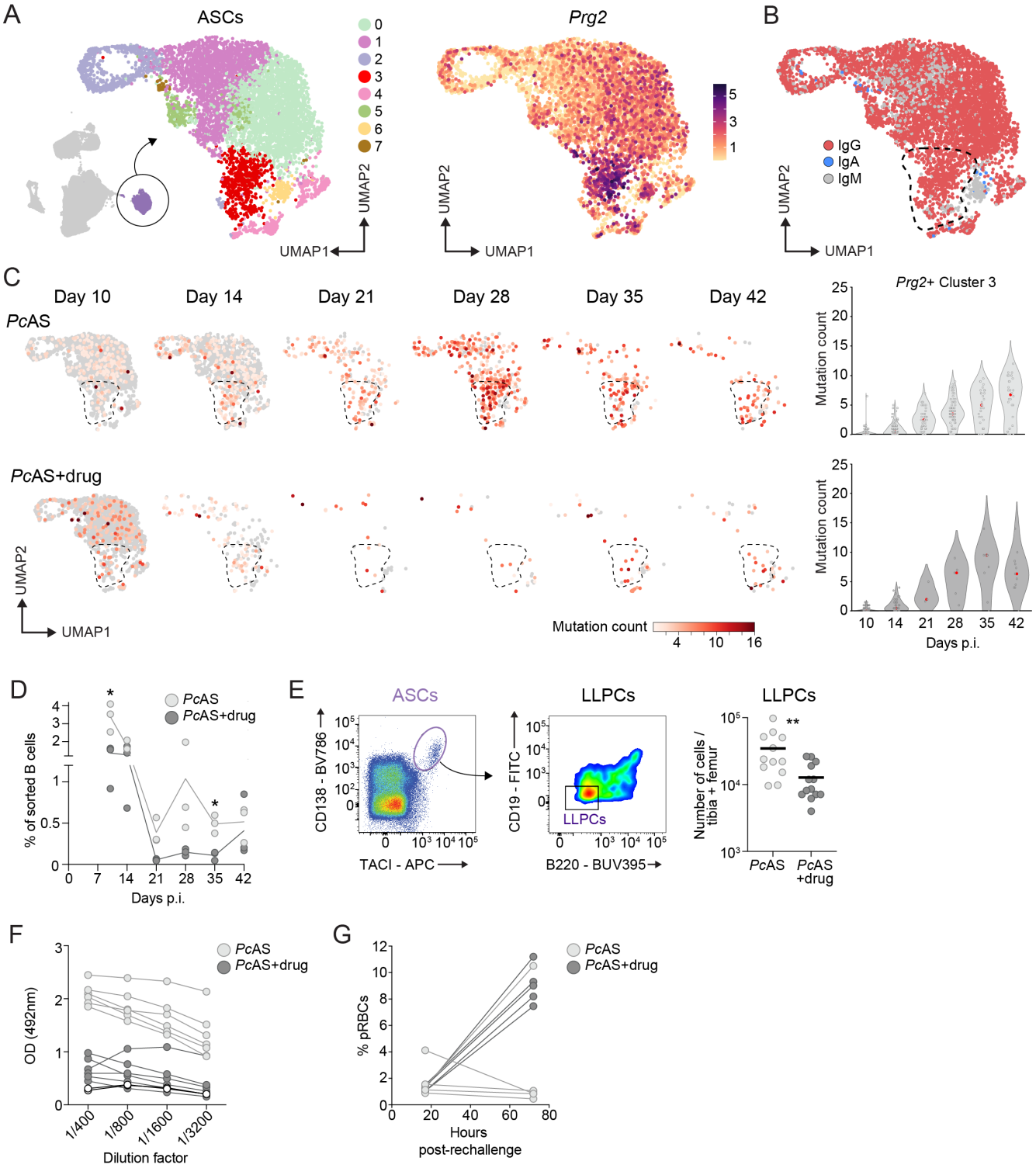
A
ASCs
0
1
2
3
4
5
6
7
UMAP2
UMAP1
Prg2
5
3
1
UMAP2
UMAP1
B
IgG
IgA
IgM
UMAP2
UMAP1
C
Day 10
Day 14
Day 21
Day 28
Day 35
Day 42
PcAS
PcAS+drug
UMAP2
UMAP1
Mutation count
4
10
16
Prg2+ Cluster 3
Mutation count
Days p.i.
D
PcAS
PcAS+drug
% of sorted B cells
Days p.i.
E
ASCs
CD138 - BV786
TACI - APC
LLPCs
CD19 - FITC
B220 - BUV395
LLPCs
Number of cells / tibia + femur
PcAS
PcAS +drug
F
PcAS
PcAS+drug
OD (492nm)
1/400
1/800
1/1600
1/3200
Dilution factor
G
PcAS
PcAS+drug
% pRBCs
Hours post-rechallenge

Figure 5: Anti-malarial treatment exerts quantitative limits on GC output.

(**A**) UMAP of sub-clustered antibody secreting cells (ASCs) identifies *Prg2*^{hi} splenic plasma cells (red). (**B**) UMAP of isotype classification with *Prg2*^{hi} cluster indicated. (**C**) UMAPs of BCR mutation counts in ASCs per timepoint, with or without anti-malarial drug treatment. *Prg2*^{hi} area indicated by enclosed dashed line and quantified in violin plots (right), where the median number of mutations from violin plots are highlighted in red (**D**) Line graph of *Prg2*^{hi} cell frequencies (cluster 3 plasma cells) over the course of infection with or without anti-malarial drug treatment. (**E**) Representative pseudocolour density plots of ASCs and long-lived plasma cells (LLPCs) from day 42 *Pc*AS-infected bone marrow with scatter plot (right) of total LLPCs per tibia and femur. (**F**) Line graph of *Plasmodium*-specific IgG levels in the sera of mice at 60 dpi with or without anti-malarials as measured via ELISA (uninfected mice, white dots). (**G**) Mice treated with or without anti-malarials during a primary *Pc*AS infection were rechallenged and parasitemia in the blood measured 17 and 72 hours post-rechallenge. Lines in panel D connects the mean values at each timepoint and compared using Welch's *t*-test. Data in panel E analysed by Mann-Whitney *t*-tests of n = 12-13 per group. Data are pooled from two independent experiments. Data in panel E represented by the mean. *$P < 0.05$, **$P < 0.01$.

Figure 6

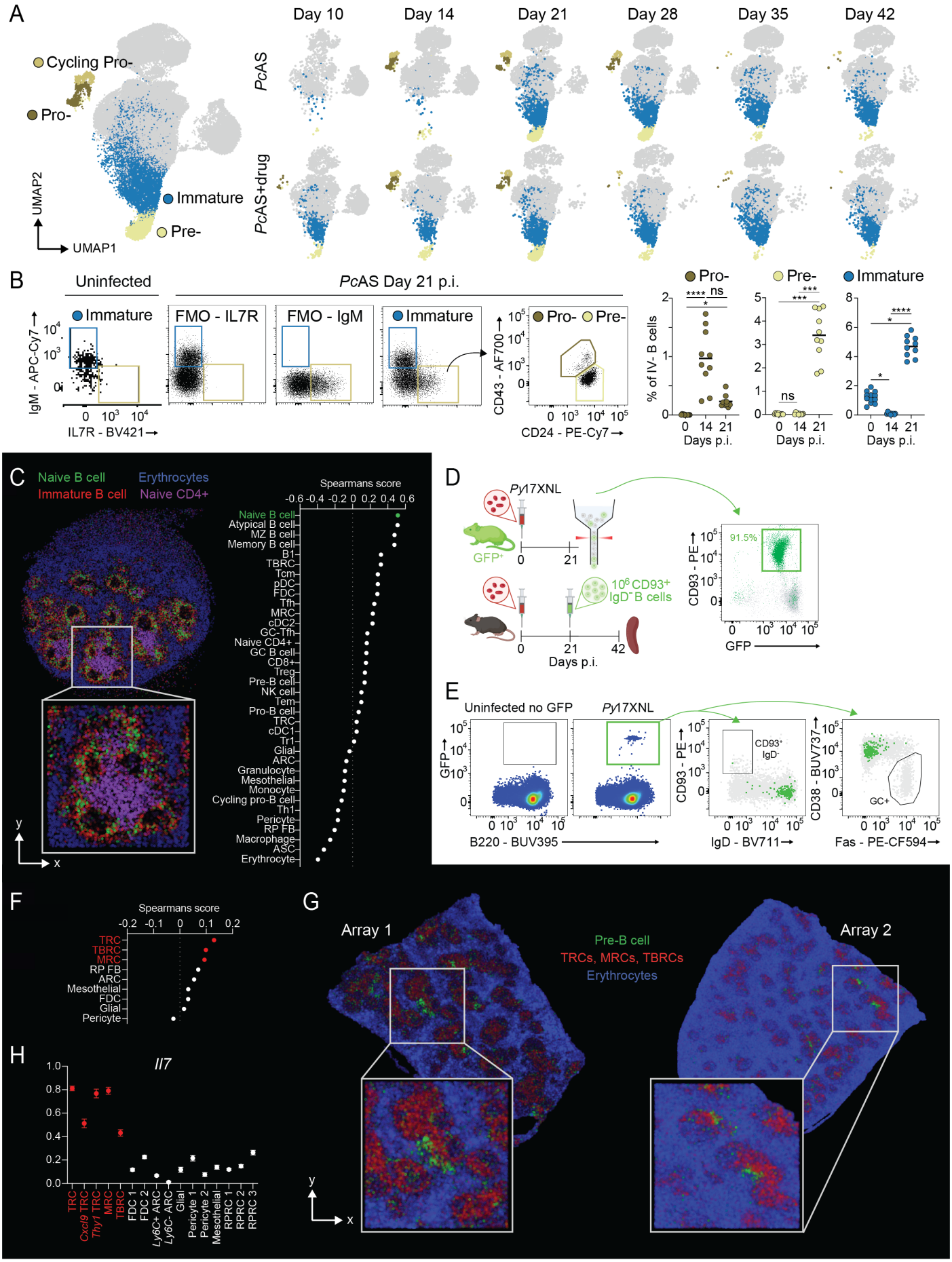
A
Day 10
Day 14
Day 21
Day 28
Day 35
Day 42
Cycling Pro-
Pro-
Immature
Pre-
UMAP2
UMAP1
PcAS
PcAS+drug
B
Uninfected
PcAS Day 21 p.i.
Immature
FMO - IL7R
FMO - IgM
Immature
Pro- Pre-
IgM - APC-Cy7
IL7R - BV421
CD43 - AF700
CD24 - PE-Cy7
Pro-
Pre-
Immature
% of IV- B cells
Days p.i.
C
Naive B cell
Immature B cell
Erythrocytes
Naive CD4+
Spearmans score
Naive B cell
Atypical B cell
MZ B cell
Memory B cell
B1
TBRC
Tcm
pDC
FDC
Tfh
MRC
cDC2
GC-Tfh
Naive CD4+
GC B cell
CD8+
Treg
Pre-B cell
NK cell
Tem
Pro-B cell
TRC
cDC1
Tr1
Glial
ARC
Granulocyte
Mesothelial
Monocyte
Cycling pro-B cell
Th1
Pericyte
RP FB
Macrophage
ASC
Erythrocyte
D
Py17XNL
GFP+
10^6 CD93+ IgD- B cells
Days p.i.
91.5%
CD93 - PE
GFP
E
Uninfected no GFP
Py17XNL
GFP
B220 - BUV395
CD93+ IgD-
CD93 - PE
IgD - BV711
GC+
CD38 - BUV737
Fas - PE-CF594
F
Spearmans score
TRC
TBRC
MRC
RP FB
ARC
Mesothelial
FDC
Glial
Pericyte
G
Array 1
Array 2
Pre-B cell
TRCs, MRCs, TBRCs
Erythrocytes
H
Il7
TRC
Cxcl9 TRC
Thy1 TRC
MRC
TBRC
FDC 1
FDC 2
Ly6C+ ARC
Ly6C- ARC
Glial
Pericyte 1
Pericyte 2
Mesothelial
RPRC 1
RPRC 2
RPRC 3

Figure 6: B cell lymphopoiesis relocates to the spleen during experimental malaria.

(**A**) Annotated B cell scVI-integrated (Experiment 1 & 2) UMAP highlighting specific precursor B cell subsets (pro-, cycling pro-, pre- and immature B cells) split over the course of infection, with or without anti-malarial drug treatment. (**B**) IL7R and IgM surface markers were used to identify precursor B cells shown by representative dot plots of B cells gated on CD45.2^{-} (intravenous label negative, IV^{-}), CD19^{+} B220^{+} CD138^{-} CD38^{+} Fas^{-} IgD^{-} CD93^{+} for immature B cells (IgM^{+} IL7R^{-}), pro-B cells (IgM^{-} IL7R^{+}, CD43^{hi} CD24^{int}) and pre-B cells (IgM^{-} IL7R^{+}, CD43^{int} CD24^{hi}) in uninfected mice and at day 21 post-*Pc*AS infection, with quantitation of splenic precursor B cells at 0, 14 and 21 dpi. Gating determined by representative FMOs. (**C**) Robust Cell Type Deconvolution (RCTD) of immature B cell populations in a representative *Plasmodium* infected spleen at 30 dpi using *Slide-seqV*2, showing the spearman's correlation score of immature B cell co-localisations with cell types from a scRNAseq reference across four independent 30 dpi spleen sections. (**D**) Sorting strategy for adoptive transfer of GFP^{+} splenic precursor B cells into *Py*17XNL infected host mice, showing enrichment of CD93^{+} GFP^{+} precursor B cells (right). (**E**) Representative pseudocolour density plots identifying GFP^{+} cells at day 21 post-transfer (green), compared to host-derived cells (grey). (**F**) RCTD spatial deconvolution of pre-B cell populations at 21 dpi using *Stereo-seqV1.2* spatial transcriptomics indicates spearman's correlation scores of pre-B cell co-localisations with various splenic stromal cell types from a scRNAseq reference. Highlighted in red, T cell zone reticular cells (TRCs), T-B reticular cells (TBRCs) and marginal reticular cells (MRCs). (**G**) Location of pre-B cells, white-pulp stromal cells and erythrocytes on both replicate arrays following RCTD spatial deconvolution. (**H**) *Il7* gene expression across multiple splenic stromal cell types from a publicly available dataset[50]. Data in panel B represented by the mean and analysed by Kruskal-Wallis test with Dunn's multiple comparisons test of n = 10-20 per group. Data in B are pooled from 2 independent experiments. *$P < 0.05$, ***$P < 0.001$, ****$P < 0.0001$. ns, not significant.

Figure 7

A

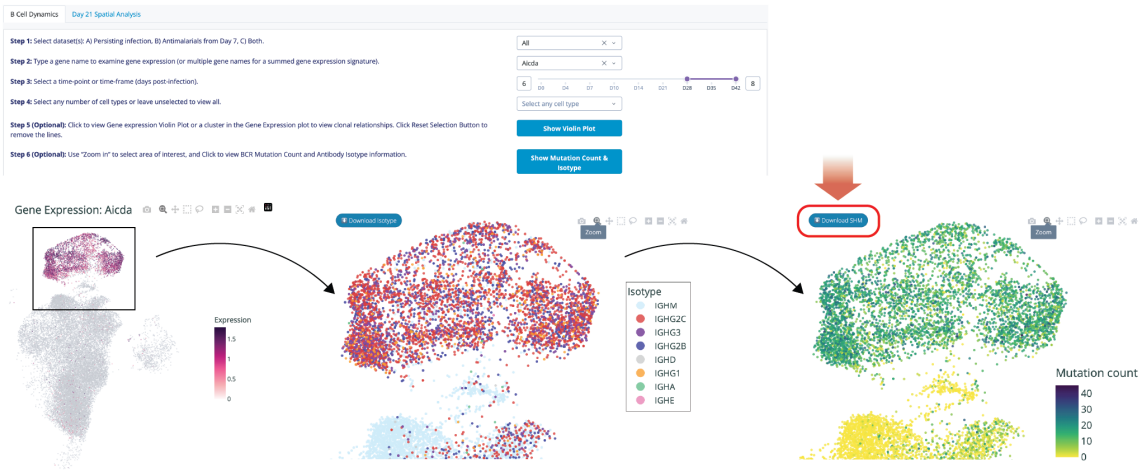

Clone_id	Isotype	Mutations	Days p.i.	Condition	CDR3_aa_VDJ	CDR3_aa_VJ
B_388_5_5_313_2_17IB_	IGHG2C	45	D35	PcAS+drug	AMDGSGSAF	QQSKEVPWTIQQWSSYSFT
B_227_1_1_266_2_12	IGHG2C	43	D42	PcAS+drug	TRGYDYDGNYGLDF	LHYDEFPWT
B_88_4_2_98_3_47	IGHA	38	D35	PcAS+drug	ARGYGSFDV	LQYDEFPYT
B_184_11_16_383_3_10	IGHG2C	38	D42	PcAS	ATRKLVSTRGDFAMDY	QQYSTYPFT
B_70_14_3_297_2_19	IGHG2C	37	D42	PcAS	VRSIFLYYFGSGYWYFDV	LQYAEFPLT
B_58_6_18_98_3_28	IGHG2B	36	D42	PcAS	TCYSIDWSTY	LQFDEFPYT
B_154_5_4_98_3_47	IGHG3	36	D42	PcAS+drug	AIWFFYALDS	LQYDEFPYT
B_11_9_4_139_3_72IB_1	IGHG2C	35	D35	PcAS+drug	ISREGWLQRGFTY	ALWYSNHWVIQQYHSYPYT
B_259_7_42_230_3_55	IGHG2B	35	D42	PcAS	ARKGWGAWFAY	QQCHIYPNT
B_237_9_12_248_3_26	IGHG2C	34	D42	PcAS+drug	TRFGTSYFAWFAY	QQYSNYPLT
B_173_5_32_135_3_25IB	IGHG2B	34	D42	PcAS	ARDHSFDY	QQFTSSPLTIHQWSTYPPT
B_339_8_29_339_2_4IB_	IGHG3	33	D35	PcAS+drug	ARSGDYDHGLDY	QQYHSYPLTIQQFSGYPLT
B_166_8_9_169_2_17	IGHG2C	33	D42	PcAS	ARDDYYGFWFVN	QHHYHPPYT
B_320_10_55_66_2_10	IGHG2C	32	D42	PcAS	ARVYYGGFYVGAMDY	HQYYSFPWT
B_327_7_24_72_3_22IB_	IGHG2B	32	D35	PcAS	ARRSYDDGRPYFDY	LQGTYYPYTIWQGSHFPRT
B_245_5_10_297_2_27	IGHG1	32	D28	PcAS+drug	AIYCDNWFFDV	LQYDEFPLT
B_327_7_24_72_3_22IB_	IGHG2B	32	D35	PcAS	ARRSYDDGRPYFDY	LQGTYYPYTIWQGSHFPRT
B_184_5_14_135_3_24	IGHG2C	32	D35	PcAS	ARLTNSVMDF	QQWRSSPTT
B_252_6_8_129_1_6IB_2	IGHG3	32	D35	PcAS	ARPNYSGSNTWFAY	HHYRSYPLTILQHLEYPYT
B_374_3_1_230_3_40	IGHG2C	32	D35	PcAS+drug	ARRGMDY	QQFNSYPYT

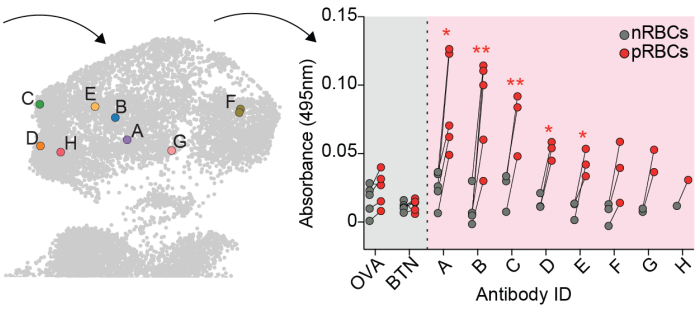

B

C

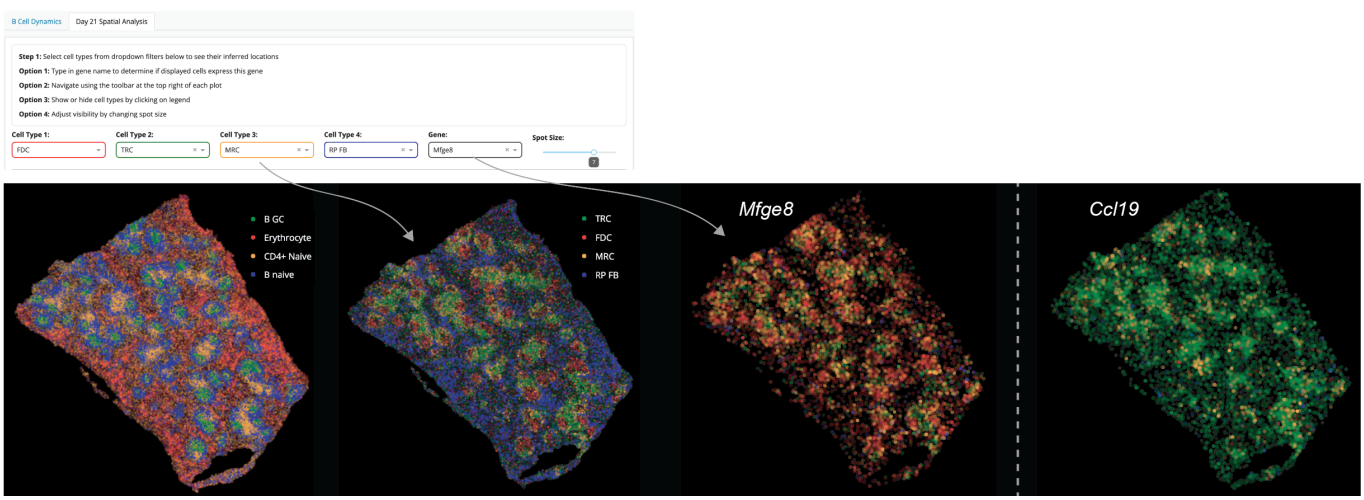

Figure 7: A Graphical User Interface (GUI) enables multi-parameter assessment of B cells *in vivo.*

(**A**) Case study 1 – GC B cells screened for *Aicda* expression at 28-42 dpi and assessed for isotypes and mutation counts. Selected GC BCR data downloaded and sorted by mutation count. Coloured are BCRs that were cloned from the GC B cell dataset. ELISA measuring binding of cloned antibodies and irrelevant antibodies (OVA - ovalbumin and BTN - butyrophilin) to lysates from naive and parasitised RBCs. Data is shown as the mean ± S.D., n = 1-5 per antibody, dependent on antibody yield (A – 1.5mg, B – 1.5mg, C – 1mg, D – 0.8mg, E – 1mg, F – 0.09mg, G – 0.22mg, H – 0.18mg), analysed by multiple paired t-tests. *P <0.05, **P <0.01. (**B**) Case study 2 – ASCs screened for *Prg2*$^{+}$ and *Ssr2*$^{-}$ expression in 21-42 dpi and assessed for isotypes and mutation counts. Clicking on the ASC cluster highlights individual expanded clones. (**C**) Case study 3 – location of GC B cells, erythrocytes, naïve CD4^{+} T cells and naïve B cells assessed on *Stereo-seqV1.2* spatial transcriptomic datasets from day 21 *Pc*AS infected mouse spleens. Location of TRCs, FDCs, MRCs and red pulp fibroblasts (RP FBs), followed by assessment of these cell types expressing *Mfge8* or *Ccl19*.

Extended Data Figures

Extended Data Figure 1

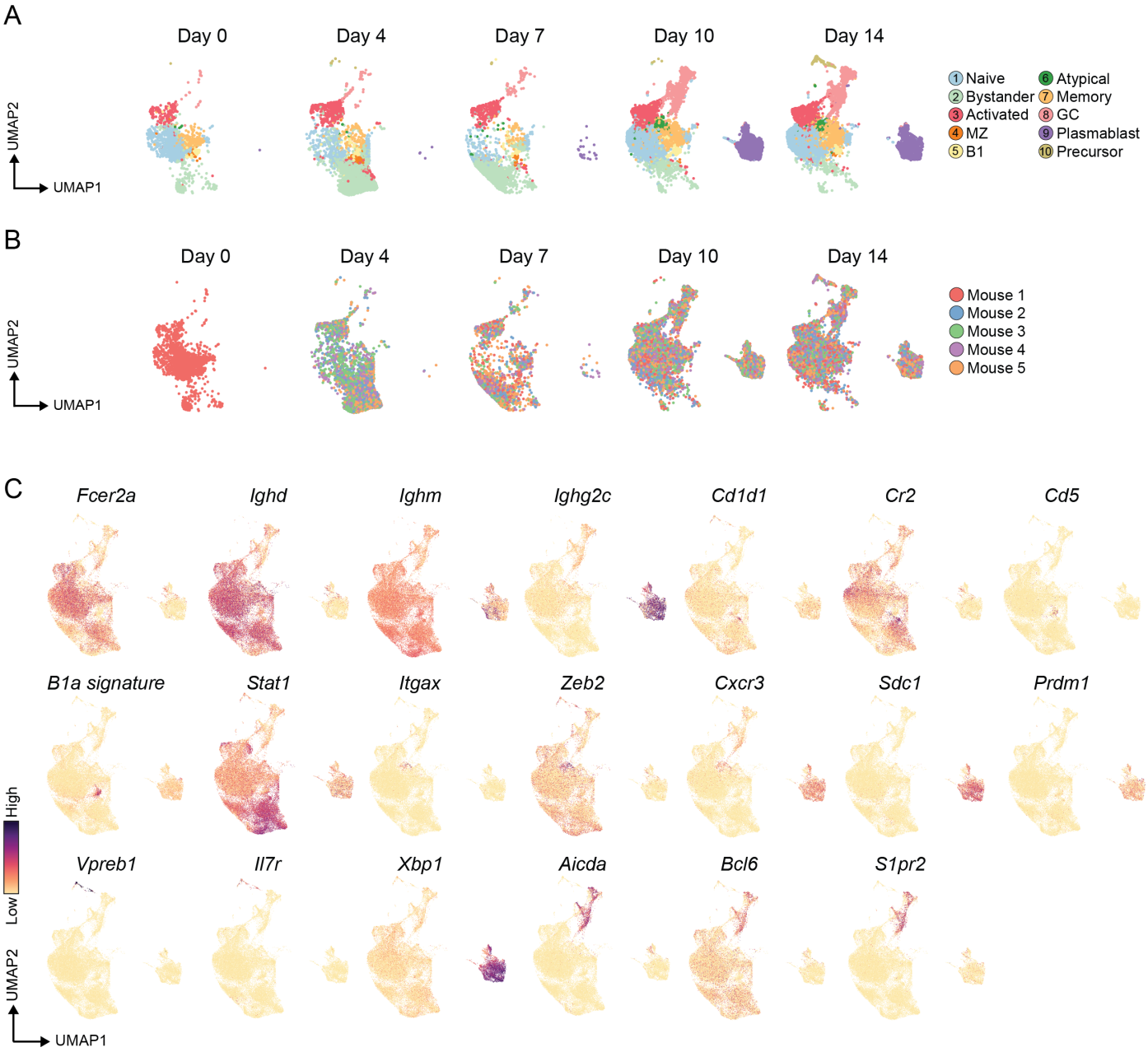

Extended Data Figure 1: Cluster annotation of B cell scRNAseq data (Experiment 1: 0-14 dpi).

(**A**) Annotation of B cell subsets after high-dimensional reduction and clustering analysis, split by timepoints and (**B**) grouped by individual mice. (**C**) Expression of canonical markers for each cluster type: naive follicular B cells (*Fcer2a*, unswitched: *Ighd*$^{+}$*, Ighm*$^{+}$*, Ighg2c*$^{-}$), MZ cells (*Cd1d1, Cr2*), B1 cells (*Cd5, B1a signature*), bystanders (*Stat1*), precursor B cells (*Vpreb1, Il7r*), atypicals (*Itgax, Zeb2, Cxcr3*), plasmablasts (*Sdc1, Prdm1, Xbp1*, switched: *Ighd*$^{-}$*, Ighg2c*$^{+}$) and GC B cells (*Aicda, Bcl6, S1pr2,* switched: *Ighd*$^{-}$*, Ighg2c*$^{+}$).

Extended Data Figure 2

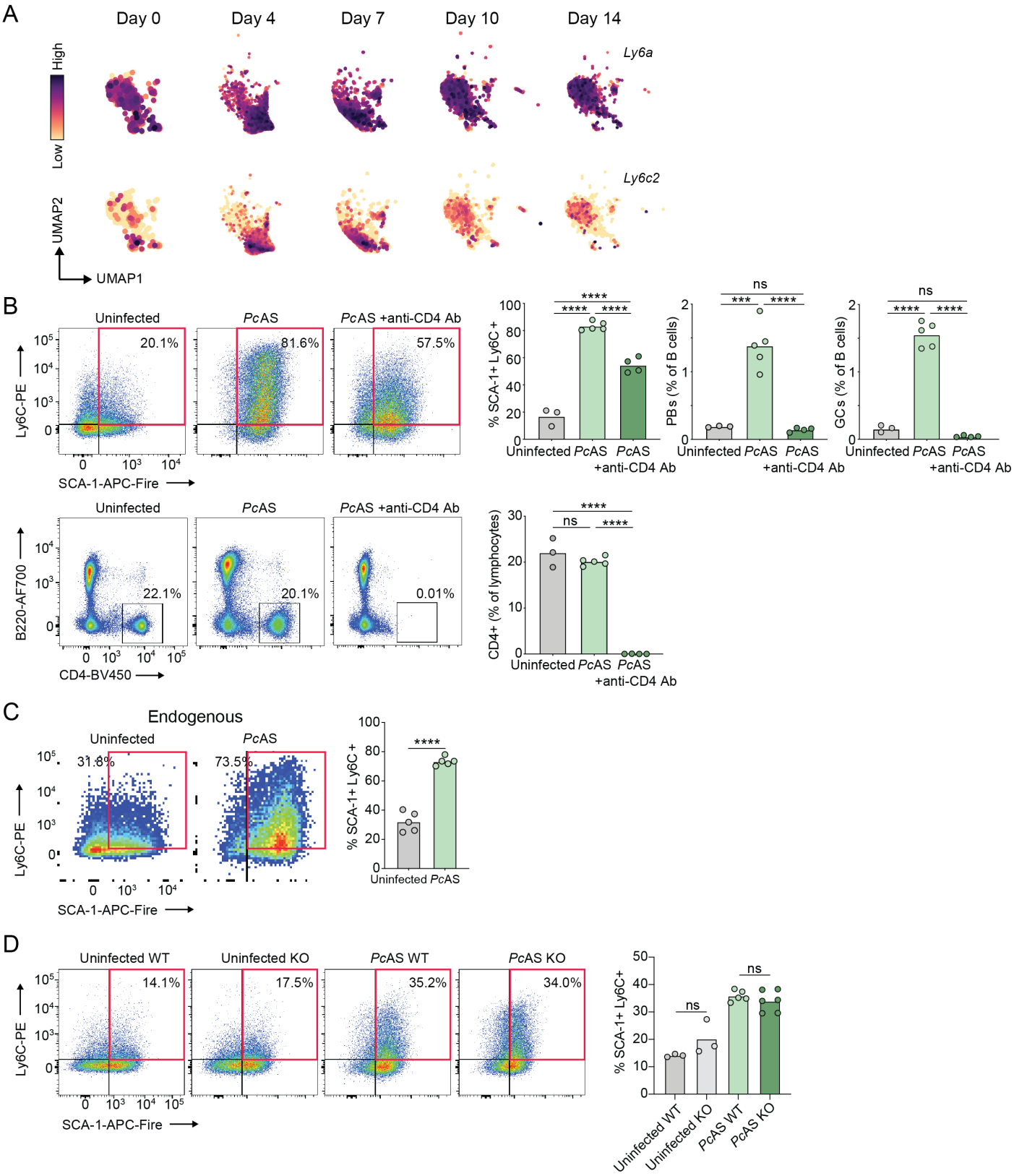

Extended Data Figure 2: Bystander B cell activation is partially CD4^{+} T cell-dependent, and independent of cell-intrinsic MyD88-signalling.

(**A**) Expression of *Ly6a* (Sca-1) and *Ly6c2* on naive follicular and bystander B cells over the course of *Plasmodium* infection. (**B**) Representative density dot plots and bar graphs of CD4 expression on lymphocytes 7 days post-*Pc*AS infection, and SCA-1 and Ly6C expression on IgD^{+} B cells, and frequency of plasmablast and GC B cells relative to all B cells 7 days post *Pc*AS infection, with or without CD4 T cell depletion. (**C**) Representative density dot plots and bar graph showing proportion of SCA-1 and Ly6C expression on CD86^{lo}, IgD^{+} endogenous host derived B cells from the OB1 adoptive transfer experiments, 4 days post-*Pc*AS infection. (**D**) Representative density dot plots, and bar graph showing proportion of SCA-1 and Ly6C expression on IgD^{+} MyD88flox/flox B cells with (CD23$^{cre+/-}$ KO) or without (CD23$^{cre-/-}$ WT) MyD88 KO, 7 days post-*Pc*AS infection. Data in panels B-D are represented as the mean value. Data in panel B and D analysed using one-way ANOVA with Tukey's multiple comparisons test and data in panel C analysed using Welch's *t*-test. All data are represented of two independent experiments of (B & C) n = 3-5 and (D) n = 3-7 biological replicates per group. ***P < 0.001, ****P < 0.0001. ns, not significant.

Extended Data Figure 3

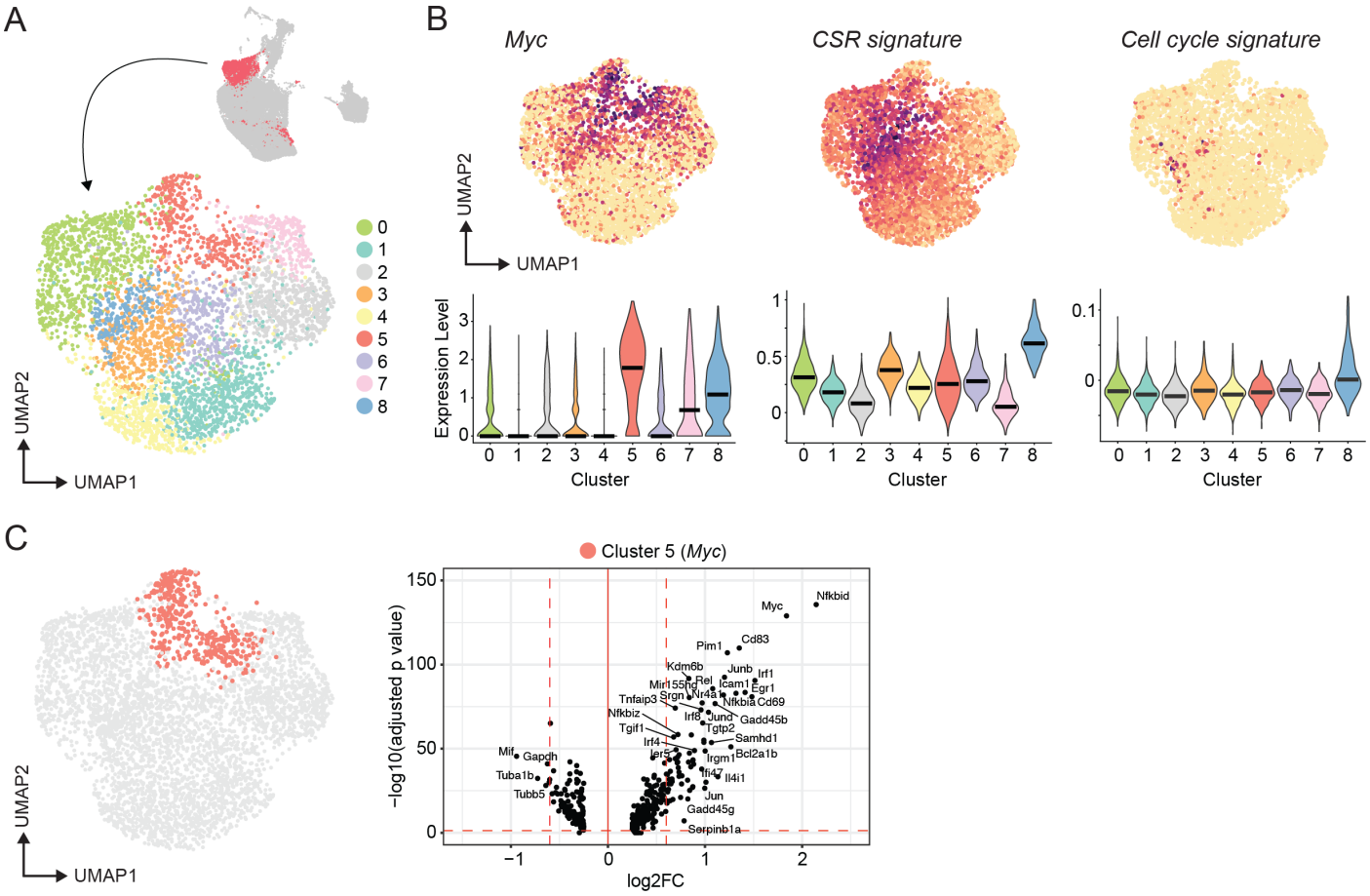

Extended Date Figure 3: Re-clustering and deeper analysis of the early activated B cell cluster.

(**A**) UMAP of sub-clustered activated B cells. (**B**) Expression of overlapping events of *Myc*, CSR and cell cycle signatures within each cluster. (**C**) Volcano plot of differentially regulated genes for Cluster 5 highlighting selected top differentially regulated and significant genes.

Extended Data Figure 4

A

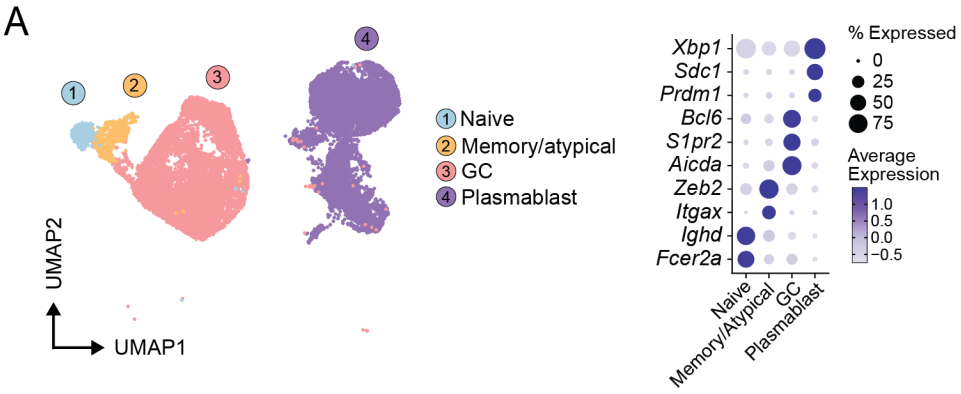

B

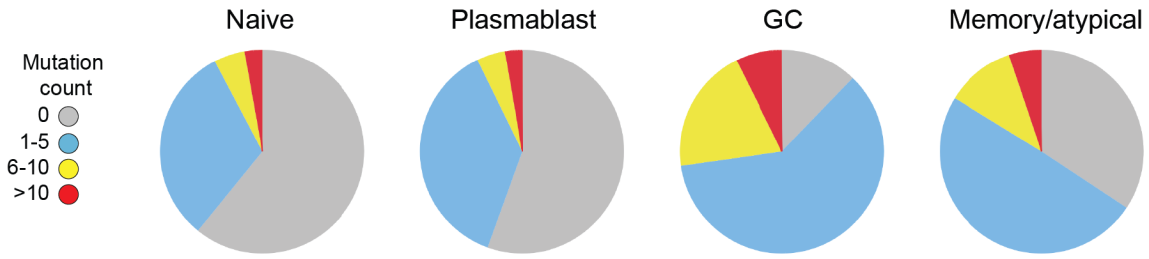

Extended Data Figure 4: QC assessment of scRNAseq/BCRseq data from enriched GC B cells and plasmablasts from a single representative mouse spleen at 14 dpi.

(**A**) Annotated UMAP of scRNAseq/BCRseq data generated from FACS-sorted splenic GC B cells, plasmablasts, minor populations of atypical/memory B cells, and naïve spike-in cells from a representative mouse at 14 dpi, with dot plot showing canonical gene markers. (**B**) Pie charts showing mutation count of clones detected in naïve B cells, GC B cells and memory/atypical B cells.

Extended Data Figure 5

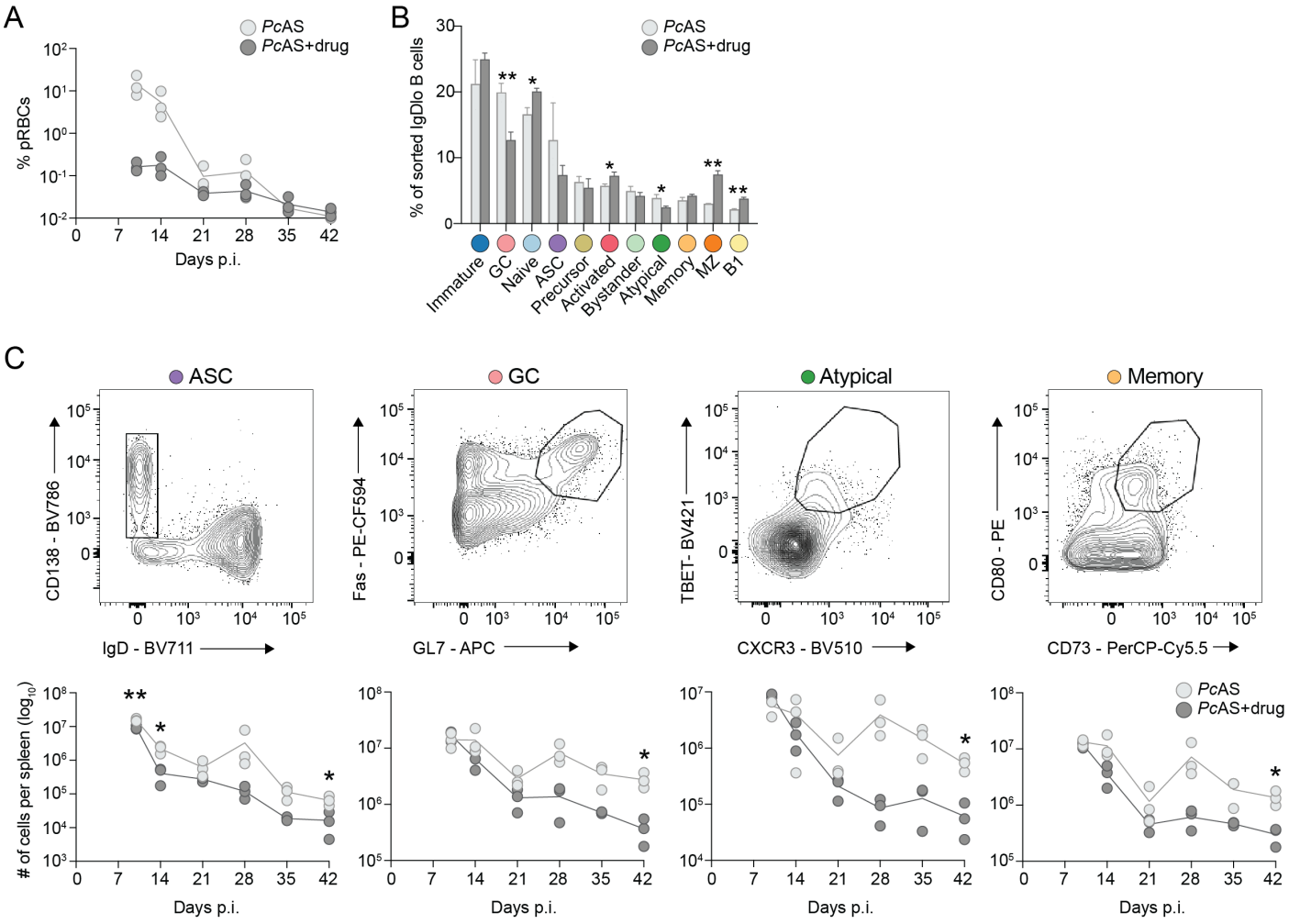

Extended Data Figure 5: Anti-malarial treatment efficacy, and effects on proportions of B cell subsets in scRNAseq and FACS validation datasets.

(**A**) Percentage parasitemia of circulating RBCs at each timepoint post with or without anti-malarials. Lines connect the mean values at each timepoint. (**B**) For the combined day 10-42 scRNAseq dataset, proportion of each B cell subset under each condition (*Pc*AS or *Pc*AS+drug) for individual mice. (**C**) Flow cytometric assessment of live $CD19^{+}$ $B220^{int\text{-}hi}$ cells for ASCs, GCs, atypical and memory B cells on matched spleen samples from the scRNAseq dataset at each timepoint post-infection, Data are the mean ± S.D, statistical test used was Welch's *t*-test. $^{*}P < 0.05$, $^{**}P < 0.01$.

Extended Data Figure 6

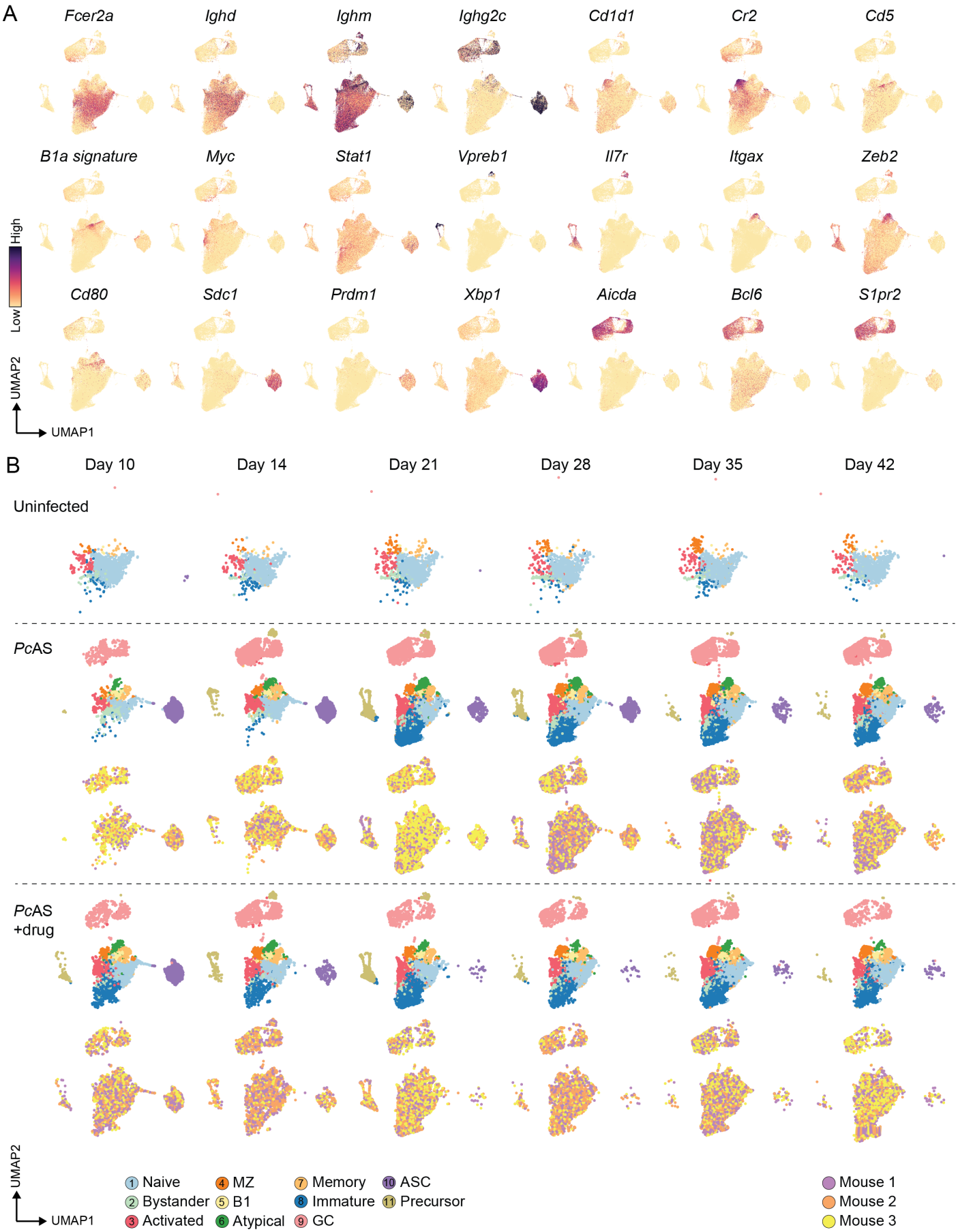

Extended Data Figure 6: Cluster annotation of B cell scRNAseq data (Experiment 2: 10-42 dpi).

(**A**) Expression of canonical markers for each cluster type: naive follicular B cells (*Fcer2a*, unswitched: *Ighd*$^{+}$*, Ighm*$^{+}$*, Ighg2c*$^{-}$), MZ cells (*Cd1d1, Cr2*), B1 cells (*Cd5, B1a signature*), activated B cells (*Myc*), bystanders (*Stat1*), precursor B cells (*Vpreb1, Il7r*), atypicals (*Itgax, Zeb2*), memory B cells (*Cd80*), plasmablasts (*Sdc1, Prdm1, Xbp1*, switched: *Ighd*$^{-}$*, Ighg2c*$^{+}$) and GC B cells (*Aicda, Bcl6, S1pr2,* switched: *Ighd*$^{-}$*, Ighg2c*$^{+}$). (**B**) Annotated UMAPs split by timepoint for each condition: uninfected, *Pc*AS or *Pc*AS+drug also grouped by individual mice.

Extended Data Figure 7

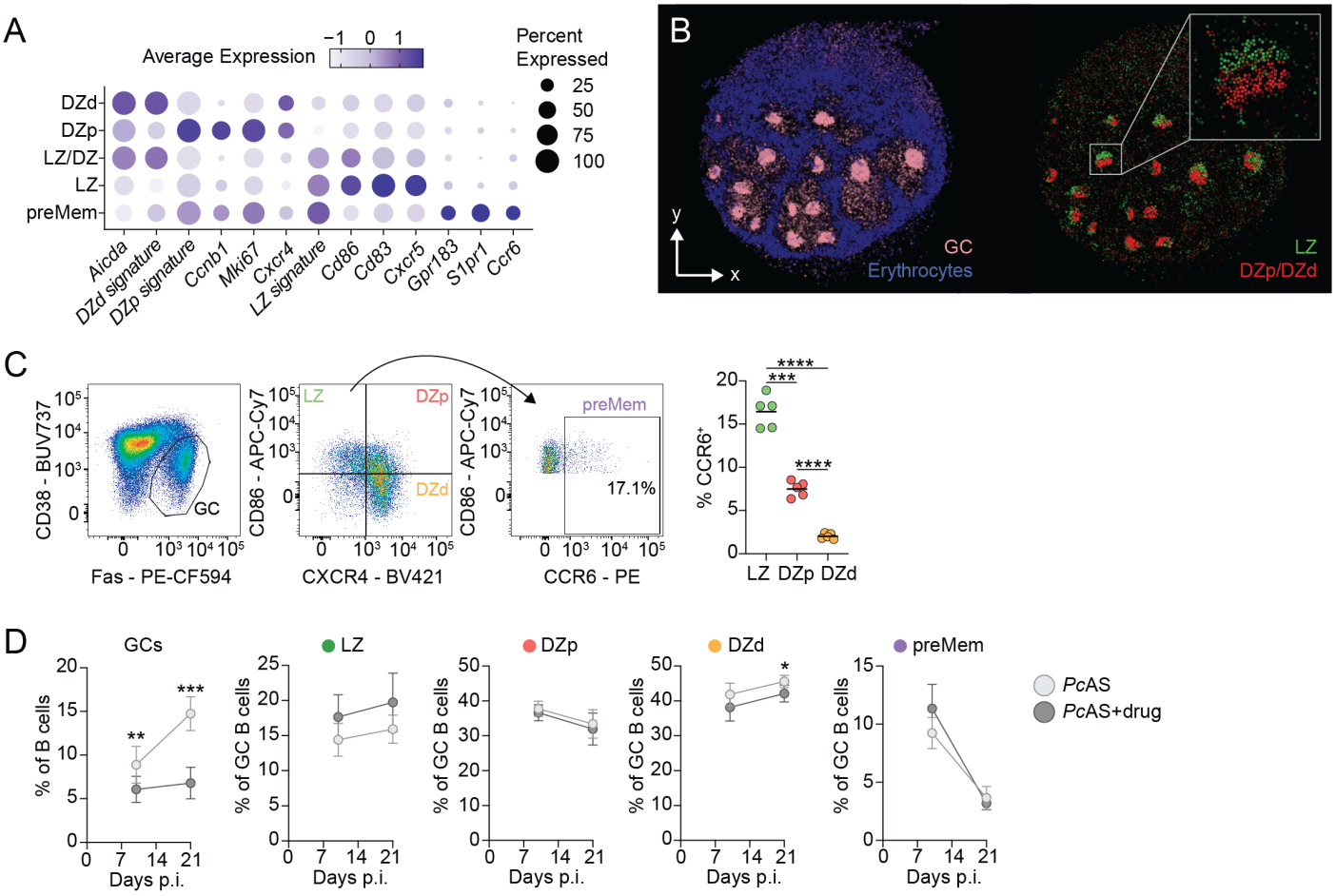

Extended Data Figure 7: Anti-malaria drug intervention does not affect GC B cell composition.

(**A**) Dot plot of canonical gene markers and signatures for LZ and DZ GC B cells and preMems. (**B**) RCTD spatial deconvolution of GC B cell populations on a day 30, *Plasmodium* infected spleen using *Slide-seqV2* spatial transcriptomics. (**C**) Gating strategy to identify $CD38^{-}$ Fas^{+} LZ, DZp, DZd and preMem GC B cells in 21 dpi mouse spleens, showing quantitation of % CCR6+ in each GC B cell compartment. Quantitation shown is representative of two independent experiments. Data is mean, n=5 biological replicates, analysed using paired one-way ANOVA with Geisser-Greenhouse correction. (**D**) Quantitation of splenic GC B cells and LZ, DZp, DZd and preMem GC B cells in 10 and 21 dpi mice with or without drug treatment. Data is shown as mean ± S.D. pooled form two independent experiments, n=9-10 biological replicates, and analysed using multiple Welch's t-tests. $^{*}P < 0.05$, $^{**}P < 0.01$. $^{****}P < 0.0001$.

Extended Data Figure 8

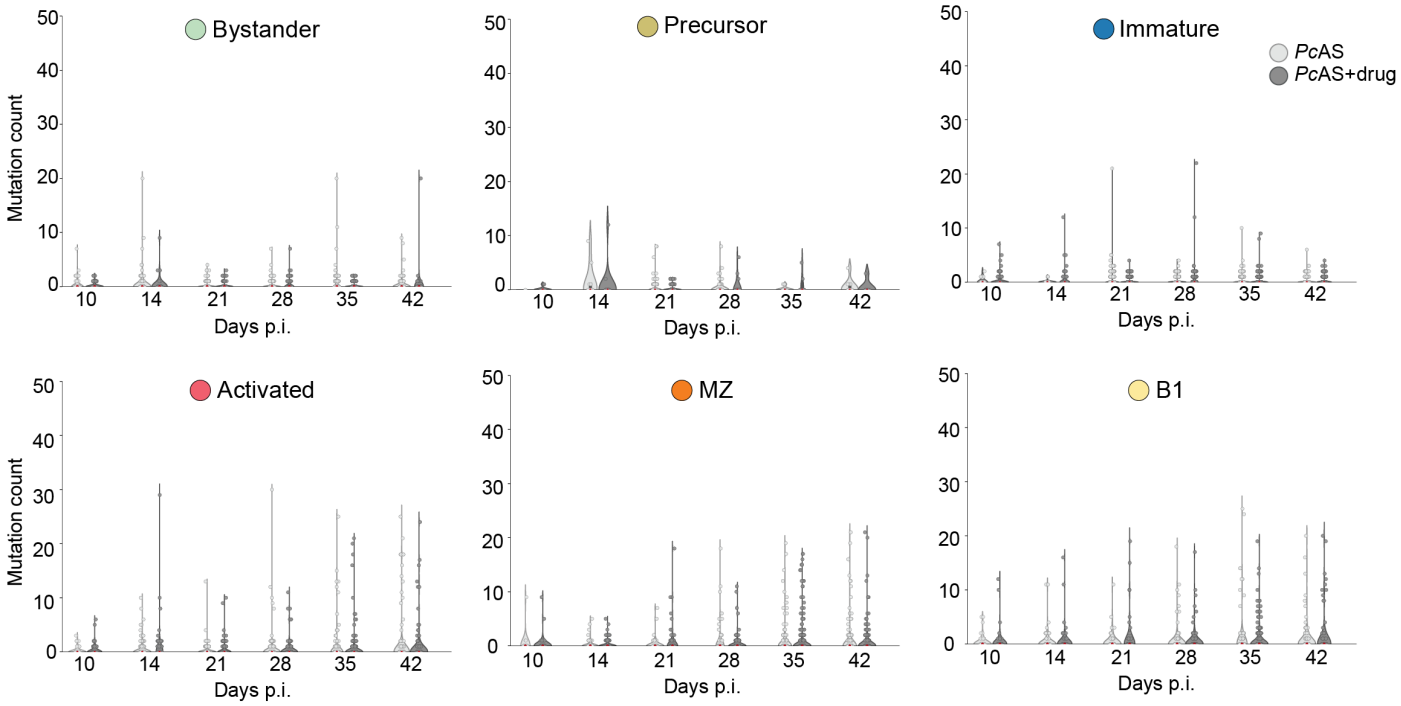

Extended Data Figure 8: Low BCR mutation counts across multiple B cell populations.

Somatic hypermutation analysis of various B cells (naive, precursor, immature, activated, MZ, B1 and bystander B cells) over the course of *Plasmodium* infection, split by treatment. Median number of mutations highlighted in red.

Extended Data Figure 9

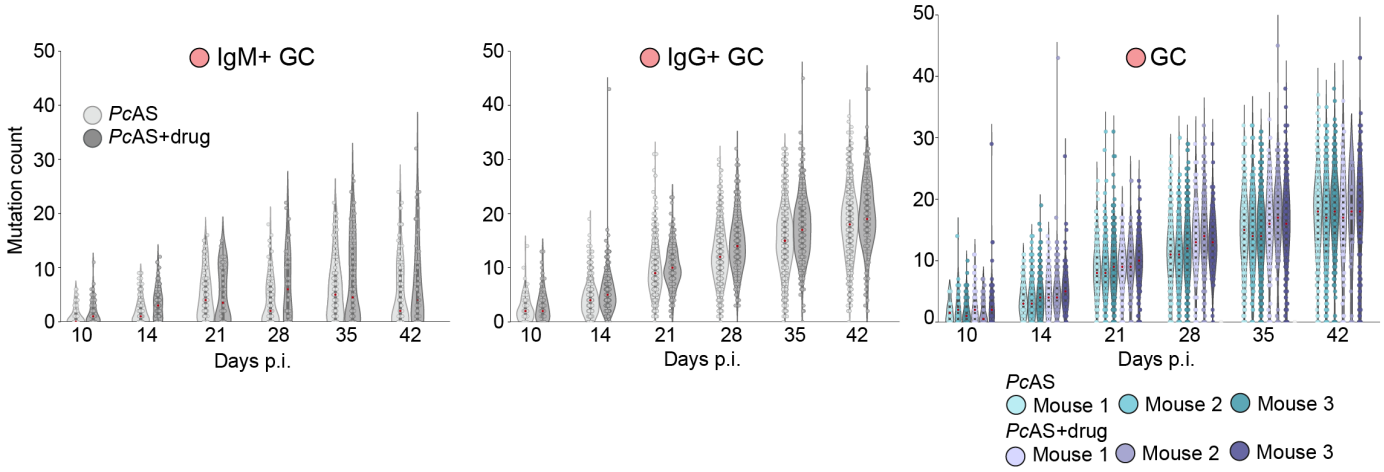

Extended Data Figure 9: BCR mutation counts in GC B cells over time, as depicted for different isotypes and across individual mice.

Somatic hypermutation analysis of GC B cells over the course of *Plasmodium* infection, split by treatment, shown as unswitched (IgM^+) and switched (IgG^+) and also shown mutations in all GC B cells split by individual mice. Median number of mutations highlighted in red.

Extended Data Figure 10

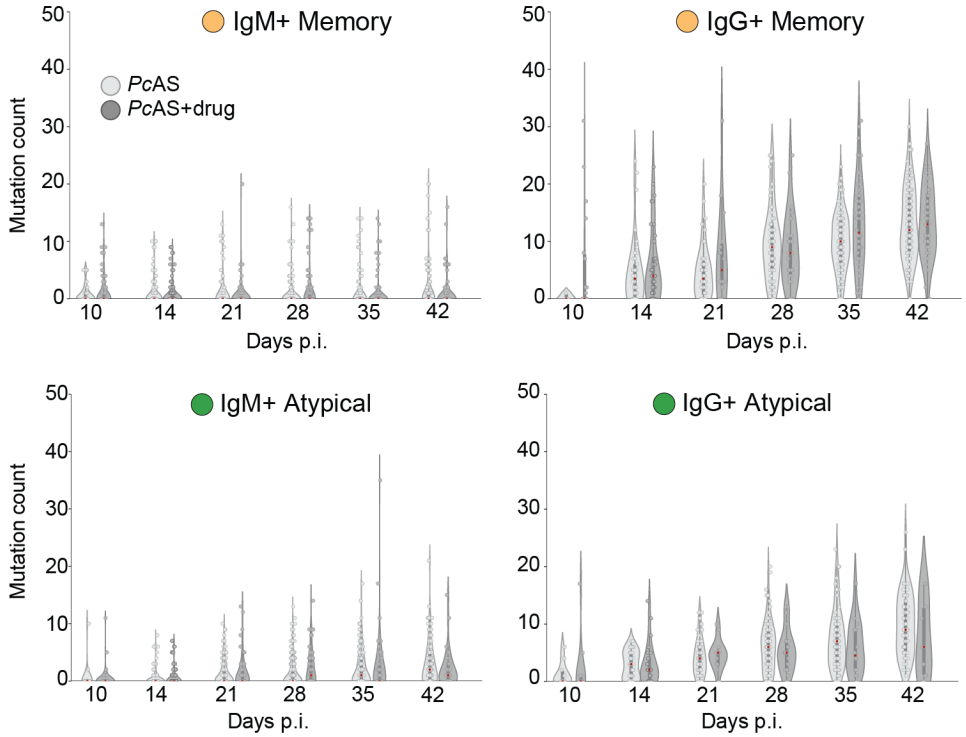

Extended Data Figure 10: BCR mutations over time for atypical and memory B cells.

Somatic hypermutation analysis of memory and atypical B cells split by unswitched (IgM^+) and switched (IgG^+) over the course of *Plasmodium* infection, split by treatment. Median number of mutations highlighted in red.

Extended Data Figure 11

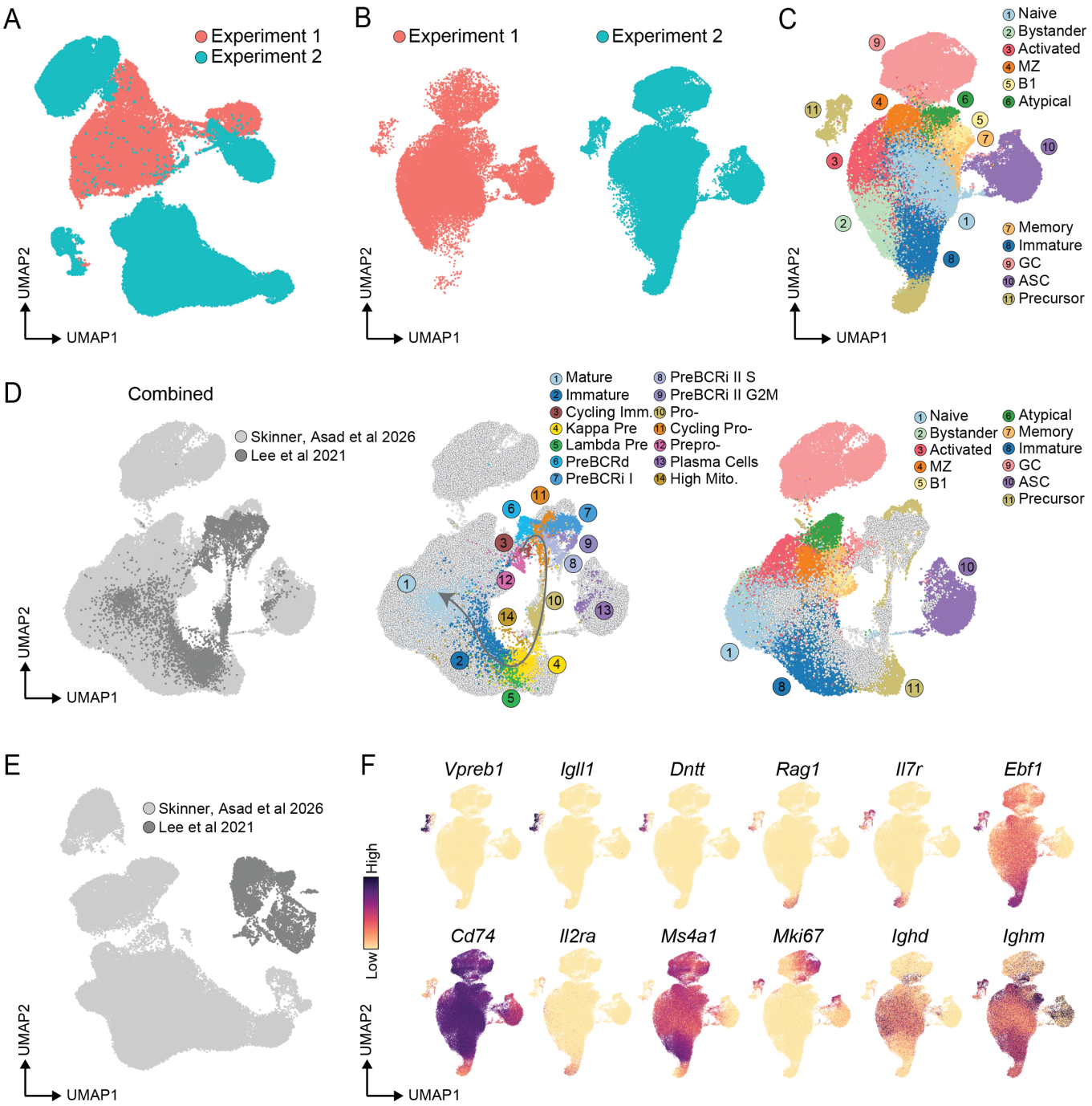

Extended Data Figure 11: Computational integration with bone marrow scRNAseq data facilitates identification of developing B cell subsets in the spleen.

(**A**) scVI integration of experiment 1 and 2 without batch correction. (**B**) Integrated scVI UMAP of experiment 1 and 2, using batch correction, split by experiment. (**C**) Annotated, scVI integrated UMAP of both experimental datasets. (**D**) scVI integration of our day 10-42 B cell dataset with publicly available scRNAseq bone marrow data combined and split by each dataset, with arrow indicating inferred trajectory of Lee et al., 2021 dataset. (**E**) scVI integration of our day 10-42 B cell dataset and publicly available bone marrow B cell scRNAseq dataset, without batch correction. (**F**) Expression of canonical markers of pro-B cells (*Vpreb1, Igll1, Dntt*), cycling pro-B cells (*Mki67*), pre-B cells (*Il2ra*), both pro- and pre-B cells (*Rag1, Il7r, Ebf1, Cd74*^{lo}*, Ighd*$^{-}$) and immature B cells (*Ms4a1, Ighd*$^{-}$*, Ighm*$^{+}$).

Extended Data Figure 12

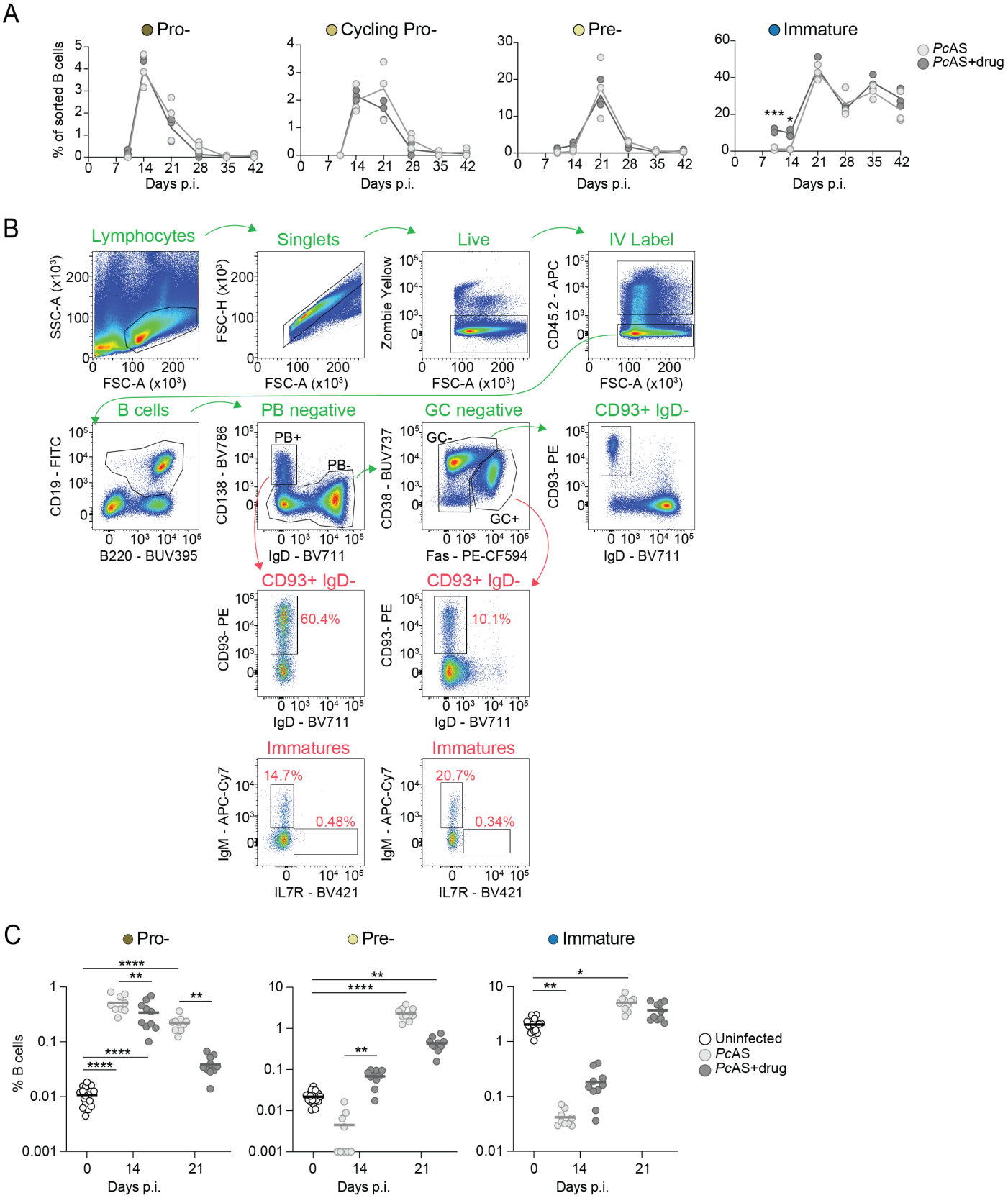

Extended Data Figure 12: Splenic B cell development during experimental malaria is unaffected by anti-malarial drug treatment.

(**A**) Quantification of pro-, cycling pro-, pre- and immature B cells in replicate mice from the integrated UMAP. (**B**) Gating strategy for identifying splenic precursor B cells after *Plasmodium* infection by gating on live CD45.2$^-$ CD19$^+$ B220$^+$ B cells, CD138$^-$ IgD$^+$ non-plasmablasts, CD38$^+$ Fas$^-$ non-GCs and IgD$^-$ CD93$^+$ to look for immature B cells (IgM$^+$ IL7R$^-$) and pre- and pro-B cells (IgM$^-$ IL7R$^+$). (**C**) Quantification of flow cytometric analysis of pro-, pre- and immature B cells at 14 and 21 dpi with or without anti-malarial drug treatment. Lines in panel A connect the mean values at each timepoint and analysed by Welch's *t*-test. Data in panel C is the mean of n=9-20 mice pooled form 2 independent experiments and analysed by one-way ANOVA with Tukey's multiple comparisons test (pro-B cells) or Kruskal-Wallis test with Dunn's multiple comparisons test (pre- and immature B cells). *P <0.05, **P <0.01, ***P <0.001, ****P <0.0001.

Extended Data Figure 13

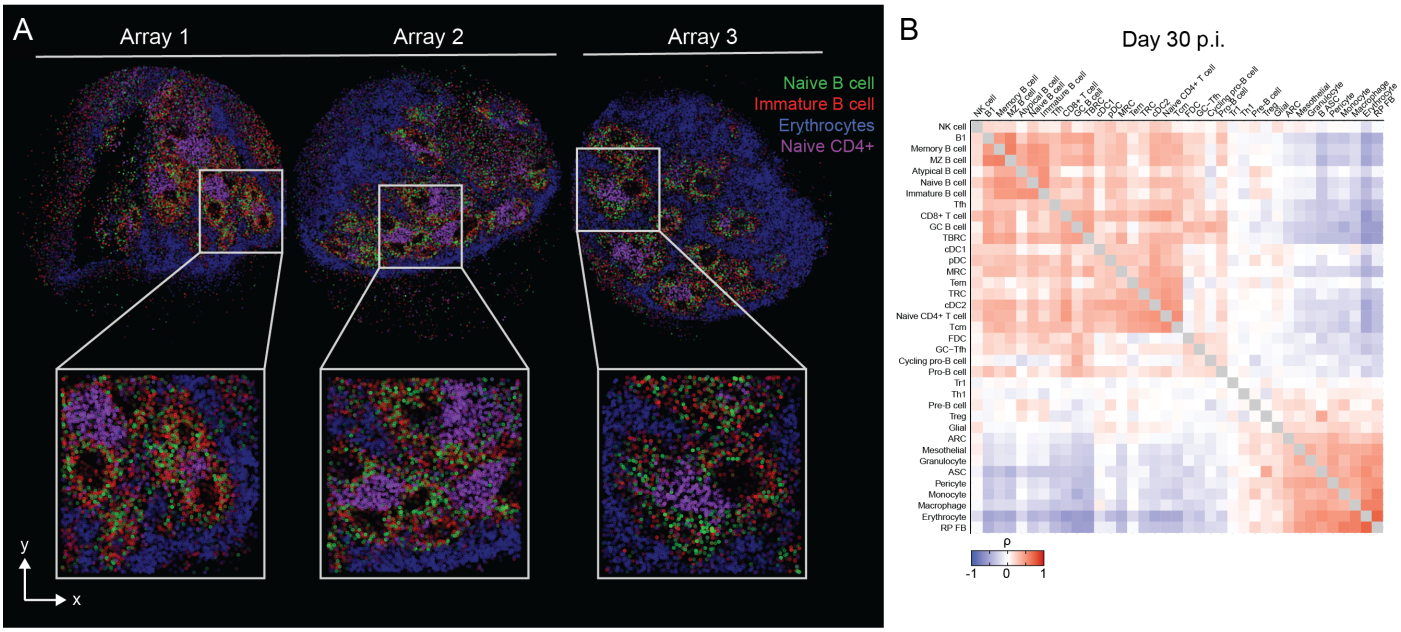

Extended Data Figure 13: Multiple spatial transcriptomic arrays at 30 dpi reveal co-localisation of immature B cells with naïve B cell follicles in the spleen.

(**A**) RCTD spatial deconvolution in 30 dpi spleens and three independent spleen sections. Arrays 1 and 2 are from the same mouse spleen. Array 3 is from same spleen as in Fig. 6C. (**B**) Spearman's correlation analysis of all cell co-localisations from all 4 arrays.

Extended Data Figure 14

A

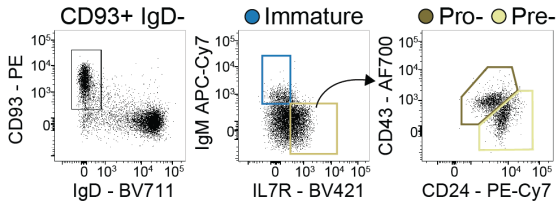

B

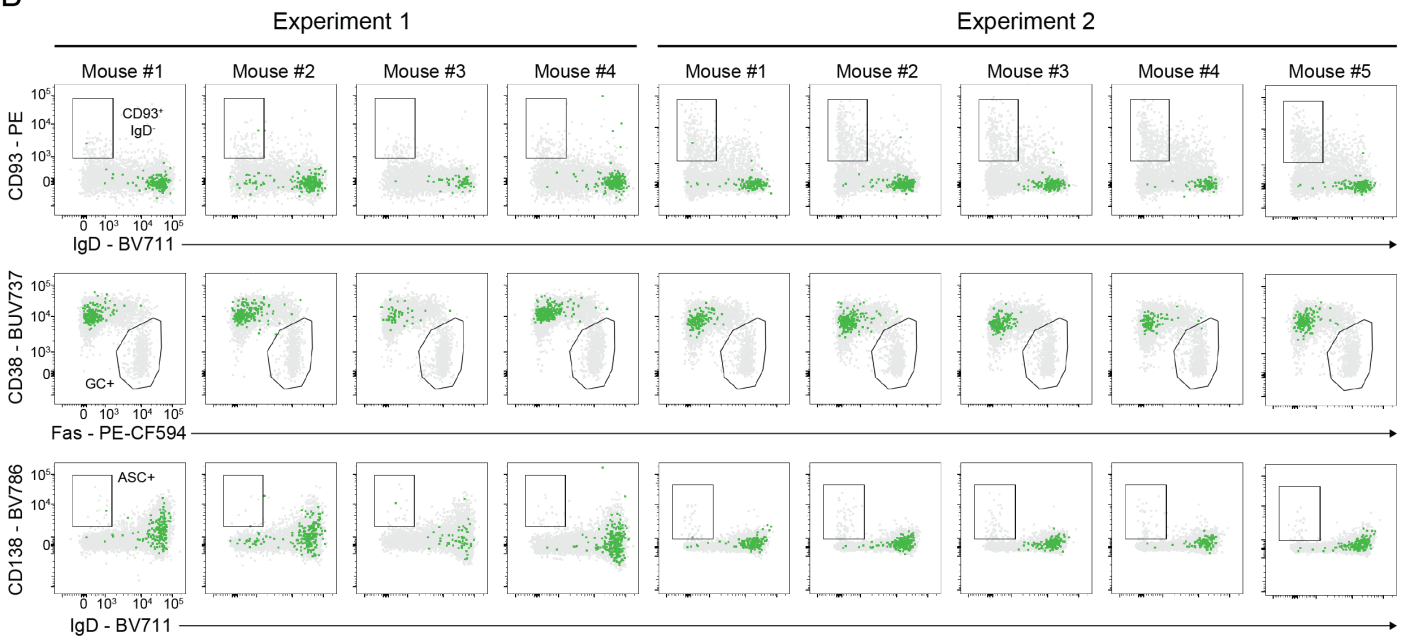

Extended Data Figure 14: QC and summary data illustrating splenic precursor B cells develop into mature B cells *in vivo*.

(**A**) Representative flow cytometry panel of splenocytes gated on $CD19^+$ $B220^+$ $CD138^-$ $CD38^+$ Fas^- for $CD93^+$ IgD^- B cells, followed by immature B cells (IgM^+ $IL7R^-$), pro-B cells (IgM^- $IL7R^+$, $CD43^{hi}$ $CD24^{int}$) and pre-B cells (IgM^- $IL7R^+$, $CD43^{int}$ $CD24^{hi}$) in mice at 21 dpi with *Py*17XNL. (**B**) Flow cytometry panels of $CD93^+$ IgD^- B cells, GC B cells and ASCs at 21 days post-transfer of GFP^+ $CD93^+$ IgD^- splenic precursor B cells (green cells). Cells in grey are endogenous cells from host mice at day 42 post *Py*17XNL infection.

Supplementary Method Figures

Supplementary Method Figure 1

A

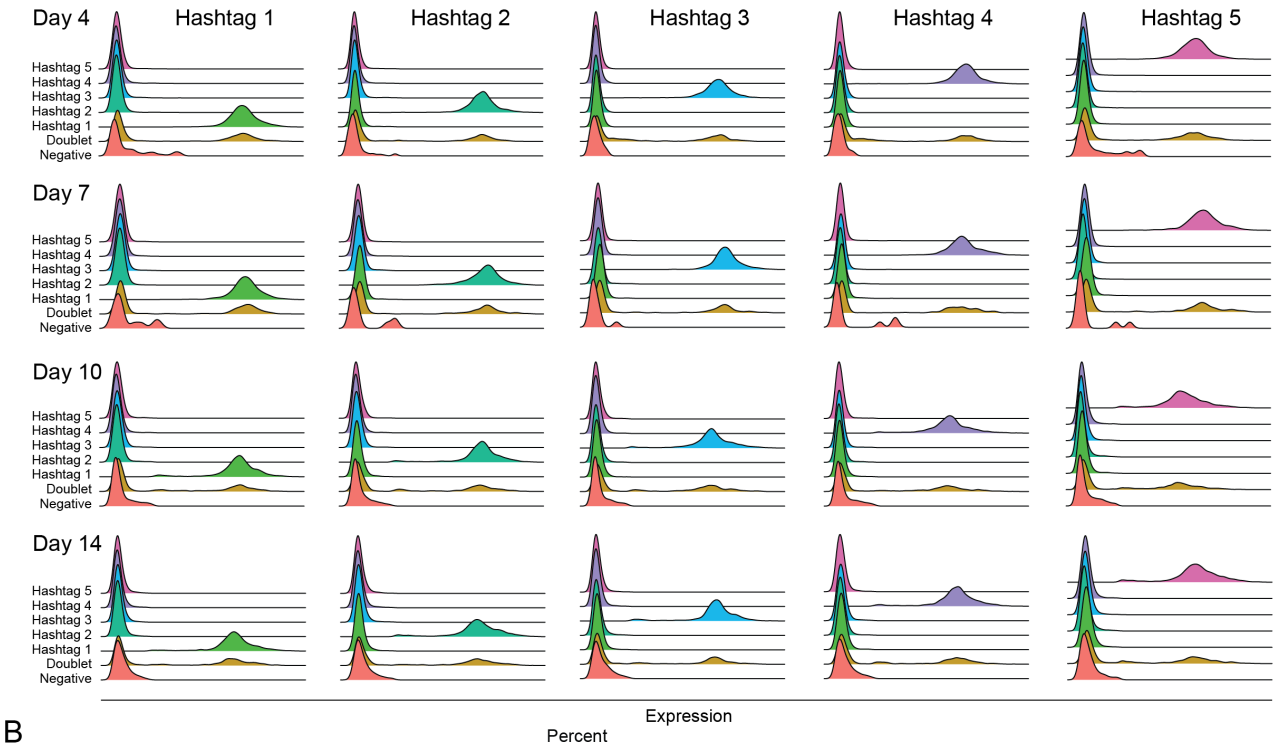

B

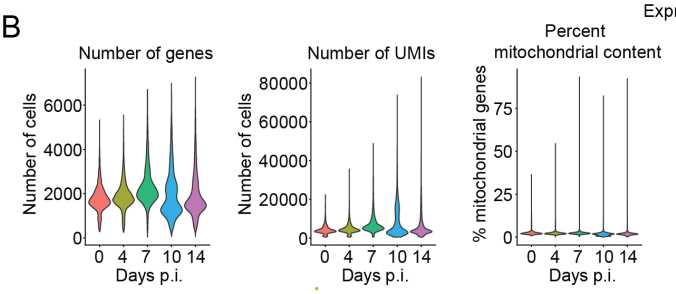

C

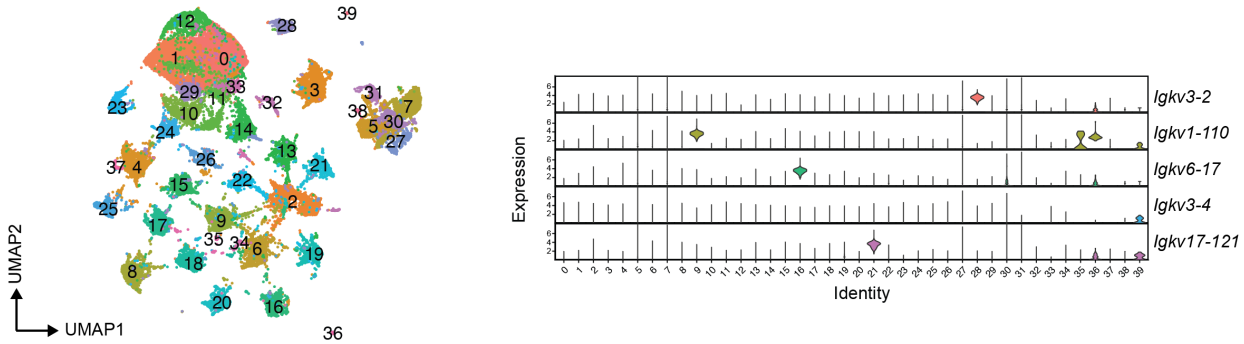

D

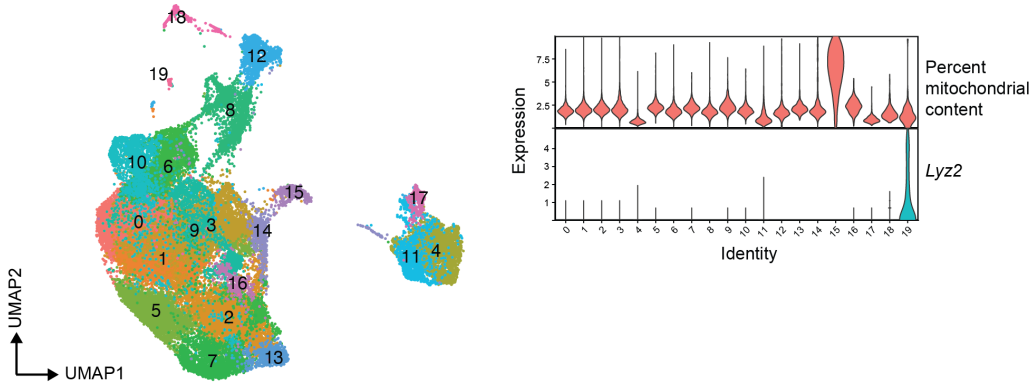

Supplementary Method Figure 1: Quality control for B cell scRNAseq Experiment 1: 0-14 dpi.

(**A**) Ridge plots for each hashtag showing expression of hashtag oligos for singlets (hashtags 1-5), doublets and negative cells for each timepoint. Note, hashtag 1 in the day 4 group is the day 0, naive B cell sample. (**B**) Violin plots of number of genes, number of UMIs and percent mitochondrial content prior to pre-processing of data. (**C**) UMAP of entire B cell dataset after high-dimensional reduction and clustering prior to removal of BCR-related genes including violin plots showing distribution of expression of a random selection of BCR related genes for each cluster. (**D**) UMAP of entire B cell dataset after removal of BCR-related genes and after high-dimensional reduction and clustering. Violin plots show the distribution of percent mitochondrial content and *Lyz2* (monocytes) expression per cluster.

Supplementary Method Figure 2

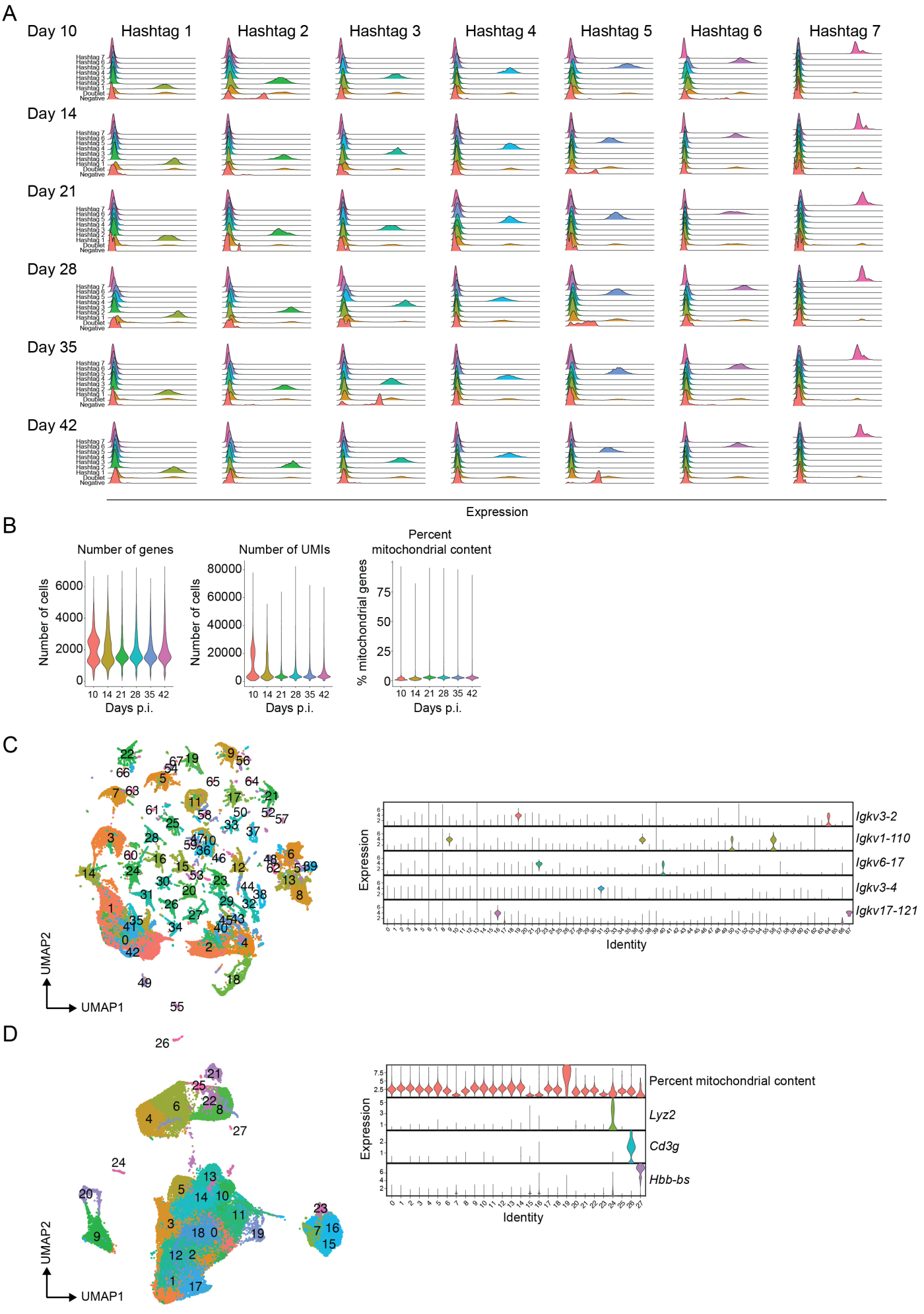

Supplementary Method Figure 2: Quality control for B cell scRNAseq Experiment 2: 10-42 dpi.

(**A**) Ridge plots for each hashtag showing expression of hashtag oligos for singlets (hashtags 1-7), doublets and negative cells for each timepoint. (**B**) Violin plots of number of genes, number of UMIs and percent mitochondrial content prior to pre-processing of data. (**C**) UMAP of entire B cell dataset after high-dimensional reduction and clustering prior to removal of BCR-related genes including violin plots showing distribution of expression of a random selection of BCR related genes for each cluster. (**D**) UMAP of entire B cell dataset after removal of BCR-related genes and after high-dimensional reduction and clustering. Violin plots show the distribution of percent mitochondrial content and *Lyz2* (monocytes), *Cd3g* (T cells) and *Hbb-bs* (erythrocytes) expression per cluster.

Supplementary Method Figure 3

A

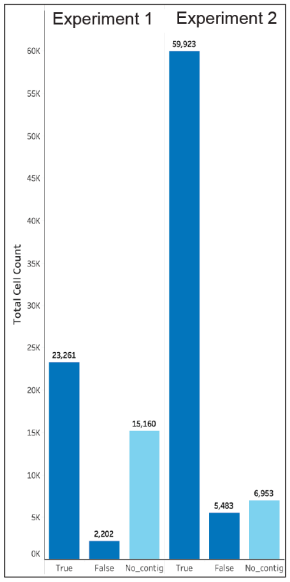

B

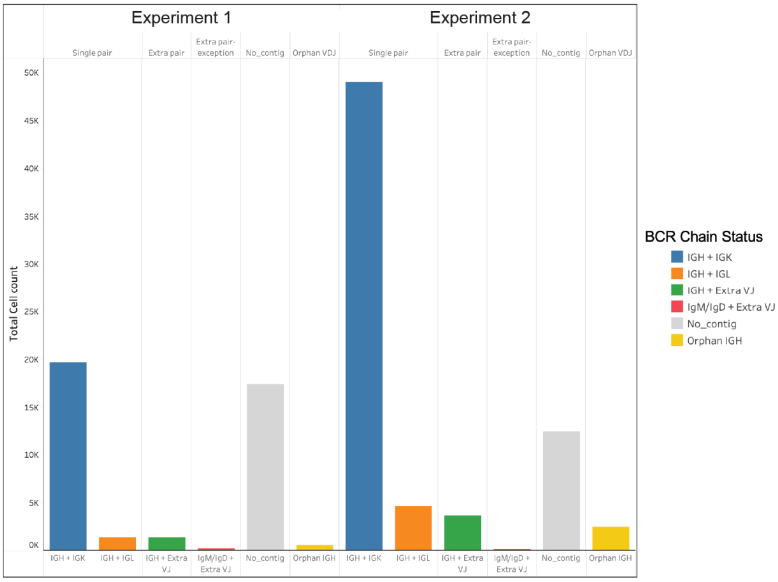

C

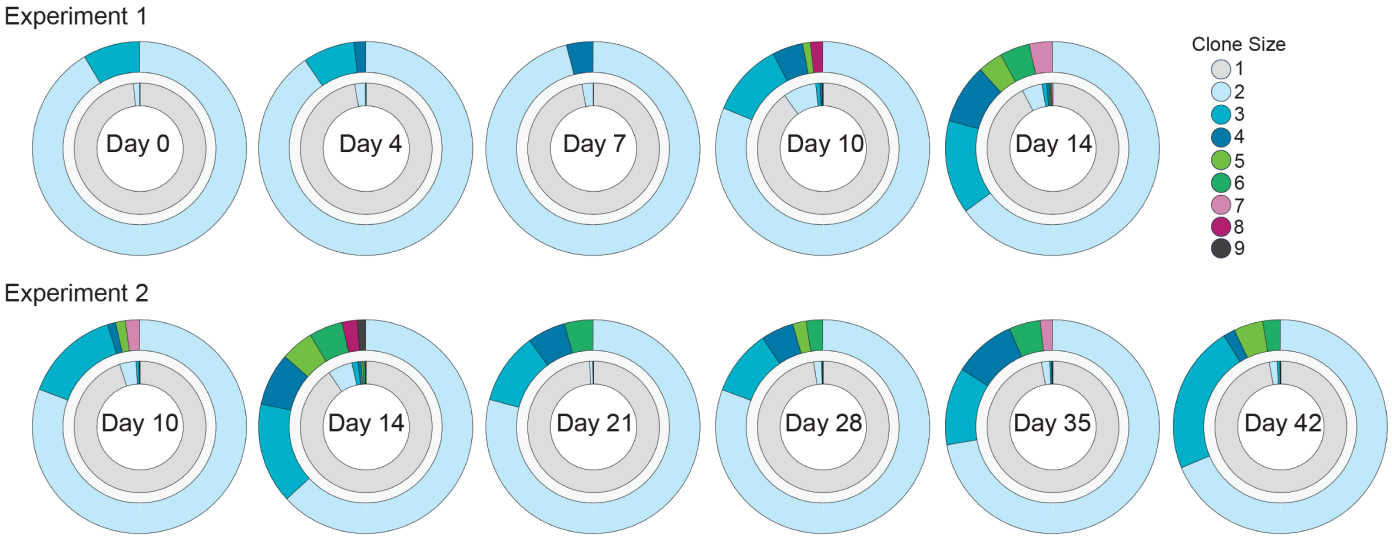

Supplementary Method Figure 3: Quality control for clonal analysis from single-cell BCRseq

(**A**) Bar graph showing distribution of cells which passed Dandelion quality control pipeline for each experiment. (**B**) Bar graph showing distribution of BCR chains in each experiment. (**C**) Donut plots showing all clones including unexpanded and expanded clones (inner donut) and expanded clones only (outer donut) at each timepoint for each experiment.

References

1 Stavnezer, J., Guikema, J. E. & Schrader, C. E. Mechanism and regulation of class switch recombination. *Annu Rev Immunol* **26**, 261–292 (2008). https://doi.org/10.1146/annurev.immunol.26.021607.090248

2 Stavnezer, J. & Schrader, C. E. IgH chain class switch recombination: mechanism and regulation. *J Immunol* **193**, 5370–5378 (2014). https://doi.org/10.4049/jimmunol.1401849

3 Mesin, L., Ersching, J. & Victora, G. D. Germinal Center B Cell Dynamics. *Immunity* **45**, 471–482 (2016). https://doi.org/10.1016/j.immuni.2016.09.001

4 Suan, D., Sundling, C. & Brink, R. Plasma cell and memory B cell differentiation from the germinal center. *Curr Opin Immunol* **45**, 97–102 (2017). https://doi.org/10.1016/j.coi.2017.03.006

5 Sutton, H. J. *et al.* Atypical B cells are part of an alternative lineage of B cells that participates in responses to vaccination and infection in humans. *Cell Rep* **34**, 108684 (2021). https://doi.org/10.1016/j.celrep.2020.108684

6 Holla, P. *et al.* Shared transcriptional profiles of atypical B cells suggest common drivers of expansion and function in malaria, HIV, and autoimmunity. *Sci Adv* **7** (2021). https://doi.org/10.1126/sciadv.abg8384

7 Eisen, H. N. & Siskind, G. W. Variations in Affinities of Antibodies during the Immune Response. *Biochemistry* **3**, 996–1008 (1964). https://doi.org/10.1021/bi00895a027

8 Vijay, R. *et al.* Infection-induced plasmablasts are a nutrient sink that impairs humoral immunity to malaria. *Nat Immunol* **21**, 790–801 (2020). https://doi.org/10.1038/s41590-020-0678-5

9 Osier, F. H. *et al.* Breadth and magnitude of antibody responses to multiple Plasmodium falciparum merozoite antigens are associated with protection from clinical malaria. *Infect Immun* **76**, 2240–2248 (2008). https://doi.org/10.1128/IAI.01585-07

10 Rono, J. *et al.* Breadth of anti-merozoite antibody responses is associated with the genetic diversity of asymptomatic Plasmodium falciparum infections and protection against clinical malaria. *Clin Infect Dis* **57**, 1409–1416 (2013). https://doi.org/10.1093/cid/cit556

11 Nkumama, I. N. *et al.* Breadth of Fc-mediated effector function correlates with clinical immunity following human malaria challenge. *Immunity* **57**, 1215–1224 e1216 (2024). https://doi.org/10.1016/j.immuni.2024.05.001

12 Bhatt, S. *et al.* The effect of malaria control on Plasmodium falciparum in Africa between 2000 and 2015. *Nature* **526**, 207–211 (2015). https://doi.org/10.1038/nature15535

13 Chandramohan, D. *et al.* Seasonal Malaria Vaccination with or without Seasonal Malaria Chemoprevention. *N Engl J Med* **385**, 1005–1017 (2021). https://doi.org/10.1056/NEJMoa2026330

14 Dicko, A. *et al.* Seasonal vaccination with RTS,S/AS01(E) vaccine with or without seasonal malaria chemoprevention in children up to the age of 5 years in Burkina Faso and Mali: a double-blind, randomised, controlled, phase 3 trial. *Lancet Infect Dis* (2023). https://doi.org/10.1016/S1473-3099(23)00368-7

15 Greenwood, B. M. *et al.* Mortality and morbidity from malaria after stopping malaria chemoprophylaxis. *Trans R Soc Trop Med Hyg* **89**, 629–633 (1995). https://doi.org/10.1016/0035-9203(95)90419-0

16 Menendez, C. *et al.* Randomised placebo-controlled trial of iron supplementation and malaria chemoprophylaxis for prevention of severe anaemia and malaria in Tanzanian infants. *Lancet* **350**, 844–850 (1997). https://doi.org/10.1016/S0140-6736(97)04229-3

17 Schreiber, N. *et al.* Immune responses after single-dose sulphadoxine-pyrimethamine indicate underestimation of protective efficacy of intermittent preventive treatment in infants. *Trop Med Int Health* **12**, 1157–1163 (2007). https://doi.org/10.1111/j.1365-3156.2007.01902.x

18 Boulanger, D. *et al.* Immunological consequences of intermittent preventive treatment against malaria in Senegalese preschool children. *Malar J* **9**, 363 (2010). https://doi.org/10.1186/1475-2875-9-363

19 Toellner, K. M., Gulbranson-Judge, A., Taylor, D. R., Sze, D. M. & MacLennan, I. C. Immunoglobulin switch transcript production in vivo related to the site and time of antigen-specific B cell activation. *J Exp Med* **183**, 2303–2312 (1996). https://doi.org/10.1084/jem.183.5.2303

20 Pape, K. A. *et al.* Visualization of the genesis and fate of isotype-switched B cells during a primary immune response. *J Exp Med* **197**, 1677–1687 (2003). https://doi.org/10.1084/jem.20012065

21 Roco, J. A. *et al.* Class-Switch Recombination Occurs Infrequently in Germinal Centers. *Immunity* **51**, 337–350 e337 (2019). https://doi.org/10.1016/j.immuni.2019.07.001

22 Taylor, J. J., Pape, K. A., Steach, H. R. & Jenkins, M. K. Humoral immunity. Apoptosis and antigen affinity limit effector cell differentiation of a single naive B cell. *Science* **347**, 784–787 (2015). https://doi.org/10.1126/science.aaa1342

23 Gitlin, A. D. *et al.* Independent Roles of Switching and Hypermutation in the Development and Persistence of B Lymphocyte Memory. *Immunity* **44**, 769–781 (2016). https://doi.org/10.1016/j.immuni.2016.01.011

24 Horton, M. B. *et al.* Lineage tracing reveals B cell antibody class switching is stochastic, cell-autonomous, and tuneable. *Immunity* **55**, 1843–1855 e1846 (2022). https://doi.org/10.1016/j.immuni.2022.08.004

25 de Carvalho, R. V. H. *et al.* Clonal replacement sustains long-lived germinal centers primed by respiratory viruses. *Cell* **186**, 131–146 e113 (2023). https://doi.org/10.1016/j.cell.2022.11.031

26 Hagglof, T. *et al.* Continuous germinal center invasion contributes to the diversity of the immune response. *Cell* **186**, 147–161 e115 (2023). https://doi.org/10.1016/j.cell.2022.11.032

27 King, H. W. *et al.* Single-cell analysis of human B cell maturation predicts how antibody class switching shapes selection dynamics. *Sci Immunol* **6** (2021). https://doi.org/10.1126/sciimmunol.abe6291

28 Espinoza, D. A. *et al.* Distinct stage-specific transcriptional states of B cells derived from human tonsillar tissue. *JCI Insight* **8** (2023). https://doi.org/10.1172/jci.insight.155199

29 Bushell, E. *et al.* Functional Profiling of a Plasmodium Genome Reveals an Abundance of Essential Genes. *Cell* **170**, 260–272 e268 (2017). https://doi.org/10.1016/j.cell.2017.06.030

30 Siddiqui, G. *et al.* A new mass spectral library for high-coverage and reproducible analysis of the Plasmodium falciparum-infected red blood cell proteome. *Gigascience* **11** (2022). https://doi.org/10.1093/gigascience/giac008

1052 31 Venkatesan, P. WHO world malaria report 2024. *Lancet Microbe*, 101073 (2025).
1053 https://doi.org/10.1016/j.lanmic.2025.101073
1054 32 Sebina, I. *et al.* IFNAR1-Signalling Obstructs ICOS-mediated Humoral Immunity during
1055 Non-lethal Blood-Stage Plasmodium Infection. *PLoS Pathog* **12**, e1005999 (2016).
1056 https://doi.org/10.1371/journal.ppat.1005999
1057 33 James, K. R. *et al.* IFN Regulatory Factor 3 Balances Th1 and T Follicular Helper
1058 Immunity during Nonlethal Blood-Stage Plasmodium Infection. *J Immunol* **200**, 1443–
1059 1456 (2018). https://doi.org/10.4049/jimmunol.1700782
1060 34 Habib, T. *et al.* Myc stimulates B lymphocyte differentiation and amplifies calcium
1061 signaling. *J Cell Biol* **179**, 717–731 (2007). https://doi.org/10.1083/jcb.200704173
1062 35 Prazma, C. M., Yazawa, N., Fujimoto, Y., Fujimoto, M. & Tedder, T. F. CD83 expression is a
1063 sensitive marker of activation required for B cell and CD4+ T cell longevity in vivo. *J*
1064 *Immunol* **179**, 4550–4562 (2007). https://doi.org/10.4049/jimmunol.179.7.4550
1065 36 Zhao, M. *et al.* NF-kappaB subunits direct kinetically distinct transcriptional cascades in
1066 antigen receptor-activated B cells. *Nat Immunol* **24**, 1552–1564 (2023).
1067 https://doi.org/10.1038/s41590-023-01561-7
1068 37 Lonnberg, T. *et al.* Single-cell RNA-seq and computational analysis using temporal
1069 mixture modelling resolves Th1/Tfh fate bifurcation in malaria. *Sci Immunol* **2** (2017).
1070 https://doi.org/10.1126/sciimmunol.aal2192
1071 38 Soon, M. S. F. *et al.* Transcriptome dynamics of CD4(+) T cells during malaria maps
1072 gradual transit from effector to memory. *Nat Immunol* **21**, 1597–1610 (2020).
1073 https://doi.org/10.1038/s41590-020-0800-8
1074 39 Lee, H. J. *et al.* CD4(+) T cells display a spectrum of recall dynamics during re-infection
1075 with malaria parasites. *Nat Commun* **15**, 5497 (2024). https://doi.org/10.1038/s41467-
1076 024-49879-6
1077 40 Yuan, D. Regulation of IgM and IgD synthesis in B lymphocytes. II. Translational and
1078 post-translational events. *J Immunol* **132**, 1566–1570 (1984).
1079 41 Sebina, I. *et al.* IL-6 promotes CD4(+) T-cell and B-cell activation during Plasmodium
1080 infection. *Parasite Immunol* **39** (2017). https://doi.org/10.1111/pim.12455
1081 42 Suo, C. *et al.* Dandelion uses the single-cell adaptive immune receptor repertoire to
1082 explore lymphocyte developmental origins. *Nat Biotechnol* (2023).
1083 https://doi.org/10.1038/s41587-023-01734-7
1084 43 Meng, W. *et al.* An atlas of B-cell clonal distribution in the human body. *Nat Biotechnol*
1085 **35**, 879–884 (2017). https://doi.org/10.1038/nbt.3942
1086 44 Urban, B. C. *et al.* Fatal Plasmodium falciparum malaria causes specific patterns of
1087 splenic architectural disorganization. *Infect Immun* **73**, 1986–1994 (2005).
1088 https://doi.org/10.1128/IAI.73.4.1986-1994.2005
1089 45 Ssewanyana, I. *et al.* Avidity of anti-malarial antibodies inversely related to transmission
1090 intensity at three sites in Uganda. *Malar J* **16**, 67 (2017). https://doi.org/10.1186/s12936-
1091 017-1721-3
1092 46 Kennedy, D. E. *et al.* Novel specialized cell state and spatial compartments within the
1093 germinal center. *Nat Immunol* **21**, 660–670 (2020). https://doi.org/10.1038/s41590-020-
1094 0660-2
1095 47 Suan, D. *et al.* CCR6 Defines Memory B Cell Precursors in Mouse and Human Germinal
1096 Centers, Revealing Light-Zone Location and Predominant Low Antigen Affinity. *Immunity*
1097 **47**, 1142–1153 e1144 (2017). https://doi.org/10.1016/j.immuni.2017.11.022

48 Mathew, N. R. *et al.* Single-cell BCR and transcriptome analysis after influenza infection reveals spatiotemporal dynamics of antigen-specific B cells. *Cell Rep* **35**, 109286 (2021). https://doi.org/10.1016/j.celrep.2021.109286
49 Tellier, J. *et al.* Unraveling the diversity and functions of tissue-resident plasma cells. *Nat Immunol* **25**, 330–342 (2024). https://doi.org/10.1038/s41590-023-01712-w
50 Pracht, K. *et al.* A new staining protocol for detection of murine antibody-secreting plasma cell subsets by flow cytometry. *Eur J Immunol* **47**, 1389–1392 (2017). https://doi.org/10.1002/eji.201747019
51 Pack, A. D. *et al.* Hemozoin-mediated inflammasome activation limits long-lived anti-malarial immunity. *Cell Rep* **36**, 109586 (2021). https://doi.org/10.1016/j.celrep.2021.109586
52 Lee, R. D. *et al.* Single-cell analysis identifies dynamic gene expression networks that govern B cell development and transformation. *Nat Commun* **12**, 6843 (2021). https://doi.org/10.1038/s41467-021-27232-5
53 Alexandre, Y. O. *et al.* A diverse fibroblastic stromal cell landscape in the spleen directs tissue homeostasis and immunity. *Sci Immunol* **7**, eabj0641 (2022). https://doi.org/10.1126/sciimmunol.abj0641
54 Grabstein, K. H. *et al.* Inhibition of murine B and T lymphopoiesis in vivo by an anti-interleukin 7 monoclonal antibody. *J Exp Med* **178**, 257–264 (1993). https://doi.org/10.1084/jem.178.1.257
55 von Freeden-Jeffry, U. *et al.* Lymphopenia in interleukin (IL)-7 gene-deleted mice identifies IL-7 as a nonredundant cytokine. *J Exp Med* **181**, 1519–1526 (1995). https://doi.org/10.1084/jem.181.4.1519
56 Kaiser, F. M. P. *et al.* IL-7 receptor signaling drives human B-cell progenitor differentiation and expansion. *Blood* **142**, 1113–1130 (2023). https://doi.org/10.1182/blood.2023019721
57 Kayentao, K. *et al.* Safety and Efficacy of a Monoclonal Antibody against Malaria in Mali. *N Engl J Med* **387**, 1833–1842 (2022). https://doi.org/10.1056/NEJMoa2206966
58 Skinner, J. *et al.* Anti-sporozoite monoclonal antibody for malaria prevention: secondary efficacy outcome of a phase 2 randomized trial. *Nat Med* **31**, 2682–2690 (2025). https://doi.org/10.1038/s41591-025-03739-y
59 Wu, R. L. *et al.* Low-Dose Subcutaneous or Intravenous Monoclonal Antibody to Prevent Malaria. *N Engl J Med* **387**, 397–407 (2022). https://doi.org/10.1056/NEJMoa2203067
60 Kayentao, K. *et al.* Subcutaneous Administration of a Monoclonal Antibody to Prevent Malaria. *N Engl J Med* **390**, 1549–1559 (2024). https://doi.org/10.1056/NEJMoa2312775
61 Kranich, J. *et al.* Follicular dendritic cells control engulfment of apoptotic bodies by secreting Mfge8. *J Exp Med* **205**, 1293–1302 (2008). https://doi.org/10.1084/jem.20071019
62 Krautler, N. J. *et al.* Follicular dendritic cells emerge from ubiquitous perivascular precursors. *Cell* **150**, 194–206 (2012). https://doi.org/10.1016/j.cell.2012.05.032
63 Pikor, N. B. *et al.* Remodeling of light and dark zone follicular dendritic cells governs germinal center responses. *Nat Immunol* **21**, 649–659 (2020). https://doi.org/10.1038/s41590-020-0672-y
64 Jondle, C. N. *et al.* B Cell-Intrinsic Expression of Interferon Regulatory Factor 1 Supports Chronic Murine Gammaherpesvirus 68 Infection. *J Virol* **94** (2020). https://doi.org/10.1128/JVI.00399-20

65 Calderon, L. *et al.* In vivo CRISPR/Cas9 screens identify new regulators of B cell activation and plasma cell differentiation. *J Exp Med* **223** (2026). https://doi.org/10.1084/jem.20250594

66 Hodgkin, P. D., Lee, J. H. & Lyons, A. B. B cell differentiation and isotype switching is related to division cycle number. *J Exp Med* **184**, 277–281 (1996). https://doi.org/10.1084/jem.184.1.277

67 Hasbold, J., Lyons, A. B., Kehry, M. R. & Hodgkin, P. D. Cell division number regulates IgG1 and IgE switching of B cells following stimulation by CD40 ligand and IL-4. *Eur J Immunol* **28**, 1040–1051 (1998). https://doi.org/10.1002/(SICI)1521-4141(199803)28:03<1040::AID-IMMU1040>3.0.CO;2-9

68 Rush, J. S., Liu, M., Odegard, V. H., Unniraman, S. & Schatz, D. G. Expression of activation-induced cytidine deaminase is regulated by cell division, providing a mechanistic basis for division-linked class switch recombination. *Proc Natl Acad Sci U S A* **102**, 13242–13247 (2005). https://doi.org/10.1073/pnas.0502779102

69 Le Bon, A. *et al.* Type i interferons potently enhance humoral immunity and can promote isotype switching by stimulating dendritic cells in vivo. *Immunity* **14**, 461–470 (2001). https://doi.org/10.1016/s1074-7613(01)00126-1

70 Tangye, S. G., Ferguson, A., Avery, D. T., Ma, C. S. & Hodgkin, P. D. Isotype switching by human B cells is division-associated and regulated by cytokines. *J Immunol* **169**, 4298–4306 (2002). https://doi.org/10.4049/jimmunol.169.8.4298

71 Deenick, E. K., Hasbold, J. & Hodgkin, P. D. Decision criteria for resolving isotype switching conflicts by B cells. *Eur J Immunol* **35**, 2949–2955 (2005). https://doi.org/10.1002/eji.200425719

72 Muramatsu, M. *et al.* Specific expression of activation-induced cytidine deaminase (AID), a novel member of the RNA-editing deaminase family in germinal center B cells. *J Biol Chem* **274**, 18470–18476 (1999). https://doi.org/10.1074/jbc.274.26.18470

73 Muramatsu, M. *et al.* Class switch recombination and hypermutation require activation-induced cytidine deaminase (AID), a potential RNA editing enzyme. *Cell* **102**, 553–563 (2000). https://doi.org/10.1016/s0092-8674(00)00078-7

74 Sundling, C. *et al.* Positive selection of IgG(+) over IgM(+) B cells in the germinal center reaction. *Immunity* **54**, 988–1001 e1005 (2021). https://doi.org/10.1016/j.immuni.2021.03.013

75 Jacob, J., Przylepa, J., Miller, C. & Kelsoe, G. In situ studies of the primary immune response to (4-hydroxy-3-nitrophenyl)acetyl. III. The kinetics of V region mutation and selection in germinal center B cells. *J Exp Med* **178**, 1293–1307 (1993). https://doi.org/10.1084/jem.178.4.1293

76 McKean, D. *et al.* Generation of antibody diversity in the immune response of BALB/c mice to influenza virus hemagglutinin. *Proc Natl Acad Sci U S A* **81**, 3180–3184 (1984). https://doi.org/10.1073/pnas.81.10.3180

77 Kleinstein, S. H., Louzoun, Y. & Shlomchik, M. J. Estimating hypermutation rates from clonal tree data. *J Immunol* **171**, 4639–4649 (2003). https://doi.org/10.4049/jimmunol.171.9.4639

78 Merkenschlager, J. *et al.* Regulated somatic hypermutation enhances antibody affinity maturation. *Nature* **641**, 495–502 (2025). https://doi.org/10.1038/s41586-025-08728-2

79 Pae, J. *et al.* Transient silencing of hypermutation preserves B cell affinity during clonal bursting. *Nature* **641**, 486–494 (2025). https://doi.org/10.1038/s41586-025-08687-8

1190 80 Dicko, A. *et al.* Seasonal vaccination with RTS,S/AS01(E) vaccine with or without
1191 seasonal malaria chemoprevention in children up to the age of 5 years in Burkina Faso
1192 and Mali: a double-blind, randomised, controlled, phase 3 trial. *Lancet Infect Dis* **24**,
1193 75–86 (2024). https://doi.org/10.1016/S1473-3099(23)00368-7
1194 81 Haque, A. *et al.* Type I interferons suppress CD4(+) T-cell-dependent parasite control
1195 during blood-stage Plasmodium infection. *Eur J Immunol* **41**, 2688–2698 (2011).
1196 https://doi.org/10.1002/eji.201141539
1197 82 Haque, A. *et al.* Type I IFN signaling in CD8- DCs impairs Th1-dependent malaria
1198 immunity. *J Clin Invest* **124**, 2483–2496 (2014). https://doi.org/10.1172/JCI70698
1199 83 Montes de Oca, M. *et al.* Type I Interferons Regulate Immune Responses in Humans
1200 with Blood-Stage Plasmodium falciparum Infection. *Cell Rep* **17**, 399–412 (2016).
1201 https://doi.org/10.1016/j.celrep.2016.09.015
1202 84 Webster, R. *et al.* Adjunctive ruxolitinib attenuates inflammation and enhances
1203 immunity in volunteers experimentally infected with Plasmodium falciparum. *Sci Transl*
1204 *Med* **17**, eaea2531 (2025). https://doi.org/10.1126/scitranslmed.aea2531
1205 85 Cooper, L. *et al.* Type I interferons induce an epigenetically distinct memory B cell
1206 subset in chronic viral infection. *Immunity* (2024).
1207 https://doi.org/10.1016/j.immuni.2024.03.016
1208 86 Belyaev, N. N. *et al.* Induction of an IL7-R(+)c-Kit(hi) myelolymphoid progenitor critically
1209 dependent on IFN-gamma signaling during acute malaria. *Nat Immunol* **11**, 477–485
1210 (2010). https://doi.org/10.1038/ni.1869
1211 87 Haltalli, M. L. R. *et al.* Manipulating niche composition limits damage to haematopoietic
1212 stem cells during Plasmodium infection. *Nat Cell Biol* **22**, 1399–1410 (2020).
1213 https://doi.org/10.1038/s41556-020-00601-w
1214 88 Ghosn, E. E., Sadate-Ngatchou, P., Yang, Y., Herzenberg, L. A. & Herzenberg, L. A.
1215 Distinct progenitors for B-1 and B-2 cells are present in adult mouse spleen. *Proc Natl*
1216 *Acad Sci U S A* **108**, 2879–2884 (2011). https://doi.org/10.1073/pnas.1019764108
1217 89 Ghosh, D. *et al.* An Atypical Splenic B Cell Progenitor Population Supports Antibody
1218 Production during Plasmodium Infection in Mice. *J Immunol* **197**, 1788–1800 (2016).
1219 https://doi.org/10.4049/jimmunol.1502199
1220 90 Lee, M. S. J. *et al.* Acute malaria suppresses the B lymphocytic niche in the bone
1221 marrow through the alteration of CXCL12-abundant reticular cells. *Int Immunol* **36**, 339–
1222 352 (2024). https://doi.org/10.1093/intimm/dxae012
1223 91 Kallies, A. *et al.* Plasma cell ontogeny defined by quantitative changes in blimp-1
1224 expression. *J Exp Med* **200**, 967–977 (2004). https://doi.org/10.1084/jem.20040973
1225 92 Dougan, S. K. *et al.* IgG1+ ovalbumin-specific B-cell transnuclear mice show class
1226 switch recombination in rare allelically included B cells. *Proc Natl Acad Sci U S A* **109**,
1227 13739–13744 (2012). https://doi.org/10.1073/pnas.1210273109
1228 93 Rigau, M. *et al.* Butyrophilin 2A1 is essential for phosphoantigen reactivity by
1229 gammadelta T cells. *Science* **367** (2020). https://doi.org/10.1126/science.aay5516
1230 94 Compte, E., Pontarotti, P., Collette, Y., Lopez, M. & Olive, D. Frontline: Characterization
1231 of BT3 molecules belonging to the B7 family expressed on immune cells. *Eur J Immunol*
1232 **34**, 2089–2099 (2004). https://doi.org/10.1002/eji.200425227
1233 95 Amante, F. H. & Good, M. F. Prolonged Th1-like response generated by a Plasmodium
1234 yoelii-specific T cell clone allows complete clearance of infection in reconstituted mice.
1235 *Parasite Immunol* **19**, 111–126 (1997). https://doi.org/10.1046/j.1365-3024.1997.d01-
1236 187.x

96 Akter, J. *et al.* Plasmodium-specific antibodies block in vivo parasite growth without clearing infected red blood cells. *PLoS Pathog* **15**, e1007599 (2019). https://doi.org/10.1371/journal.ppat.1007599

97 Hao, Y. *et al.* Integrated analysis of multimodal single-cell data. *Cell* **184**, 3573–3587 e3529 (2021). https://doi.org/10.1016/j.cell.2021.04.048

98 Sundell, T. *et al.* Single-cell RNA sequencing analyses: interference by the genes that encode the B-cell and T-cell receptors. *Brief Funct Genomics* **22**, 263–273 (2022). https://doi.org/10.1093/bfgp/elac044

99 Chen, J., Bardes, E. E., Aronow, B. J. & Jegga, A. G. ToppGene Suite for gene list enrichment analysis and candidate gene prioritization. *Nucleic Acids Res* **37**, W305–311 (2009). https://doi.org/10.1093/nar/gkp427

100 Liao, Y., Wang, J., Jaehnig, E. J., Shi, Z. & Zhang, B. WebGestalt 2019: gene set analysis toolkit with revamped UIs and APIs. *Nucleic Acids Res* **47**, W199–W205 (2019). https://doi.org/10.1093/nar/gkz401

101 Santos, A., Wernersson, R. & Jensen, L. J. Cyclebase 3.0: a multi-organism database on cell-cycle regulation and phenotypes. *Nucleic Acids Res* **43**, D1140–1144 (2015). https://doi.org/10.1093/nar/gku1092

102 Mabbott, N. A. & Gray, D. Identification of co-expressed gene signatures in mouse B1, marginal zone and B2 B-cell populations. *Immunology* **141**, 79–95 (2014). https://doi.org/10.1111/imm.12171

103 Lopez, R., Regier, J., Cole, M. B., Jordan, M. I. & Yosef, N. Deep generative modeling for single-cell transcriptomics. *Nat Methods* **15**, 1053–1058 (2018). https://doi.org/10.1038/s41592-018-0229-2

104 Wolf, F. A., Angerer, P. & Theis, F. J. SCANPY: large-scale single-cell gene expression data analysis. *Genome Biol* **19**, 15 (2018). https://doi.org/10.1186/s13059-017-1382-0

105 Stickels, R. R. *et al.* Highly sensitive spatial transcriptomics at near-cellular resolution with Slide-seqV2. *Nat Biotechnol* **39**, 313–319 (2021). https://doi.org/10.1038/s41587-020-0739-1

106 Williams, C. G. *et al.* Plasmodium infection induces phenotypic, clonal, and spatial diversity among differentiating CD4(+) T cells. *Cell Rep* **43**, 114317 (2024). https://doi.org/10.1016/j.celrep.2024.114317

107 Cable, D. M. *et al.* Robust decomposition of cell type mixtures in spatial transcriptomics. *Nat Biotechnol* **40**, 517–526 (2022). https://doi.org/10.1038/s41587-021-00830-w